INTERFACIAL EFFECTS IN FECOB BASED MAGNETIC TUNNEL JUNCTIONS AND SPIN HALL EFFECT BI-LAYER STRUCTURES

A Dissertation

Presented to the Faculty of the Graduate School

of Cornell University

In Partial Fulfillment of the Requirements for the Degree of

Doctor of Philosophy

by

Yun Li

January 2014

INTERFACIAL EFFECTS IN FECOB BASED MAGNETIC TUNNEL JUNCTIONS AND SPIN HALL EFFECT BI-LAYER STRUCTURES

Yun Li, Ph. D.

Cornell University 2014

The transfer of spin angular momentum from a spin-polarized current to a ferromagnet can generate sufficient torque to reorient the magnet's moment, thus this effect has prospective applications in spintronics. In this dissertation, the main theme of my work has been the study of spin-transfer-driven ferromagnetic resonance (ST-FMR) signals to understand what is the interfacial effects on the spin transfer torque (STT) in magnetic tunnel junction (MTJ) devices with a nanopillar geometry and bi-layer spin Hall effect structures.

In the first part of my work, I have studied the bias dependence of the spin transfer torques in the as-grown and annealed FeCoB/MgO/FeCoB MTJs by ST-FMR measurement. The motivation of this work was to understand the important mechanisms contributing to the in-plane torque with a view to optimizing the switching current of devices. I have found the annealing reduces the inelastic tunneling component of the junction conductance, and creates or enhances a peak at about 0.15V above the Fermi level in the density of states of the minority band of the electrodes, which may be the reason for the asymmetry of the bias dependence of the in-plane torque. This peak location is essentially the same as the peak of the minority

band states that has previously observed on the surface of bcc (100) Fe. The existence of these interfacial states can also explain the asymmetry of the TMR, and the bias dependence of both G_{AP} and G_P.

As a function of temperature, my experimental STTs can be explained by magnon contributions. My results show that with a relative increase of 50% in tunneling MR, however, both in-plane torque and perpendicular torque have been depressed at low temperature, indicating that magnon assisted tunneling, which results in a spin-flip process for the tunneling electron, has a negative contribution to the spin polarization, but plays a positive role in STT, with the latter consistent with recent theoretical predictions.

In the second part of my work, I have studied the spin-torque effects on the FeCoB/W bi-layer structures with different W phases. The motivation of this work was to investigate the spin Hall and spin pumping effects in this system. I have observed a greatly enhanced magnetic damping coefficient for the $Fe_{40}Co_{40}B_{20}$ layer with α-W, and I tentatively attribute these results to a significantly enhanced spin pumping effect in α-W, relative to that in β-W. Magnetization measurements indicate that the two different types of $Fe_{40}Co_{40}B_{20}$/W bilayers also have substantially different interfacial magnetic anisotropy coefficients.

BIOGRAPHICAL SKETCH

Yun Li was born in Hangzhou, China, is the only daughter of Zhongyue Li and Xiujuan Qian. Yun had a joyful childhood in her hometown, which has been one of the most renowned and prosperous cities of China for much of the last 1,000 years. Her most vivid childhood memories are sitting on the back-chair of her farther's bike and seeking for the beautiful natural sceneries surround the West Lake. Yun attended Hangzhou No. 2 middle school, where she found that the beauty of harmony is not only in the nature but also in science and mathematics. Encouraged by lovely teachers in the high school, she pursued her higher education in Physics.

In 2002, Yun was accepted into the undergraduate Physics program at the Peking University, Beijing. Thanks to Chun-Tseng Scholar Funding, which was supported by Tsung-Dao Lee, she had an opportunity to start her research in the low dimensional structure materials and physics lab, exploring the mysterious nano-size world. With the support from her family, she applied for the Ph. D programs in Physics in the USA. In 2007, she moved to the Ithaca, NY and was lucky enough to start his Ph.D. degree with Prof. Robert A. Burhman at the School of Applied and Engineering Physics, Cornell University since that summer, and really excited about spin-transfer torque physics. She obtained an M.S. in Applied Physics from Cornell in 2011 and will receive her Ph.D. in Physics in January 2014.

To my family

ACKNOWLEDGMENTS

During my Ph D. journey, I have met and worked with a lot of amazing people and have drawn strength from those friends. I would never have become what I am today their invaluable help and guidance.

First and foremost, I would like to express my gratitude to my advisor, Prof. Robert Buhrman. He is a brilliant scientist, a progressive thinker, and a patient advisor. I have learnt a lot while trying to make devices, collecting data and thinking about my scientific arguments to meet the high stands that he set. I am truly grateful for the time and effort that Bob has spent in guiding my career as well as my personal life. I would like to thank my special committee members Prof. Daniel C. Ralph and Prof. Bruce van Dover to provide my knowledge and guidance during my whole Ph. D. And I also appreciate Prof. David Muller and his students, Pinshane Huang and Paul Cueva, for providing me beautiful STEM pictures to help me understand many details of the chemical structure of my devices.

All the members of the Buhrman's group have been especially helpful, in particular the D7 team, John Read and Hsin-wei Tseng. John was my tutor or big brother in the lab when I joined the group. He told me how to grow the films, operate the STM system, maintain the ultra-low vacuum system, as well as how to come over the cultural shock and enjoy the life in the USA. Hsin-wei and I were working on the similar projects for more than 5 years. We shared the joy of the moment when we made the first MTJ device, obtained the first current switching data or finally made the

agreement on the explanation for the result after a long argument. He also helped me to get the driver license and provides me a number of financial advices.

Other members of the group I would like to thank include Patrick Braganca, Vlad Pribiag, Eric Ryan, Praveen Gowtham, Oukjae Lee and Takahiro Moriyama, Liuqiao Liu, Junbo Park for their assistance and persistence on maintaining all the lab equipments, sharing the experiences on device fabrication and the measurement setup, inspiring discussions on the spin transfer torques, without which much of my research would not be possible. I thank Luis Leao and Chi-Feng Pai for their assistance in the spin Hall effect experiment. Finally, for the younger students, Minghai and Yongxi, I thank them for continuing the research resource that myself and the other students contributed to, and I wish them the best of luck in their future endeavors. From the Ralph group, I would like to thank Yongtao Cui, Chen Wang, Lin Xue and Alex Mellnik for useful conversations on ST-FMR measurement, from which I were able to build a picture of the phenomena discussed in Chapter 4 and Chapter 5. I also deeply appreciate the encouragement of Wan Li when my life is up and down.

The devices discussed in Chapter 4 for the temperature dependence measurement were provided by Jordan Katine at HGST. I thank him for his contributions to that project.

I also like to thank for the great help from Jonathan Shu and Steve Kriske from The Cornell Center for Materials Research (CCNR) and all the staffs in the Cornell Nano Scale Science & Technology Facility (CNF)**.** Through the years, I have been

using CNF tools to do the fabrication and CNS equipments to perform my measurement. Without their assistance, no works can be done.

Finally, I want to acknowledge my family, who give me the freedom to pursue my career overseas but are always there whenever I need a support.

TABLE OF CONTENTS

LIST OF FIGURES

LIST OF TABLES

CHAPTER 1

INTRODUCTION

Spintronics is an emerging area of nanoscale electronics involving the spin injection, transport, modulation and detection, etc. [1-3]. It aims at developing devices based on control of the electron spin, with the potential advantages of nonvolatility, increased data processing speed, decreased electric power consumption, and increased integration densities compared with conventional semiconductor devices. In the past a few years, spintronics based on spin-transfer torque switching is considered as a major candidate since it allows the magnetization in magnetic devices to be manipulated efficiently using the interaction of spin-polarized currents with ferromagnets. In this dissertation, I use ST-FMR technique to measure the spin transfer torques in MgO-based magnetic tunnel junctions and bi-layer spin Hall effect structures. My research aims to unravel the fundamental physics of the spin transfer torques, especially the effects from the interfaces.

First of all, in chapter 2, I give a brief discussion of the development of spintronics mainly based on the MgO-based MTJs. I first introduce the historical development of the MR effect accompanied by a simple theoretical explanation for the essential physics. Then I discuss the issue of coherent and incoherent tunneling in amorphous (AlO_x) and crystalline (MgO) barrier materials. Here there is a discussion of interlayer structures in the MTJs which act as the additional scattering layer or can modify the interface resonance states. After that I track the development of magnetic

random access memory by spin transfer torque switching. And finally, I introduce some other spin effects, such as the spin Hall effect and the spin Seebeck effect.

In chapter 3, I present growth procedures that I developed for making MgO-MTJs and two layer structures for the spin Hall effect measurement, with a focus placed on the interplay of materials and device performance. Then I describe the lift-off process for fabrication of both micron-pillars and nanopillars, and the related major issues or problems are considered. Finally, I introduce the background of the measurement methods, including switching phase diagram and ST-FMR measurement that I used in my investigations.

In chapter 4, I present electronic transport studies, spin-torque studies and the chemical analysis on FeCoB/MgO/FeCoB MTJs in both the as-grown and annealed (350 ℃) cases. The ST-FMR measurement indicates that the asymmetry of the bias dependence of the in-plane torque is due to changes of the MTJs that occur in the annealing process. Analysis of the adjusted torkance suggests that the annealing reduces the inelastic tunneling component of the junction conductance, and creates or enhances a peak at about 0.15V above the Fermi level in the density of states of the minority band of one or both of the electrodes, which is essentially the same as the peak of the minority band states that has previously observed on the surface of bcc (100) Fe. This model can also explain the features in the bias dependent conductance and TMR. At the end of this chapter I describe studies of the temperature dependence of STT, which reveals the magnon contribution on the STT experimentally.

Finally, I discuss my ST-FMR study of the spin Hall effect in chapter 5 which shows that both the spin Hall effect and the spin pumping effect can exist in the FeCoB/W bilayers, with the latter effect greatly dependent on the thickness of the W, correlated with the phase change of the W-thin film. This result can be explained by our modified spin Hall effect and spin pumping effect model. Magnetization measurements also indicate that the two different types of FeCoB/W bilayers have substantially different interfacial magnetic anisotropy coefficients. In the last section of chapter 5 I report on preliminary work that I have done on the possible spin Hall effect in WSi_x and discuss possible experiments where the spin Hall effect could be used to provide spin injection into a Si substrate.

BIBLIOGRAPHY

1. Wolf S. A., Awschalom D. D., Buhrman R. A., et al. Spintronics: A spin-based electronics vision for the future. *Science*, 294, 1488 (2001).

2. Žutić I., Fabian J., Das Sarma S. Spintronics: Fundamentals and applications. *Rev. Mod. Phys.*, 76, 323 (2004).

3. Ohno H. A window on the future of spintronics. *Nat. Mater.*, 9, 952 (2010).

CHAPTER 2

BACKGROUND

Spintronics, exploiting both the spin of the electron and its associated magnetic moment, in addition to its fundamental electronic charge, has received great attention and significant interest within the past decades, and has provided considerable and remarkable applications in industry and electronic information. In spintronics, the MgO based MTJ is an important research advancement because of its high magnetoresistance (MR) and tunable resistance-area (RA) product. In this chapter, I mainly focus on the development of the Fe/MgO/Fe or FeCo/MgO/FeCo based MTJs, including: the historical development and basic physics of MTJs, MgO based MTJs with interlayer structures, interfacial perpendicular anisotropy and spin transfer torque (STT) effect. The final section outlines other spintronics devices based on the other mechanisms, such as the spin Hall effect and the Seebeck effect.

2.1 GMR and TMR

When a core structure consists of a thin layer sandwiched between two ferromagnetic (FM) metal layers (metal electrodes), and when that thin middle layer is an insulator and is used as a tunnel barrier, the structure is known as a magnetic tunnel junction (MTJ). Then the change in the electrical resistance of the tunnel junction as a function of whether the magnetic moments of the two ferromagnetic layers are parallel or anti-parallel is known as the tunneling magnetoresistance (TMR) effect. When the thin middle layer is non-magnetic metal, such as Cr, Cu, it is called spin-valve

structure, and then the magnetoresistance change that occurs when the two ferromagnetic electrodes go from being parallel to being anti-parallel is known as the giant magnetoresistance (GMR) effect.

The TMR effect was first observed in 1975 by Julliére [1], who observed a difference in the resistance of a Fe/Ge–O/Co MTJ as a function of the relative orientation of the ferromagnetic electrode magnetizations in an applied magnetic on the order of 14% at 4.2 K. Based on the ferromagnetic electrode (FM)/insulator (I)/ferromagnetic electrode (FM) model structure, TMR ratio is defined as: TMR = $(G_P-G_{AP})/G_{AP}$, where G_P and G_{AP} are conductance under parallel and anti-parallel states respectively, and P_i is the spin polarization of ferromagnetic electrode (i=1 or 2), which is defined as $P_i=(N_i\uparrow-N_i\downarrow)/(N_i\uparrow+N_i\downarrow)$, Here the $N_i\uparrow$ and $N_i\downarrow$ are density of states (DOS) at the Fermi level for the majority and the minority spins respectively. As shown in the Figure 2-1, the tunnel resistance of a MTJ depends on the relative orientation of magnetic moments in the two ferromagnetic layers. For the parallel alignment of the magnetizations, the tunneling resistance R of the junction is lower (Figure 2-1(a)), whereas it is higher for the opposite case when the magnetizations are anti-parallel (Figure 2-1(b)). Here the DOS for both majority and minority bands are described by a simplified free-electron model, however, *d* bands and/or the hybridization between *sp* and *d* electrons to the electrical transports are also critical for both ferromagnetism. This model also assumes that tunneling probabilities are equal for all the Bloch states in the electrodes. This assumption corresponds to a completely incoherent tunneling, in which none of the momentum and coherency of Bloch states

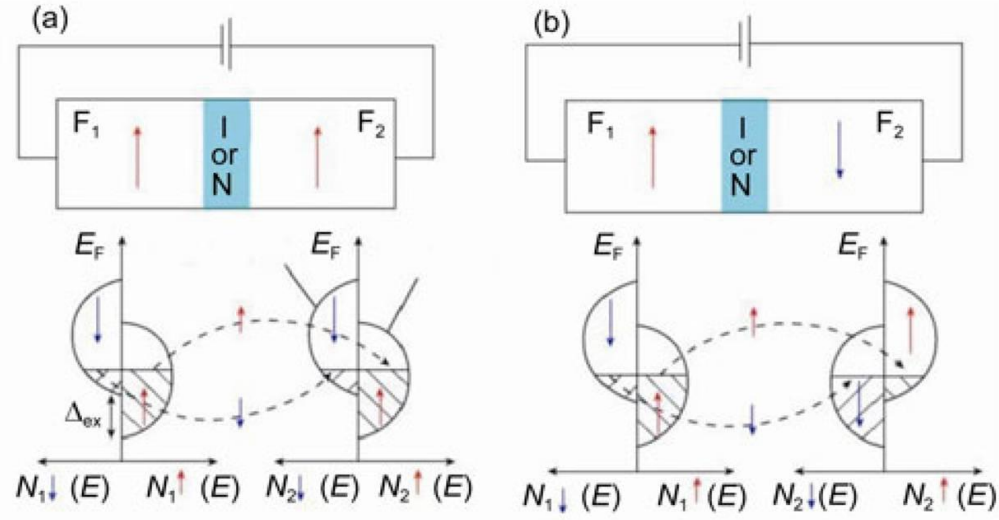

Figure 2-1. Schematic illustration of the MR effect, where I indicates insulator (in that case, TMR effect) and N indicates non-magnetic metal (GMR effect). A two-current model for (a) parallel and (b) anti-parallel alignment of the magnetizations, $N_i\uparrow$ and $N_i\downarrow$ (i=1,2) respectively denote the density of states at Fermi level for the majority-spin and minority-spin bands in electrode i. [From Ref. 79]

is conserved. It is not the case for most tunnel barriers. Therefore more detail band structures and tunneling coherency need to be considered in calculating the TMR behavior of a MTJ.

After that the original Julliere experiment, the TMR effect did not receive mcuh attention for almost a decade due to lack of the room temperature data. On the other hand, in the late 1980s the GMR effect was discovered and identified as a new spin-dependent phenomenon with very promising technical applications.

In 1986, Grünberg et al. [2] first reported the antiferromagnetic interlayer exchange coupling in the Fe/Cr/Fe trilayers, with an enhanced room temperature MR

up to 1.5%. Subsequently [3]. Baibich et al. [4] independently observed a large MR around 50% at low temperature in Fe/Cr magnetic superlattices, and attributed it to the spin-dependent transmission of the conduction electrons between the Fe layers through Cr layers. After that, the Co/Cu system received a lot of interest because it has good lattice matching between Co and Cu, resulting in low dislocation density at the interface and low extrinsic spin independent scattering processes. For example, at room temperature, GMR larger than 65% has been achieved in Co/Cu multilayers.[5]. As ther result commercial GMR sensors and read heads were introduced and produced in late 1990s [6]. Currently, GMR magnetic sensors have already found wide applications in different fields such as data storage, and as magnetic sensors used in engineering, biology ,and space science [7].

The demonstration of GMR revitalized experimental and theoretical studies devoted to increase the MR ratio at RT. TMR ratios on the order of 10% in MTJs with amorphous aluminum oxide (Al–O) tunnel barriers and 3d ferromagnetic electrodes were achieved by Miyazaki et al. [8] and Moodera et al. [9] in 1995, and attracted a great deal of attention. TMR had been increased by about 80% by optimizing the ferromagnetic electrode materials and the conditions for fabricating the Al–O barrier [10]. Meanwhile, the MgO based MTJs such as Fe(001)/MgO(001)/ Fe(001) based single crystalline MTJ was predicted theoretically indicating the possibility to obtain extremely high TMR ratios [11] because of the tunneling of coherent electrons. In 2004, 220% TMR ratios at RT was obtained by sputtering methods in Parkin's group [12] and 180% by using molecular beam epitaxy (MBE) by Yuasa et al. [13]. After

that, more researches directed to MgO based MTJs were reported. Until now, the highest achieved value of TMR is 604% at RT [14].

The reason of such a large TMR ratio can be explained by the coherent tunneling of electrons through the barrier [15-16]. The momentum of electron during the tunneling through an amorphous barrier does not remain conserved because of the nonsymmetrical barrier structure and scattering within the barrier. Bloch states with various symmetries can couple with evanescent states in Al–O and therefore have finite tunneling probabilities. This tunneling process can be regarded as an incoherent tunneling. However, in a crystallized MgO barrier, coherent tunneling transport occurs because of its electronic structure. In Fe(001)/MgO/ Fe MTJs, $\Delta 1$, $\Delta 2$, $\Delta 2'$ and $\Delta 5$ electric states can tunnel the MgO barrier by coherent tunneling (See Figure 2-2). First-principles based calculations show that Bloch states with different orbital symmetry couple into the MgO tunneling states with different efficiency. Only the majority channel has the slowly decaying $\Delta 1$ state. Therefore, as the MgO barrier gets thicker, the majority electrons that are most likely to tunnel to the counter electrode have s-like $\Delta 1$ symmetry. In the case of minority spin states, $\Delta 5$ Bloch states decay more slowly than $\Delta 2$ and $\Delta 2'$ Bloch states. So, the minority electrons with $\Delta 5$ symmetry are more likely to tunnel through a thick MgO barrier. Since $\Delta 1$ majority states decay far more slowly in MgO tunnel barrier than $\Delta 5$ minority states, its conductance is much higher than that of the minority channel. The large difference in

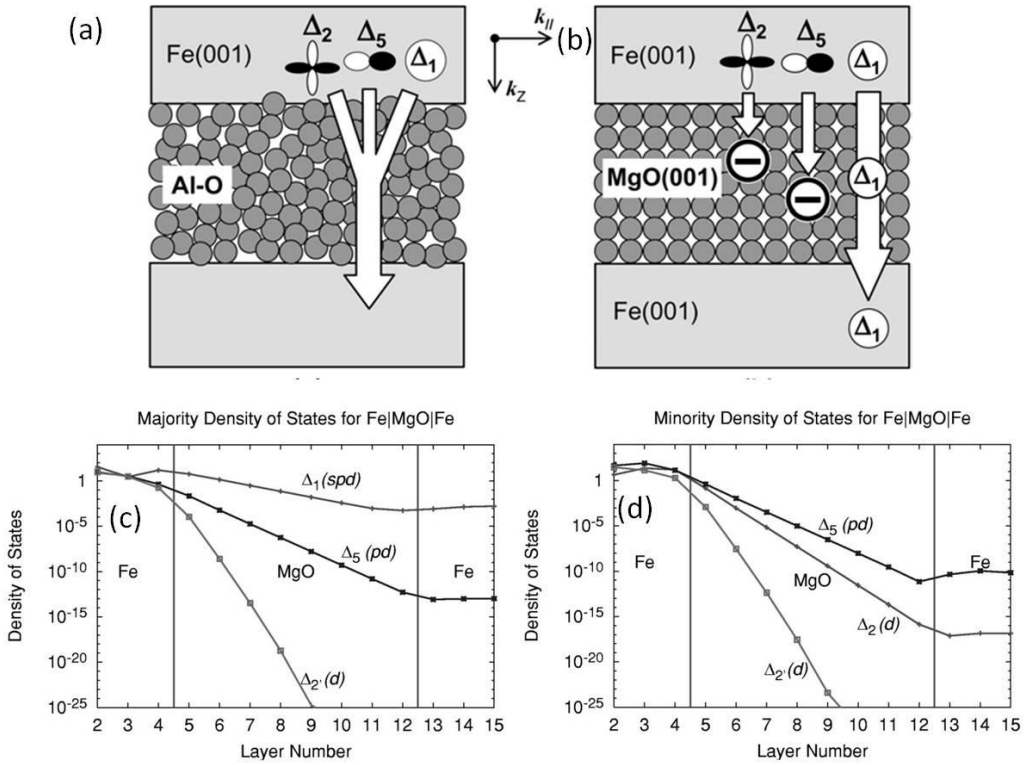

Figure 2-2. Schematic illustrations of electron tunneling through (a) an amorphous Al–O barrier and (b) a crystalline MgO (0 0 1) barrier [From Ref. 15]. (c-d) Tunneling DOS for $k_{//}$=0 for Fe(100)/8MgO/Fe(100). The two panels show the tunneling DOS for (c) majority and (d) minority [From Ref. 16].

these tunnel currents is the primary reason for the extraordinarily high TMR in Fe / MgO / Fe MTJs.

2.2 MgO based MTJs with interlayer structures

Interfacial engineering in single-crystal magnetic MTJs has been of extensive interest since it allows experimental and theoretical investigation and understanding of fundamental physics related to the spin-dependent tunneling. Interlayers in MTJs are layers with atomic thicknesses inserted between one of the magnetic electrodes and

the barrier. Such interlayers can have a significant effect on spin-dependent tunneling. In addition to the possibility that they can be used to further optimize the performance of the MTJs, the interlayer may act as the additional scattering layer or modified the interface resonance states (IRS). In this section I overview the studies on the adjustment of the tunneling efficiency or interfacial resonant states by inserting thin metal layers of various types between the electrode and the MgO layer.

2.2.1 Mg layer

To provide a crystalline seed layer for the tunnel barrier and to prevent the possible oxidation of the electrode at the junction interface, the use of a ultrathin Mg layer on top of the bottom ferromagnetic electrode layer prior to the deposition of MgO has been studied [17-18]. Miao et al. [17] reported that the spin symmetry of the bulk Fe Bloch states can be maintained well into an Mg interlayer as thick as 10 Å with artificial asymmetric barriers in CoFeB/ Mg/MgO/CoFeB MTJs. A slight increase in TMR has been observed with the first few angstroms Mg layer followed by a significant drop with further increase in the Mg layer (Figure 2-3(c)), with the maximum effect usually occurs at the nominal Mg thickness of 2–4 Å. The increase in RA value indicates that there exists some Mg converted into MgO, but only by a small amount because a fully oxidized 10 Å Mg would increase RA by more than three orders of magnitude. Their results also suggest that the spin coherence can remain even for a 10 Å Mg layer, indicating that the Bloch states have long diffusion length in Mg.

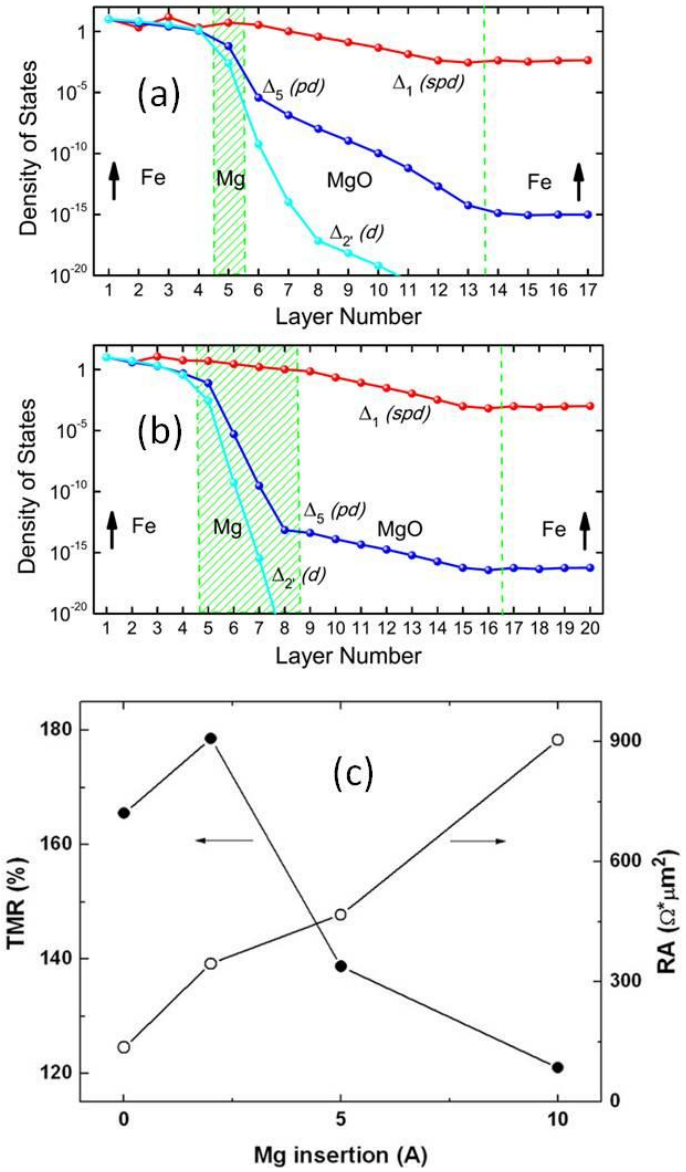

Figure 2-3. MTJs with Mg interlayer (a-b) DOS on each atomic layer of (a) Fe/Mg 1ML/MgO/Fe , (b) Fe/Mg 4ML/MgO/Fe for $k_{//}=0$ with parallel configuration. Each DOS curve is labeled by the symmetry of the incident Bloch state in the left Fe electrode at the Fermi energy. Shadow area and dashed line represent the Mg interlayer and the Fe/MgO interface, respectively. Arrows represent the relative magnetization in the Fe electrodes (From Ref. 19). (c) TMR and RA dependence on the Mg insertion layer thickness at room temperature.(From Ref. 17).

The effect of the Mg interlayer has been studied by first-principles calculations. Wang et al. [19] reported that that the Mg interlayer can preserve the preferential transmission of the majority-spin states with Δ1 symmetry, which dominates the spin dependent electron transport in MTJs with MgO barrier. It was also found that at a certain Mg thickness, resonant tunneling strongly influences the TMR in the minority-spin channel. Figure 2-3(a-b) show that the decay rate of the Δ1 state in Mg is much smaller than in the MgO barrier, but the DOS for other symmetry states decreases rapidly with a decay rate much larger than within the MgO barrier. Thus a thin Mg interlayer can also act as a spin symmetry filter and produce spin-dependent transport that preferentially filters for the majority-spin Δ1 states. This result can explain why TMR increases first with an ultra-thin Mg layer. However, at certain Mg thickness, a quantum well state lays exactly at the Fermi level and couple to a minority-spin *d*- IRS of adjacent Fe, corresponding to the large resonance peak in minority-spin conductance. Thus the TMR is strongly influenced by resonant tunneling, resulting in a significant drop.

2.2.2 FeO layer

For the junction with 1 ML FeO interface layer in Figure 2-4(a), the Δ1 state decays rapidly in the FeO layer compared to the Mg interlayer, consistent with their calculated large G_P difference between Fe/Mg/MgO/Fe and Fe/FeO/MgO/Fe. This result also explains why the formation of FeO on the interface greatly reduces the TMR [20-22]. Tiusan et al. [23] reported that the direct impact of the electronic

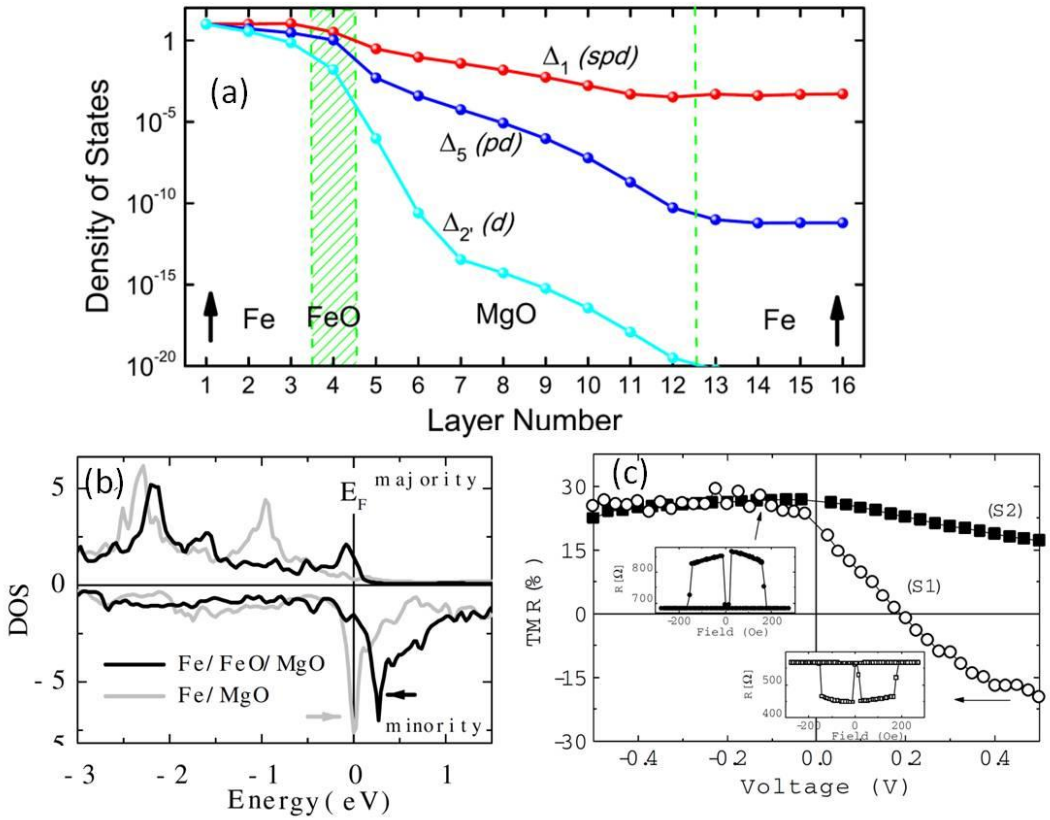

Figure 2-4. MTJs with FeO interlayer (a) DOS on each atomic layer of Fe/FeO/MgO/Fe for $k_{//}$=0 with parallel configuration [From Ref. 19]. (b) Calculated local spin-polarized DOS for the interfacial Fe in Fe/MgO/Fe and Fe/FeO/MgO/Fe stacks. The arrows indicate the IR in the minority DOS of Fe. (c)TMR versus the voltage *V* curves measured in two Fe/MgO/Fe samples with different growth conditions. Insets: Positive TMR versus magnetic field *H* curve measured at *V* =-0.1 V, negative *TMR(H)* curve measured at *V* =0.5 V (From Ref. 23).

structure on spin-polarized transport has been observed experimentally in the Fe/MgO/Fe epitaxial MTJs, with an extremely flat bottom Fe/MgO interface. Their result shows that there is an IRS located in the minority band of Fe(001), and it is sensitive to the quality of the interface. When coupled to a metallic bulk state, this

spin-polarized interfacial state enhances the band matching at the interface and therefore increases strongly the conductivity in the AP configuration. Consequently, the TMR is found to be positive below 0.2V and negative above (See Figure 2-4 (c) S1 case); On the other hand, when the interfacial state is either destroyed by roughness-related disorder or not coupled to the bulk, the magnetoresistance is almost independent on the bias voltage (the S2 case). The spin-polarized DOS in Fe/MgO/Fe and Fe/FeO/MgO/Fe stacks were calculated, and the results are shown in the Figure 2-4(b). They find an IR state located in the minority *d* orbital for both Fe(001)/MgO and Fe/Fe-O/MgO systems, and its location in energy shifts upwards when the complete O monolayer is introduced between the Fe and MgO..

2.2.3 Cr layer

Cr (001) presents some unique properties because of the absence of the $\Delta 1$ band at the Fermi Energy, while this fully spin-polarized band in Fe or FeCo is critical for high TMR in MgO based junctions as I discussed above. Furthermore, the Cr (001) on Fe (001) has the layer-antiferromagnetic ordering [24]. Scattering caused by such magnetic ordering near the interface may also have a profound impact on the TMR.

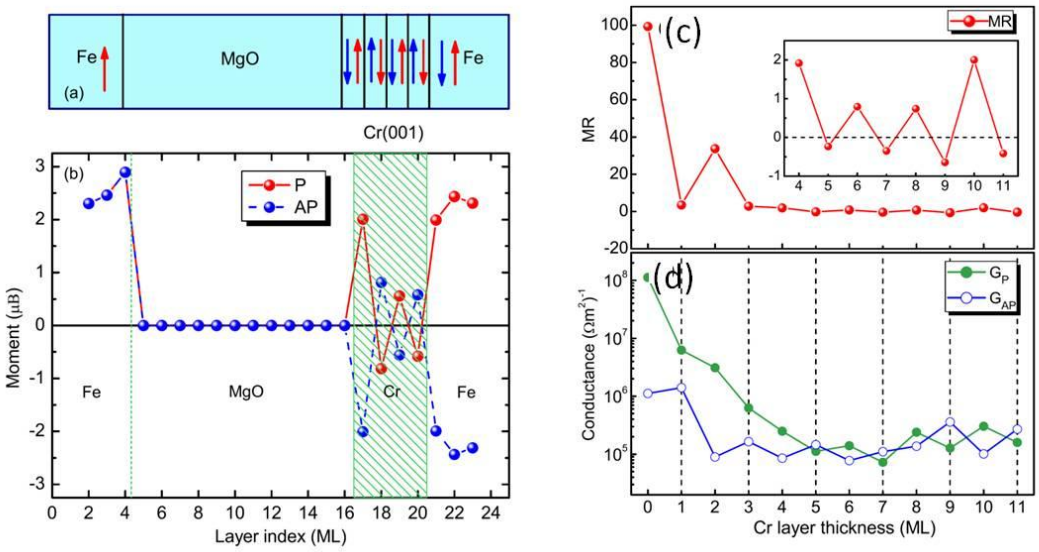

Figure 2-5. MTJs with Cr interlayer (a) Schematic sketch of the structure of a Fe/MgO/Cr/Fe tunneling junction. The arrows indicate the magnetic moment directions. (b) The layer-resolved magnetic moment for parallel alignment (red solid line) and antiparallel alignment (blue dashed line) of the Fe electrodes for a junction with 4 ML Cr (green shadow region) by first-principles calculation. (c) MR as a function of Cr layer thickness (the inset shows the details for the range of 4–11 ML). (d) Tunneling conductance in P (circle) and AP (open circle) configurations. [From Ref. 25]

Zhang et al. [25] used first-principles to calculate the electronic, magnetic, and tunneling properties of Fe/MgO/Cr/Fe MTJs. They show that the tunneling conductance is strongly dependent on thickness of the Cr, correlated with the Cr moment at the Cr-MgO interface. (See Figure 2-5). The calculated conductance as well as the MR ratio show two-monolayer oscillations as a function of Cr layer thickness, in agreement with experiments. Independent of the thickness of the Cr layer

0–11 ML, the Cr moment at the Fe-Cr interface is always antiferromagnetically coupled to the adjacent Fe electrode, and the moments of the rest of the Cr layers alternate in sign layer by layer. The oscillatory interfacial Cr moment at the Cr-MgO interface as a function of the Cr layer thickness, which arises from the layer-antiferromagnetic ordering of Cr, is the cause for the oscillations [25-26]

2.2.4 C layer

To study the interplay of the interlayer spin-orbit coupling (SOC) and minority IRSs on the magneto transport properties in single crystal Fe(001)/MgO/Fe MTJs, Lu et al. [27] used C as interlayer in the control sample Fe/C/MgO/Fe MTJs to affect the IRSs. They found a large difference of conductance between the two field directions for pure Fe MTJs (See Figure 2-6(a-b)). The in-plane conductance is higher than the out-of-plane one. However, in their C-doped sample the small difference in conductivity between the two directions indicated a weak SOC around the zero bias. Thus the different tunneling anisotropic magnetoresistive (TAMR) at zero bias indicates that the sample without C has stronger SOC at the interface than the sample with C. Meanwhile theoretical ab initio calculations predicted that the SOC scattering is enhanced between the majority $\Delta 1$ and minority $\Delta 5$ band near the Fermi level when presenting a $\Delta 5$ symmetry dominant IRS at the Fe/MgO interface, which are affected by inserting a C layer. Their results validate the interplay between SOC and IRSs, which gives a possible explanation for the tunneling anisotropic magnetoresistance and the large perpendicular magnetic anisotropy at the Fe/MgO interface.

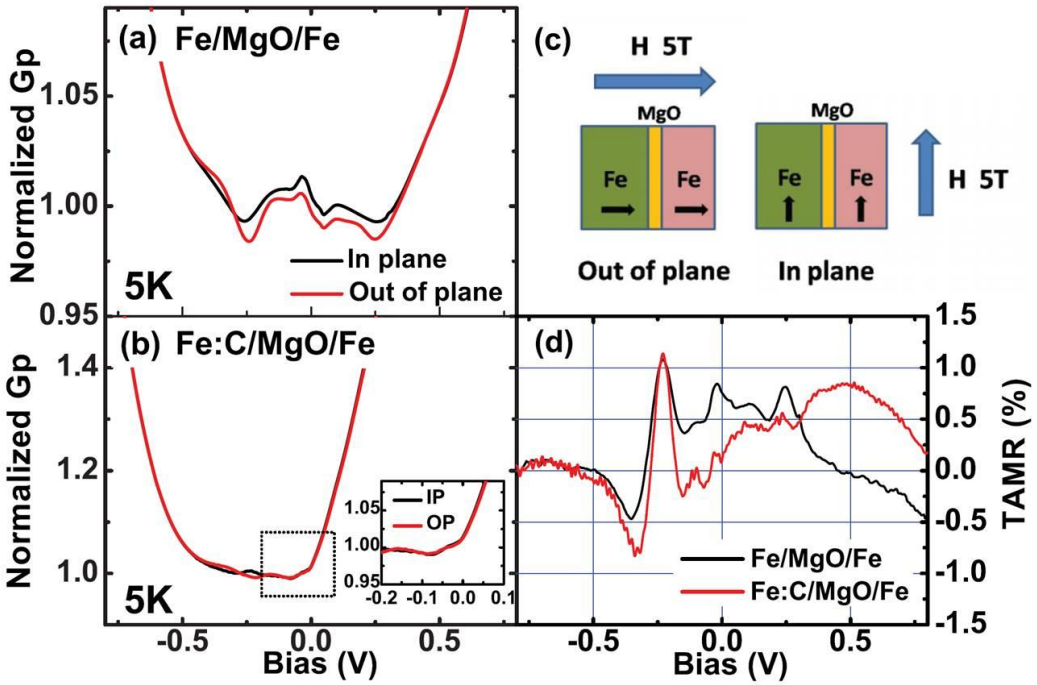

Figure 2-6. MTJs with C interlayer. (a-b) Bias dependence of normalized dynamic conductance in a perpendicular and in-plane field at 5 K for (a) a pure Fe/MgO/Fe MTJ and (b) a Fe/C/MgO/Fe MTJ. The inset shows the magnified zoom in the dashed square. (c) Schematic diagram of the tunneling anisotropic magnetoresistive (TAMR) measurement. (d) Bias dependence of TAMR for MTJs with and without C [From Ref. 27].

2.3 Magnetic anisotropy

Ferromagnetic materials have intrinsic easy and hard directions of the magnetization. This magnetic anisotropy is one of the most important properties of magnetic materials. Low dimensional magnetic systems, including surfaces, interfaces and thin-films, show different magnetic anisotropy.

2.3.1 Perpendicular MTJs

STT-MTJs with perpendicular magnetic anisotropy electrodes MTJ (p-MTJ) attracted much interest due to the potential to reduce the critical current density of the STT switching, while maintaining the thermal stability [28-30] without the shape limitation, since thermal stability of perpendicular magnetic anisotropy electrodes is controlled by material magnetic anisotropy instead of shape anisotropy.

The interfacial perpendicular anisotropy between oxide and ferromagnetic metal (Fe/MgO) has been predicted by first- principles calculation and attributed to hybridization of Fe 3d and O 2p orbital [31]. Earlier experimental studies indicated the presence of perpendicular anisotropy at the interface in Pt/Co/MOx (M = Al, Mg, Ta and Ru) trilayer structures [32-33]. In 2008, Ohmori et al. [34] measured p-MTJs with layer structure as GdFeCo(100) /Fe(3) /MgO(3) /Fe(3)/ TbFeCo(100 nm). They used extraordinary Hall effect measurement to clarify that the perpendicular magnetic components of 3 nm thick Fe buffer layers on the two ends of MgO tunneling barrier layer were increased by exchange coupling with GdFeCo alloy layers. TMR ratio of 64% was obtained in the multilayered p-MTJ element by current-in-plane tunneling. In the same year, Yoshikawa et al. [35] reported $L1_0$-FePt/MgO/Fe/$L1_0$-FePt p-MTJ films with the (001) texture and realized a large TMR ratio above 100% at RT. After this, studies on MgO based MTJs with CoFe/Pd multilayer electrodes or interlayer insertion, such as Fe and FeCo were reported [36]. In 2010, Ikeda et al. [37] used Ta/CoFeB/MgO/CoFeB/Ta structures to obtain a TMR ratio of over 120% at RT with p-

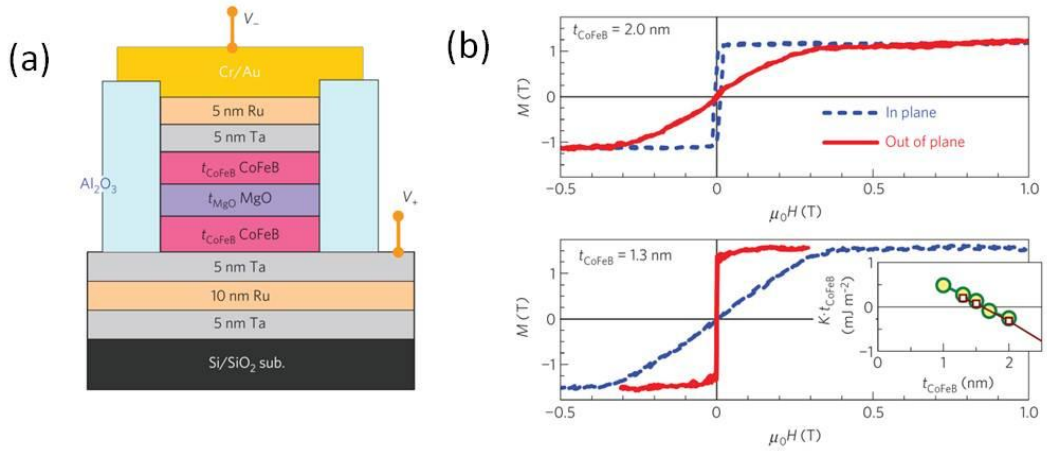

Figure 2-7. MTJs with perpendicular magnetic anisotropy. (a) Schematic of an MTJ device for TMR and current induced magnetic switching measurements. (b) In-plane and out-of-plane magnetization curves for CoFeB/MgO (up) t_{CoFeB} =2.0 nm. (bottom) t_{CoFeB}=1.3 nm. Inset: t_{CoFeB} dependence of the product of K and t_{CoFeB}, where the intercept to the vertical axis and the slope of the linear extrapolation of the data. Circles and squares are obtained from magnetization and FMR measurements, respectively. The data show that PMA is achieved when t_{CoFeB} is below 1.5nm. [Ref. 37]

MTJ properties by using interfacial perpendicular anisotropy between the ferromagnetic electrodes and the tunnel barrier of the MTJ by employing the material combination of CoFeB-MgO. As shown in the Figure 2-7, the anisotropy field, H_K increases as thickness reduces and changes its sign reflecting the change of magnetic-easy-axis direction around t_{CoFeB}=1.5 nm. Their results exploit interfacial perpendicular magnetic anisotropy that exists between CoFeB and MgO for fabricating high-performance MTJs and demonstrate that the present approach is capable of producing 40-nm-scale MTJs with sufficient E/k_BT, low critical switching current and high TMR ratio all at the same time with the potential applications in

future high-density memories and logic circuits, using current induced magnetic switching. Subsequently many other researchers focused on the interface induced perpendicular anisotropy in MgO based MTJs [38-39].

2.3.2 Voltage controlled PMA in MTJs

Both theoretical and experimental work have shown that magnetization and the magnetic anisotropy energy (MAE) in ferromagnetic layer can be modulated by electric method, which can crucially reduce the required magnetic field to switch the magnetization, developing the electric-field assisted magnetic recording technology.

Early work includes ferroelectric/ferromagnetic heterostructure, such as Fe/$BaTiO_3$ [40-41]. Duan et al. [41] found that at the Fe/$BaTiO_3$ interface, there exists strong atomic bonding between Fe and Ti atoms and this bonding induced obvious magnetic moment at Ti atom. Controlled by the electric field, the polarization in $BaTiO_3$ can influence the orbital magnetic moments and MAE of the Fe layers at the interface.

Niranjan et al. [42] further investigated the electric field effect on magnetization at the Fe/MgO(001) interface. The result from density-functional calculations shows the induced spin density and the magnetic moment of Fe atom at the Fe/MgO interface depend on the electric field in the MgO. They predicted an enhancement of the interface magneto-electric susceptibility by a factor of the dielectric constant of MgO over that of the free standing Fe (001) surface. They also predicted a significant effect of electric field on the interface magneto-crystalline

anisotropy because of the change in the relative occupancy of the 3*d*-orbitals of Fe atoms at the Fe/MgO interface, which may be interesting for technological applications such as electrically controlled magnetic data storage. Further studies show that a relatively small electric field (less than 100 mV/nm) can cause a large change (~40%) in the magnetic anisotropy of a bcc Fe(001)/ MgO(001) junction, which was also confirmed by simulations.

Wang et al. [43] reported electric-field-assisted reversible switching in CoFeB/MgO/CoFeB MTJs with interfacial perpendicular magnetic anisotropy (schematic drawing of the MTJ is shown in the Figure 2-8(c)). They demonstrated in CoFeB/MgO/CoFeB that the electric field, both the magnitude and its direction, has a direct effect on the perpendicular magnetic anisotropy (PMA) of the CoFeB layers, such that the magnetic configuration and tunneling magnetoresistance can be switched at much smaller current densities. Figure 2-8(d) shows the switching characteristics of the MTJ depend explicitly on the bias voltage V_{bias}, both the value as well as sign. Later on, Shiota et al. [44] showed that electric field pulses can be used to induce a coherent processional magnetization switching, and a bi-stable toggle switching using the coherent precession is realized.

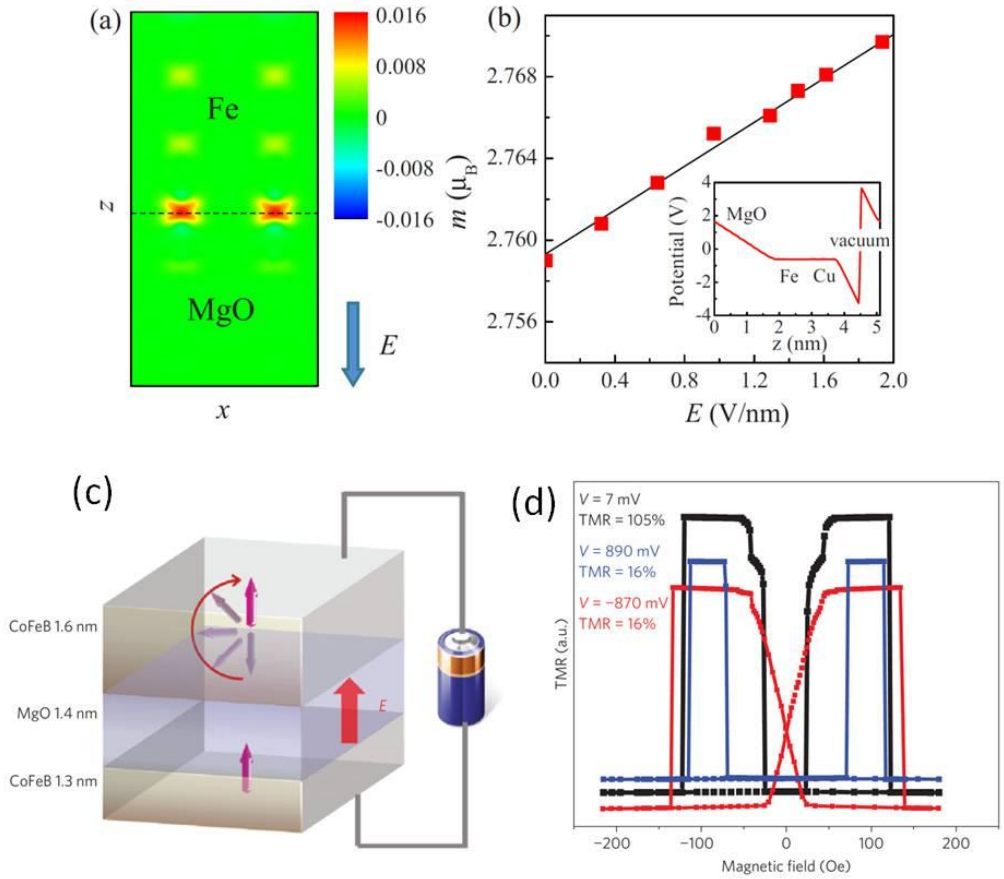

Figure 2-8. Voltage control magnetic anisotrophy. (a) Induced spin density $\Delta\sigma = \sigma(E) - \sigma(0)$, in units of $e/\text{Å}^3$, projected to the (010) plane around the Fe/MgO interface under the influence of electric field E=1.0 V/nm in MgO. The dashed line indicates the interfacial Fe monolayer at the Fe/MgO interface. (b) Magnetic moment of Fe at Fe/MgO interface as a function of the electric field in the MgO. The inset shows the calculated electrostatic potential across the supercell due to the applied electric field E=4 V/nm [From Ref. 42]. (c-d) Electric-field-assisted switching in a CoFeB/MgO/ CoFeB MTJ with interfacial perpendicular magnetic anisotropy. (c) Schematic drawing of a p-MTJ and the effect of electric field through a small voltage supplied by a battery. (d) TMR curves under different bias voltages [From Ref. 43]

2.4 Spin transfer torque effect

In STT switching, a spin polarized current is utilized to directly switch the magnetization of a nanomagnet. In this case, a spin-polarized electrical current can apply a large torque to a ferromagnet, which can switch the magnetization of free magnetic layer without applying external magnetic field [45-46]. It was theoretically predicted in 1996 by Slonczewski [47] and Berger [48] and first demonstrated in metallic spin valve thin films with critical switching current density (J_{c0})>10^7–10^8 A/cm^2 [49-51], but this number is too large for conventional magnetic random access memory (MRAM), where a magnetic field generated by pulse currents is used for the writing process. In order to realize a compact cell size (density >1 Tbits/in^2), high speed(<1ns) and low energy (writing current < 10^5-10^6 A/cm^2), the unit in MRAM must meet a set of performance requirements on switching current density, voltage, magnetoresistance ratio (MR), resistance-area product (RA), thermal stability factor, switching current distribution, read resistance distribution and reliability.

Later 2004, because of the important discovery of high TMR>100% CoFe based MgO MTJs at room temperature, which yields a very high output signal, several groups reported STT effect in MgO based MTJs [52-54]. In 2005, Diao et al. [55] reported spin transfer switching results for MgO based MTJs with ratio of up to 150% and low intrinsic switching current density of (2–3)×10^6 A/cm^2, a three times reduction in J_{c0} has been found in MgO barrier based MTJs as compared to that obtained on Al–O*x* MTJs, resulting from the enhancement of spin transfer efficiency caused by higher tunnel spin polarization. These low RA MgO-MTJs enable high-

density spin transfer switching MRAM with fast access time of few nanoseconds. (See Figure 2-9).

After that, more effects have been put in the development of MgO based MTJs. For example, STT switching was achieved in the p-MTJs with high thermal stability at dimension as low as 40nm diameter and a low switching current of 49 μA [37]. Electric-field-assisted reversible switching were reported with the switching current around 2 $x10^4$ A/cm^2, thanks to the greatly reduced energy barrier and the applied H_{bias} , which is much smaller than the normal STT switching current density at 10^6 A/cm^2 [43].

Since the behavior of spin torque provides a sensitive probe into the fundamental spin physics of hot electrons and is critical for applications, there are several efforts to understand the fundamental spin-torque effect in the MTJs experimentally and theoretically. The microwave emission is measured to estimate the in-plane and field-like torque by Deac et al. in the MgO-based MTJs [56], and Oh et al. examined the bias dependence of the field-like torque in asymmetric MTJs by fitting the switching phase diagram with the thermal activation model [57]. Currently, ST-FMR technique is applied to MgO-based MTJs to quantitatively measure the spin-torque vectors [58-59]. The details of ST-FMR technique will be discussed in the next chapter.

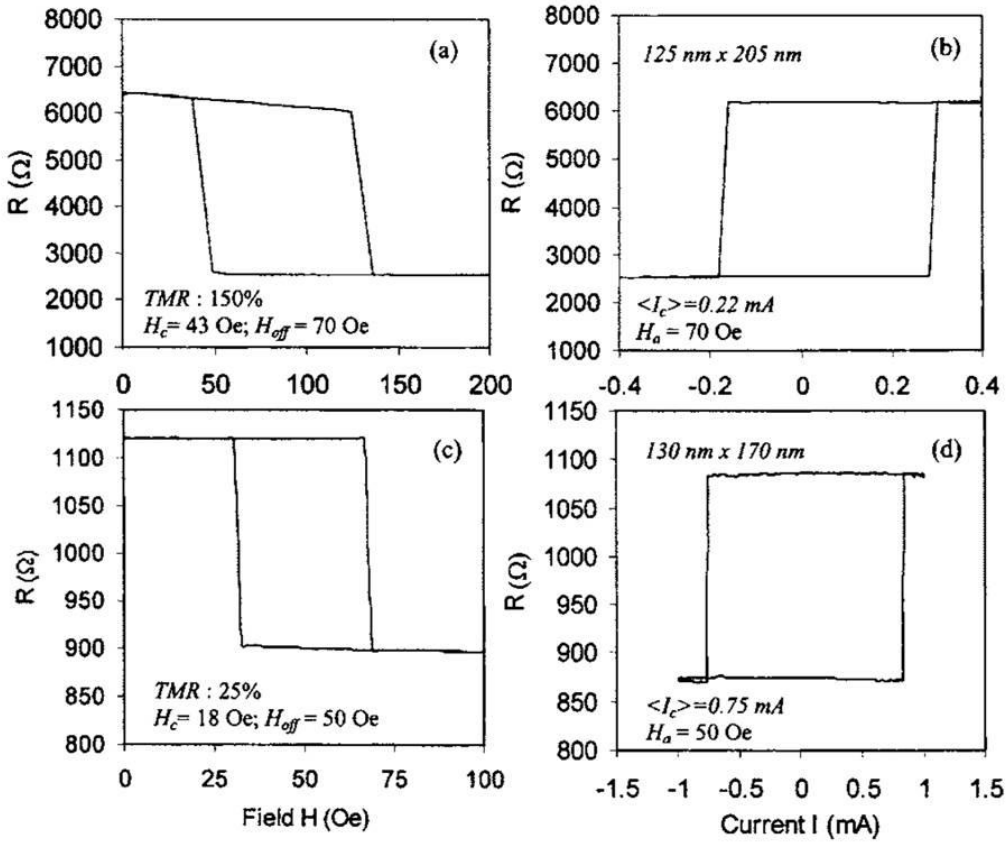

Figure 2-9. Field and current driven magnetization switching in an MgO or AlO_x barrier. Typical (a) field and (b) current driven magnetization switching for an MTJ sample with an MgO barrier, and (c) field and (d) current driven magnetization switching for an MTJ sample with an AlO*x* barrier. Current pulse width of 30 ms was used in obtaining (b) and (d) (From Ref. 55).

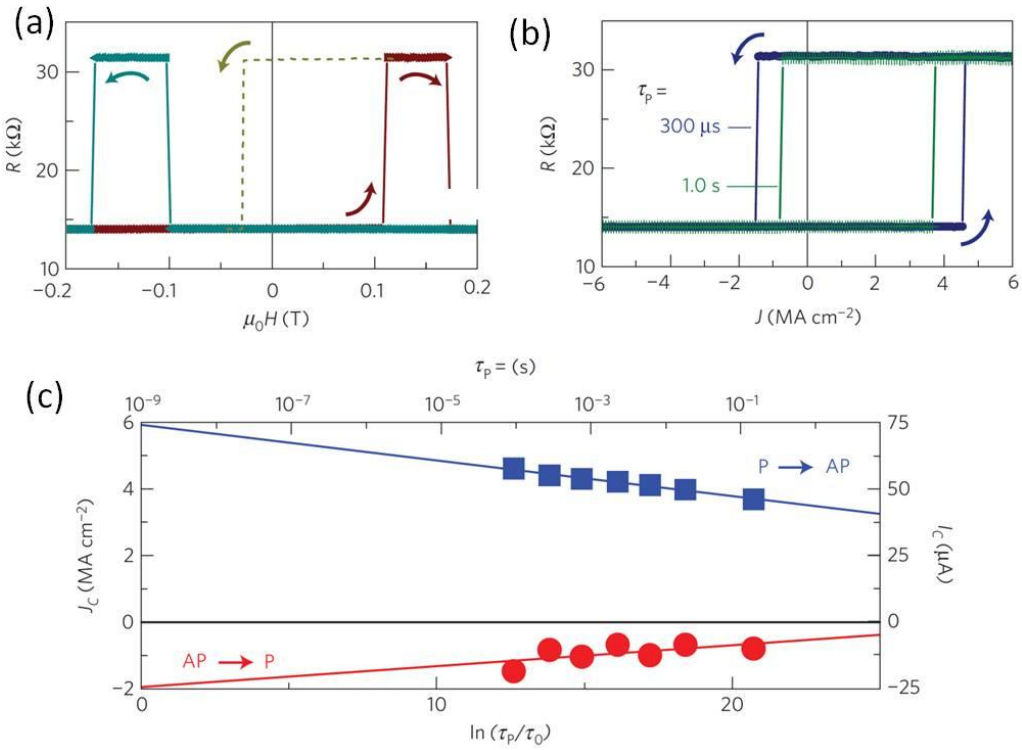

Figure 2-10. Field and current driven magnetization switching in p-MTJs (a) Perpendicular *R–H* curve. The filled symbols and dashed line represent major and minor loops respectively. The arrows show the *H* sweep direction. (b) Typical results of current induced magnetic switching at current pulse durations of 300 μs and 1.0 s. (c) J_C as a function of $\ln(\tau_P/\tau_0)$ from which E/k_BT and J_{C0} are determined (From Ref. 37).

2.5 Other spin effects

As mentioned above, the usual way to generate and detect spin currents by a two-terminal MTJ with a layered FM/ I /FM structure. However, other effects also have been observed in a metal based ferromagnetic system, here I briefly introduce a few of them, which have potential applications in future spintronics.

2.5.1 Spin Hall effect

In the Hall effect, when a conductor/semiconductor is subject to orthogonal electric and magnetic fields, opposite charges will accumulate at the edges of a conductor/semiconductor due to the Lorentz force. In the spin Hall effect, spin accumulation occurs as a result of a charge current in the presence of a spin-orbit interaction [60]. Such a process is represented schematically in Figure 2-11(a). Two different types of SHE (intrinsic and extrinsic) have been recently proposed and observed in experiments. The intrinsic effect is caused by the spin-orbit splitting in the band structure of the non-magnetic material and is independent on disorder [61], whereas the extrinsic SHE is due to scattering by impurities, typically includes the skew scattering and side-jump [62].

Recent studies have demonstrated that the magnitudes of the spin Hall angles in the 5d elements Pt [63-66] and high resistivity β-Ta [67] and β-W [68] can be relatively large spin Hall angle , with θ_{Pt} =0.07 , $\theta_{\beta\text{-}Ta}$=-0.15 and $\theta_{\beta\text{-}W}$=-0.30. The resulting spin currents are sufficiently strong to be of interest for magnetization manipulation via the spin transfer torque mechanism, opening the possibility of an efficient way to implement spintronics technologies. For example, a three-terminal device, can use the current passing through a tantalum-ferromagnet bilayer to switch a adjacent nanomagnet. A MTJ that incorporates the nanomagnet as a free layer can provide a readout of the free layer magnetic orientation, resulting in a simple, reliable, and efficient design that may eliminate some of obstacles to the successful

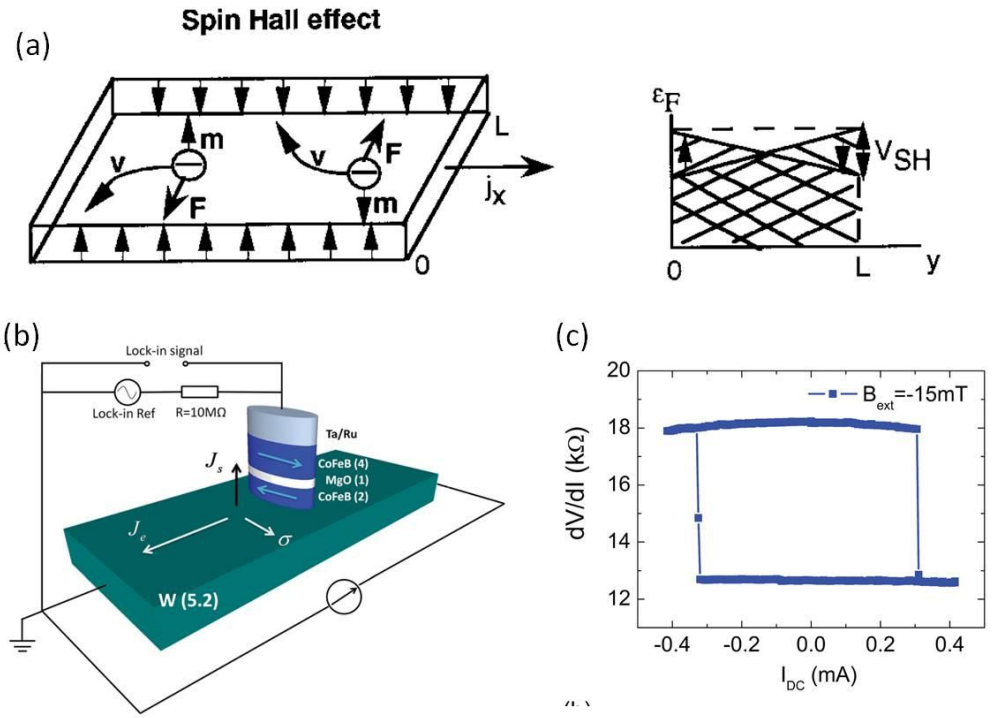

Figure 2-11. Spin Hall effect. (a) Schematic of the spin Hall effect: spin accumulation is induced at the edges of the sample due to spin-orbit interaction when a pure charge current is applied [Ref. 60]. (b) Schematic illustration of the β-W 3-terminal device and the measurement circuit layout. (c) Differential resistance (dV/dI) of the MTJ as a function of the DC bias current I_{DC}, exhibiting magnetization switching by the spin Hall torque (From Ref. 68).

development of magnetic memory and nonvolatile spin logic technologies. (See Figure 2-11(b-c)).

As mentioned above, in spin Hall effect, a spin-polarized current can exert a torque on the magnetization of a ferromagnet, leading to current-induced magnetic switching. The inverse of this process is the interfacial "pumping" of spins into adjacent nonmagnetic layers due to the precessing magnetization of a ferromagnet,

resulting in an electric potential difference between the opposite edges of the nonmagnetic layer. This process is considered as the inverse spin Hall effect and can be used as a method for the electrical detection of spin-currents [69-70].

2.5.2 Exchange spring effect

Antiferromagnetic materials play an important role in technology and in basic sciences. However, the vanishing magnetization caused by their compensated magnetic structure makes it difficult to study. Particularly interesting effects occur at the boundary of an antiferromagnet (AFM) and a ferromagnet (FM). A prominent example is exchange bias. Scholl et al. [71] show that an exchange-coupled ferromagnet/antiferromagnet system behaves similar to an antiferromagnetic exchange spring magnet, very similar to ferromagnetic spring magnets that consist of coupled soft and hard-magnetic ferromagnets [72-73]. As in a ferromagnetic spring magnet, a planar domain wall is wound up in the antiferromagnet when the magnetization of the ferromagnet is rotated or switched, as illustrated in Figure 2-12(a). This effect was observed in the system Co/NiOx, which is a fundamental assumption in magnetic models of exchange bias.

Based on the exchange spring effect, Park et al. [74] demonstrate more than 100% spin-valve-like signal in a NiFe/IrMn/MgO/Pt stack with an antiferromagnet on one side and a nonmagnetic metal on the other side of the tunnel barrier. (As shown in the Figure 2-12(b)). Ferromagnetic moments in NiFe are reversed by external fields, and the exchange-spring effect of NiFe on IrMn induces rotation of antiferromagnetic moments in IrMn, which is detected by the measured tunneling anisotropic

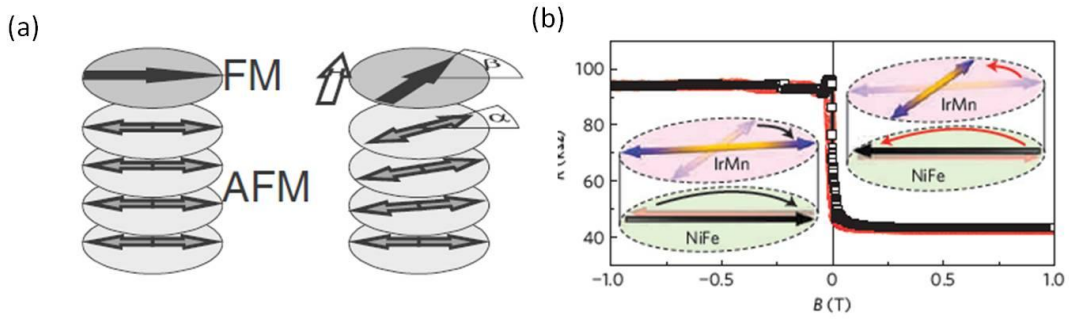

Figure 2-12. Exchange spring effect. (a) Creation of an antiferromagnetic exchange spring: FM rotates into field direction and creates a planar domain wall in the exchange-coupled AFM (From Ref. 71). (b) A spin-valve-like signal in the NiFe/IrMn(1.5nm)/MgO/Pt AFM tunnel device**:** 130% magnetoresistance signal recorded in the range of -1 to +1 T field on a tunneling device fabricated in the depicted multilayer structure with the NiFe/IrMn(1.5 nm)/MgO/Pt tunnel junction. The direction of the in-plane magnetic field corresponds to the direction of the magnetic field applied during the film growth. The insets illustrate the rotation of AFM moments in IrMn through the exchange-spring effect of the adjacent NiFe ferromagnet. The external magnetic field is sensed by the NiFe ferromagnet whereas the tunneling transport is governed by the IrMn antiferromagnet (From Ref. 74).

magnetoresistance. Their work shows that efficient rotation of staggered moments in the antiferromagnet can be induced by the exchange spring effect of the adjacent FM layer. With only one magnetic electrode in the tunnel junction simultaneously large anisotropic magnetoresistance and low switching fields were achieved, demonstrating the potential of antiferromagnets for spintronics.

2.5.3 Spin Seebeck effect

Spintronics combines the spin with charge, and is mainly concerned with the coupled electron spin and charge transport properties. Recently, the researchers

discovered the interaction of spins with heat currents [76-77], which has a great potential application in thermoelectric devices. The spin Seebeck, spin Peltier, thermal conductance, and thermal spin-transfer torques have all been studied intensively in recent years.

In the Seebeck effect, heat applied to a conductor will produce a difference of temperature across the conductor, and this temperature difference can induce an electrical current. The strength of this current is characterized by the Seebeck coefficient which can be defined by the ratio of the induced voltage and the temperature differences. For the spin Seebeck effect, a spin current potential can be defined by $\mu_{\uparrow} - \mu_{\downarrow}$, where $\mu_{\uparrow}$ and $\mu_{\downarrow}$ are the electrochemical potentials of spin-up and spin-down electrons, respectively. In a metallic magnet, if the scattering rates and densities of spin-up and spin-down conduction electrons are different, the spin-up and spin-down conduction electrons would have different Seebeck coefficients. A spin current potential can thus be induced when there is a temperature difference. The spin-Seebeck coefficient is defined as:

$$S_s = \frac{\mu_{\uparrow} - \mu_{\downarrow}}{\Delta T} \tag{2.1}$$

Recently, many researchers have reported results of the spincaloric effect in MTJs both from theoretical and experimental point of view. Liebing et al. [80], using

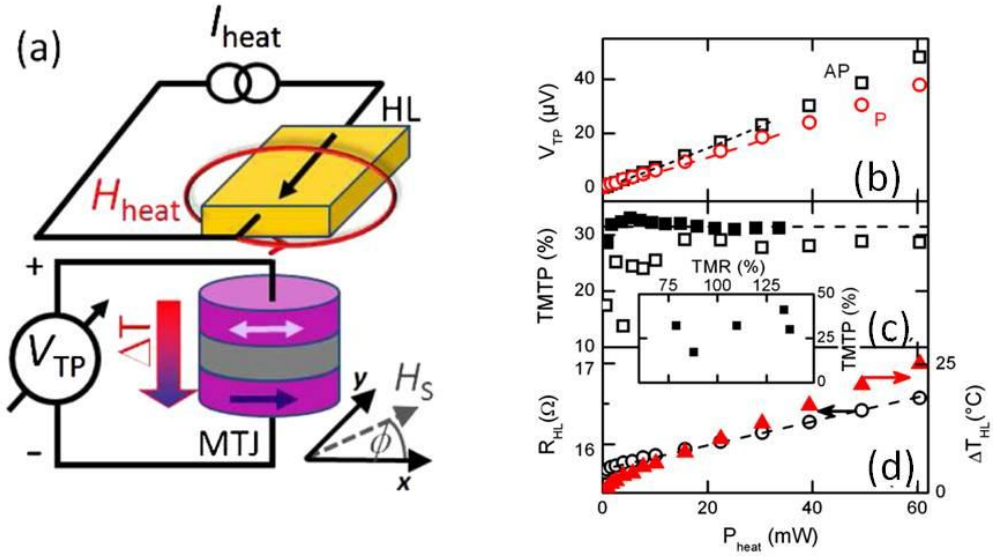

Figure 2-13. Spin Seebeck effect. (a) Sketch of tunneling magneto thermopower setup. A current I_{heat} through the HL creates a temperature gradient across the CoFeB/MgO/CoFeB MTJ and the thermovoltage V_{TP} is measured in in-plane magnetic fields H_S. (b) V_{TP} as function of P_{heat} for parallel (P, red circles) and antiparallel (AP, black squares) orientation of MTJ. dc (symbols) and ac (lines) data agree. (c) TMTP ratio vs P_{heat} for ac (full squares) and dc measurements (open squares). Inset: TMTP vs. TMR of the devices of Table I. (d) HL resistance R_{HL} (left scale, circles) and increase of HL temperature ΔT_{HL} (right scale, triangles) as a function of P_{heat} (From Ref. 80).

CoFeB/MgO/CoFeB MTJs, studied the tunneling magneto thermopower. The structures in their experiment are shown in Figure 2-13(a). Figure 2-13(b) shows the relation of V_{TP} (P, AP) as a function of P_{heat}. With increasing P_{heat}, V_{TP} (P) and V_{TP}(AP) increase linearly relatively. Figure 41(c) shows the tunneling Magneto-thermopower (TMTP) at different P_{heat}. In their work, a tunneling magneto thermopower of about 32% was observed, making them a promising candidate for spin caloritronics.

In 2012 Jaworski et al. [81] propose that the giant spin Seebeck effect is mediated by phonon–electron drag, which changes the electrons' momentum and directly modifies the spin-splitting energy through spin–orbit interactions. Thus the giant spin Seebeck voltage in non-magnetic material inSb was observed with the magnitude of comparable to the largest known classical thermopower values, owing to the simultaneously strong phonon–electron drag and spin–orbit coupling in InSb.

BIBLIOGRAPHY

1. Julliere M. Tunneling between ferromagnetic films. *Phys Lett* A 54, 225 (1975).

2. Grünberg P, Schreiber R, Pang Y, et al. Layered magnetic structures, Evidence for antiferromagnetic coupling of Fe layers across Cr interlayers. *Phys Rev Lett*, 57, 2442 (1986).

3. Binasch G, Grünberg P, Saurenbach F, et al. Enhanced magnetoresistance in layered magnetic structures with antiferromagnetic interlayer exchange. *Phys Rev B*, 39, 4828 (1989).

4. Baibich M N, Broto J M, Fert A, et al. Giant magnetoresistance of (001)Fe/(001)Cr magnetic superlattices. *Phys Rev Lett*, 61, 2472 (1988).

5. Parkin S S P, Li Z G, Smith D J. Giant magnetoresistance in antiferromagentic Co/Cu multilayers. *Appl Phys Lett*, 58, 2710 (1991).

6. Daughton J, Brown J, Chen E, et al. Magnetic-field sensors using GMR multilayer. *IEEE Trans Magn*, 30, 4608 (1994).

7. Reig C, Cubells-Beltrán M, Muñoz D R. Magnetic field sensors based on giant magnetoresistance (GMR) technology, Applications in electrical current sensing. *Sensors*, 9, 7919 (2009).

8. Miyazaki T, Tezuka N. Giant magnetic tunneling effect in Fe/Al2O3/Fe junction. *J Magn Magn Mater*, 139, L231(1995).

9. Moodera J S, Kinder L R, Wong T M, et al. Large magnetoresistance at RT in ferromagnetic thin film tunnel junctions. *Phys Rev Lett*, 74, 3273 (1995).

10. Wei H X, Qin Q H, Ma M, et al. 80% tunneling magnetoresistance at RT for thin Al–O barrier magnetic tunnel junction with CoFeB as free and reference layers. *J Appl Phys*, 101,09B501(2007).

11. Mathon J, Umerski A. Theory of tunneling magnetoresistance of an epitaxial Fe/MgO/Fe(001) junction. *Phys Rev B*, 63, 220403(R)(2001).

12. Parkin S S P, Kaiser C, Panchula A, et al. Giant tunnelling magnetoresistance at RT with MgO(100) tunnel barriers. *Nat Mater*, 3, 862 (2004).

13. Yuasa S, Nagahama T, Fukushima A, et al. Giant room-temperature magnetoresistance in single-crystal Fe/MgO/Fe magnetic tunnel junctions. *Nat Mater*, 3, 868 (2004).

14. Ikeda S, Hayakawa J, Ashizawa Y, et al. Tunnel magnetoresistance of 604% at 300 K by suppression of Ta diffusion in CoFeB/MgO/CoFeB pseudo-spin-valves annealed at high temperature. *Appl Phys Lett*, 93, 082508 (2008).

15. Yuasa S, Djayaprawira D D. Giant tunnel magnetoresistance in magnetic tunnel junctions with a crystalline MgO(001) barrier. *J Phys D-Appl Phys*, 40, R337(2007).

16. Butler W, Zhang X G, Schulthess T C, et al. Spin-dependent tunneling conductance of Fe|MgO|Fe sandwiches. *Phys Rev B*, 63, 054416(2011).

17. Miao G, Chetry K B, Gupta A, et al. Inelastic tunneling spectroscopy of magnetic tunnel junctions based on CoFeB/MgO/CoFeB with Mg insertion layer. *J Appl Phys*, 99, 08T305222503 (2006).

18. Huang J C A, Hsu C Y, Chen W H, et al. Effects of submonolayer Mg on CoFe-MgO-CoFe magnetic tunnel junctions. *J Appl Phys*,104,073909 (2008).

19. Wang Y, Zhang J, Zhang X G, et al. First-principles study of Fe/MgO based magnetic tunnel junctions with Mg interlayers. *Phys Rev B*, 82, 054405 (2010).

20. Zhang X G, Butler W H, Bandyopadhyay A. Effects of the iron-oxide layer in Fe-FeO-MgO-Fe tunneling junctions. *Phys Rev B*, 68, 092402 (2003).

21. Tusche C, Meyerheim H L, Jedrecy N, et al. Oxygen-induced symmetrization and structural coherency in Fe/MgO/Fe(001) magnetic tunnel junctions. *Phys Rev Lett*, 95, 176101(2005).

22. Heiliger C, Zahn P, Yavorsky B Y, et al. Influence of the interface structure on the bias dependence of tunneling magnetoresistance. *Phys Rev B*, 72, 180406(R)(2005).

23. Tiusan C, Faure-Vincent J, Bellouard C, Hehn M, Jouguelet E, and Schuhl A Interfacial resonance state probed by spin-polarized tunneling in epitaxial Fe/MgO/Fe tunnel junctions, *Phys Rev Lett*, 93, 106602 (2004).

24. Unguris J, Celotta RJ, and Pierce DT, Magnetism in Cr thin films on Fe(100) , *Phys. Rev. Lett.* 69,1125 (1992).

25. Zhang J, Wang Y, Zhang X G, et al. Inverse and oscillatory magnetoresistance in Fe(001)/MgO/Cr/Fe magnetic tunnel junctions. *Phys Rev B*, 82, 134449 (2010).

26. Matsumoto R, Fukushima A, Yakushiji K, et al. Spin-dependent tunneling in epitaxial Fe/Cr/MgO/Fe magnetic tunnel junctions with an ultrathin Cr(001) spacer layer. *Phys Rev B*, 79, 174436 (2009).

27. Y. Lu, H.-X. Yang, C. Tiusan, M. Hehn,M. Chshiev,A. Duluard,B. Kierren, G. Lengaigne,D. Lacour,C. Bellouard,and F. Montaigne Spin-orbit coupling effect by minority interface resonance states in single-crystal magnetic tunnel junctions. *Phys Rev B*, 86, 184420 (2012).

28. Mangin S, Ravelosona D, Katine J A, et al. Current-induced magnetization reversal in nanopillars with perpendicular anisotropy. *Nat Mater*, 5, 210 (2006).

29. Meng H, Wang J P. Spin transfer in nanomagnetic devices with perpendicular anisotropy. *Appl Phys Lett*, 88, 172506 (2006).

30. Law R, Sbiaa R, Liew T, et al. Effects of Ta seed layer and annealing on magnetoresistance in CoFe/Pd-based pseudo-spin-valves with perpendicular anisotropy. *Appl Phys Lett*, 91, 242504 (2007).

31. Shimabukuro, R., Nakamura, K., Akiyama, T. & Ito, T. Electric field effects on magnetocrystalline anisotropy in ferromagnetic Fe monolayers. *Physica E*, 42, 1014 (2010).

32. Monso, S. et al. Crossover from in-plane to perpendicular anisotropy in Pt/CoFe/AlOx sandwiches as a function of Al oxidation, A very accurate control of the oxidation of tunnel barrier. *Appl. Phys. Lett.,* 80, 4157 (2002).

33. Manchon, A. et al. Analysis of oxygen induced anisotropy crossover in Pt/Co/MOx trilayers. *J. Appl. Phys*.104, 043914 (2008).

34. Ohmori H, Hatori T, Nakagawa S. Perpendicular magnetic tunnel junction with tunneling magnetoresistance ratio of 64% using MgO(100) barrier layer prepared at RT. *J Appl Phys*, 103,07A911(2008).

35. Yoshikawa M, Kitagawa E, Nagase T, et al. Tunnel magnetoresistance over 100% in MgO-based magnetic tunnel junction films with perpendicular magnetic L10-FePt electrodes. *IEEE Trans Magn*, 44, 2573(2008).

36. Mizunuma K, Ikeda S, Park J H, et al. MgO barrier-perpendicular magnetic tunnel junctions with CoFe/Pd multilayers and ferromagnetic insertion layers. *Appl Phys Lett*, 95, 232516(2009).

37. Ikeda S, Miura K, Yamamoto H, et al. A perpendicular-anisotropy CoFeB-MgO magnetic tunnel junction. *Nat Mater* , 9, 721 (2010).

38. Wang W X, Yang Y, Naganuma H, et al. The perpendicular anisotropy of Co40Fe40B20 sandwiched between Ta and MgO layers and its application in CoFeB/MgO/CoFeB tunnel junction. *Appl Phys Lett*, 99, 012502 (2011).

39. Sato H, Yamanouchi M, Miura K, et al. Junction size effect on switching current and thermal stability in CoFeB/MgO perpendicular magnetic tunnel junctions. *Appl Phys Lett*, 99, 042501(2011).

40. Duan C G, Velev J P, Sabirianov R F, et al. Tailoring magnetic anisotropy at the ferromagnetic/ferroelectric interface. *Appl Phys Lett*, 92, 122905 (2008).

41. Duan C G, Jaswal S S, Tsymbal E Y. Predicted magnetoelectric effect in Fe/BaTiO3 multilayers, Ferroelectric control of magnetism. *Phys Rev Lett*, 97, 047201(2006).

42. Niranjan M K, Duan C G, Jaswal S S, et al. Electric field effect on magnetization at the Fe/MgO(001) interface. *Appl Phys Lett*, 96, 222504(2010).

43. Wang W G, Li M, Hageman S, et al. Electric-field-assisted switching in magnetic tunnel junctions. *Nat Mater*, 11, 64 (2012).

44. Shiota Y, Nozaki T, Bonell F, et al. Induction of coherent magnetization switching in a few atomic layers of FeCo using voltage pulses. *Nat Mater*, 11, 39 (2012).

45. Kim G, Sakuraba Y, Oogane M, et al. Tunneling magnetoresistance of magnetic tunnel junctions using perpendicular magnetization L10-CoPt electrodes. *Appl Phys Lett*, 92, 172502 (2008).

46. Watanabe D, Mizukami S, Oogane M, et al. Fabrication of MgO-based magnetic tunnel junctions with CoCrPt perpendicularly magnetized electrodes. *J Appl Phys*, 105, 07C91147 (2009).

47. Slonczewski JC, Current-driven excitation of magnetic multilayers. *Journal of Magnetism and Magnetic Materials*, 39(1-2), 4984–L7, (1996).

48. Berger L, Emission of spin waves by a magnetic multilayer traversed by a current. *Physical Review B*, 54, 9353 (1996).

49. Katine J A, Albert F J, Buhrman R A, et al. Current-driven magnetization reversal and spin-wave excitation in Co/Cu/Co pillars. *Phys Rev Lett*, 84, 3149 (2000).

50. Grollier J, Cros V, Hamzic A, et al. Spin-polarized current induced switching in Co/Cu/Co pillars. *Appl Phys Lett*, 78, 3663(2001).

51. Sun J Z, Monsma D J, Abraham D W et al. Batch fabricated spin injection magnetic switches. *Appl Phys Lett*, 81,2202 (2002).

52. Diao Z T, Panchula A, Ding Y, et al. Spin transfer switching in dual MgO magnetic tunnel junctions. *Appl Phys Lett* , 90, 132508 (2007).

53. Finocchio G, Consolo G, Carpentieri M, et al. Trends in spintransfer-driven magnetization dynamics of CoFe/AlO/Py and CoFe/MgO/Py magnetic tunnel junctions. *Appl Phys Lett* , 89, 262509 (2006).

54. Kubota H, Fukushima A, Yakushiji K, et al. Quantitative measurement of voltage dependence of spin-trnasfer torque in MgO-based magnetic tunnel junctions, *Nat Phys*, 4, 37 (2008).

55. Diao Z, Apalkov D, Pakala M, et al. Spin transfer switching and spin polarization in magnetic tunnel junctions with MgO and AlO*x* barriers. *Appl Phys Lett*, 87, 232502 (2005).

56. Deac A M, Fukushima A, Kubota H, et al. Bias-driven high-power microwave emission from MgO-based tunnel magnetoresistance devices. *Nat Phys*, 4, 803 (2008).

57. Oh S C, Park, S. Y. Manchon, A. Chshiev, M. Han, J. H. Lee, H. W. Lee, J. E. Nam, K. T. Jo, Y. Kong, Y. C. Dieny, B. Lee, K. J. Bias-voltage dependence of perpendicular spin-transfer torque in asymmetric MgO-based magnetic tunnel junctions. *Nature Physics* **5**(12), 898 (2009).

58. Wang C, Cui Y T, Sun J Z, Katine J A, Buhrman R A, and Ralph D C. Bias and angular dependence of spin-transfer torque in magnetic tunnel junctions. *Physical Review B*, 79(22), 1 (2009).

59. Wang C, Cui Y T, Sun J Z, Katine J A, Buhrman R A, and Ralph D C. Time-resolved measurement of spin-transfer-driven ferromagnetic resonance and spin torque in magnetic tunnel junctions. *Nature Physics*, 7, 496 (2011).

60. Hirsch J E. Spin hall effect. *Phys Rev Lett*, 83, 1834 (1999).

61. Tse W K, Das Sarma S. Intrinsic spin Hall effect in the presence of extrinsic spin-orbit scattering. *Phys Rev B*, 74, 245309 (2006).

62. Tse W K, Fabian J, Žutić I, et al. Spin accumulation in the extrinsic spin Hall effect. *Phys Rev B*, 72, 241303 (2005).

63. Kimura T, Otani Y, Sato T, Takahashi S, and Maekawa S, Room-Temperature Reversible Spin Hall Effect *Phys. Rev. Lett*. 98, 156601 (2007).

64. Ando K, Takahashi S, Harii K, Sasage K, Ieda J, Maekawa S, and Saitoh E, *Phys. Rev. Lett.* 101, 036601 (2008).

65. Mosendz O, Pearson J E, Fradin F W, Bauer G E W, Bader S D, and Hoffmann A, *Phys. Rev. Lett.* 104, 046601 (2010).

66. Liu LQ, Moriyama T, Ralph D. C., and Buhrman R. A., *Phys. Rev. Lett.* 106, 036601 (2011).

67. Liu L. Q., Pai C. F., Li Y., Tseng H. W., Ralph D. C., and Buhrman R. A., *Science* 336, 555 (2012).

68. Pai C. F., Liu L., Li Y., Tseng H. W., Ralph D. C., Buhrman R. A. Spin transfer torque devices utilizing the giant spin Hall effect of tungsten *Appl. Phys. Lett.* 101, 122404 (2012).

69. Czeschka, F., Dreher, L., Brandt, M., Weiler, M., Althammer, M., Imort, I.-M., Reiss, G., et al. Scaling Behavior of the Spin Pumping Effect in Ferromagnet-Platinum Bilayers. *Phys Rev Lett*.107.046601 (2011).

70. Azevedo, a., Vilela-Le ão, L., Rodr íguez-Su árez, R., Lacerda Santos, a., & Rezende, S.. Spin pumping and anisotropic magnetoresistance voltages in magnetic bilayers, Theory and experiment *Phys Rev B*, 83, 144402(2011).

71. A. Scholl, M. Liberati,E. Arenholz, H. Ohldag, and J. Stohr Creation of an Antiferromagnetic Exchange Spring, *Phys Rev Lett*, 92, 247201 (2004).

72. E. F. Kneller and R. Hawig, IEEE Trans. Magn. **27**, 3588 (1991).

73. E. E. Fullerton, J. S. Jiang, M. Grimsditch, C. H. Sowers, and S. D. Bader, *Phys. Rev. B* **58**, 12 193 (1998).

74. B. G. Park, J.Wunderlich, X. Mart í, V. Hol ý, Y. Kurosaki, M. Yamada, H. Yamamoto,Nishide, J. Hayakawa, H. Takahashi, A. B. Shick and T. Jungwirth A spin-valve-like magnetoresistance of an antiferromagnet-based tunnel junction, *Nat Mater*,10, 347 (2011).

75. Bauer G E W. Spin caloritronics. *Nat Mater*,11, 391(2012).

76. Uchida K, Takahashi S, Harii K, et al. Observation of the spin Seebeck effect. *Nature*, 455, 778 (2008).

77. Uchida K, Xiao J, Adachi H, et al. Spin seebeck insulator. *Nat Mater*, 9, 894 (2010).

78. Jaworski C M, Yang J, Mack S, et al. Observation of the spin-Seebeck effect in a ferromagnetic. *Nat Mater*, 9, 898 (2010).

79. Han, X., Ali, S. S., & Liang, S. MgO(001) barrier based magnetic tunnel junctions and their device applications. *Science China Physics, Mechanics and Astronomy*, *56*, 29 (2012).

80. Liebing, N., Serrano-Guisan, S., Rott, K., Reiss, G., Langer, J., Ocker, B., & Schumacher, H. W. Tunneling Magnetothermopower in Magnetic Tunnel Junction Nanopillars. *Physical Review Letters*, 107, 177201 (2011).

81. Jaworski, C. M., Myers, R. C., Johnston-Halperin, E., & Heremans, J. P. Giant spin Seebeck effect in a non-magnetic material. *Nature*, 487(7406), 210 (2012).

CHAPTER 3

SAMPLE PREPARATION AND MEASUREMENT

The performance of our devices is sensitive to the deposition condition and fabrication procedure. In this chapter, I will discuss the details of the thin film deposition in our AJA sputtering system, and micron-size or nano-size fabrication process. Finally I will introduce the background of the measurement methods that I used in my experiments that are discussed in the following chapters.

3.1 Thin film growth-sputtering in the AJA

3.1.1 MgO based magnetic tunnel junction

The standard MgO based MTJs that I studied were grown in the AJA sputtering system with a structure as follows: substrate/ bottom contact/fixed magnetic layer/ MgO/free layer/top contact. I have achieved reliable and repeatable high TMR(>100%) CoFeB-based MgO MTJs in our sputtering system. For example, one typical layer structure of our MTJ devices is Ta 5nm /Ru 15nm /Ta 5nm/ IrMn 10nm/ FeCoB 4nm / MgO 2nm / FeCoB 3nm/ Ru 8nm / Ta 7nm. The sputtering conditions that I used are provided in Table 3-1. The composition of the films was confirmed by secondary ion mass spectrometry (SIMS) measurements (see Figure 3-1).

	Ta	Ru	Ta	IrMn	FeCoB	MgO	FeCoB	Ta	Ru
Pressure(mTorr)	2	2	2	2	2	2	2	2	2
Power (W)	100	100	100	100	75	100	75	100	100
Current (mA)	329	292	329	262	200	-	200	329	292
Voltage(V)	311	338	311	378	374	388	374	311	338
Time (s)	120	588	120	128	178	420	134	96	118
Thickness (nm)	5	15	5	10	4	2	3	4	3

Table 3-1. **A standard CoFeB-based MgO MTJ sputtering multilayer stack structure and sputtering parameters.** The MgO tunnel barrier is deposited by RF sputtering and other layers are formed by DC sputtering.

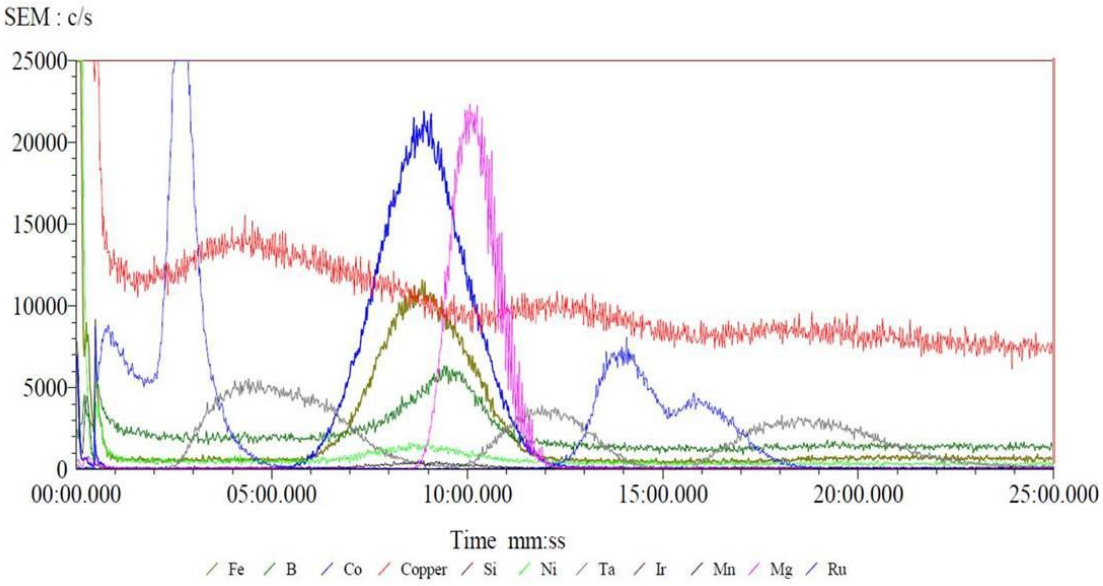

Figure 3-1. SIMS data of the standard CoFeB-based MgO MTJ during the ion mill etching. With the time increasing, the elements show up from the top layers to the bottom contact.

The bottom contact also works as a seed layer to provide a smoother interface for the subsequently deposited magnetic tunnel junction MTJ. The typical bottom layers I used were Ta 5nm/ Ru 15nm/Ta 5nm or Ta 5nm / Cu (CuN) 20nm /Ta 5nm with surface roughness less then 1nm, which was confirmed by the AFM measurement. The RA-product from those bottom layers is less than $1\Omega \cdot \mu m^2$, so the resistance of bottom contact layers could be negligible when the RA products of the tunnel barrier is larger than $10\Omega \cdot \mu m^2$. I also tried the use of a single 15nm Ta layer as the bottom contact, and still obtained a TMR >100% in the patterned devices. However, due to the high resistivity of the β-phase Ta, the contact resistance of the device is a consideration in this case, particularly since it typically increases after the annealing process. I suspect that this is due to the reaction of Ta and the SiOx substrate, possibly resulting in the formation of TaOx through the whole layer during the annealing, while in the Ta /Ru / Ta structure, the oxidation is stopped at the first Ta/Ru interface.

The fixed magnetic layer, the tunnel barrier and the free magnetic layer are the most crucial layers in the MTJ devices. To get one ferromagnetic layer fixed, I use IrMn/FeCoB as the pinned layer or simply grow one layer much thicker than the other. With 10nm IrMn, the pinning field is about 500 Oersted as measured by the H-R major loop. In my research I have studied junctions with $Fe_{20}Co_{60}B_{20}$, $Fe_{40}Co_{40}B_{20}$ and $Fe_{60}Co_{20}B_{20}$ as the magnetic layer. High TMR (> 100%) has been achieved in all the cases, but it seems that the MTJs with $Fe_{40}Co_{40}B_{20}$ have the largest coercivity in the H-R minor loop in the annealed devices, which indicates that $Fe_{50}Co_{50}$ has the strongest in-plane crystalline anisotropy. In order to get a reliable deposition process,

the sputtering power of MgO is reduced from the 300W to the 100W [1]. Under that condition, reliable TMR (>100%) is achieved with RA-product varying from $10\Omega\cdot\mu m^2$ to $10^7\Omega\cdot\mu m^2$, controlled by varying the deposition time roughly between 4 minutes and 13 minutes. Low RA-product ($<10\ \Omega\cdot\mu m^2$) devices were obtained in our MgO wedged films, however, the TMR then is also decreased. For example, a sample with RA~ $5\Omega\cdot\mu m^2$ had TMR about 50%. I suspect that pin holes through the barrier may begin to play a more significant role when the MgO becomes thinner (< 0.9nm, about two atomic layer). Since previous theoretical study suggests that the $Mg_3B_2O_6$ could also a good spin filter [2], I also used $Mg_3B_2O_6$ target to grow the tunnel barrier. After a 350℃ annealing process, STEM studies indicated that the $Mg_3B_2O_6$ tunnel barrier was amorphous but did have a TMR ~40%. That result is shown in Figure 3-2.

The capping layers in our MTJ devices are Ta and Ru. I choose Ru as the top layer for two reasons: first, it is stable in the air, and RuO_x is still conductive, so it makes the air annealing process possible. Second, the omnicoat, which I will mention in the fabrication section, adheres well on the Ru. Our results show that 3nm Ta/ 4nm Ru is thick enough to protect the underneath layers, but not too thick to do the lift-off process.

3.1.2 Tungsten based spin Hall devices

In the spin Hall effect experiment, the spin current is generated in the spin hall material, and detected by it effect on a adjacent ferromagnetic layer. Here I choose

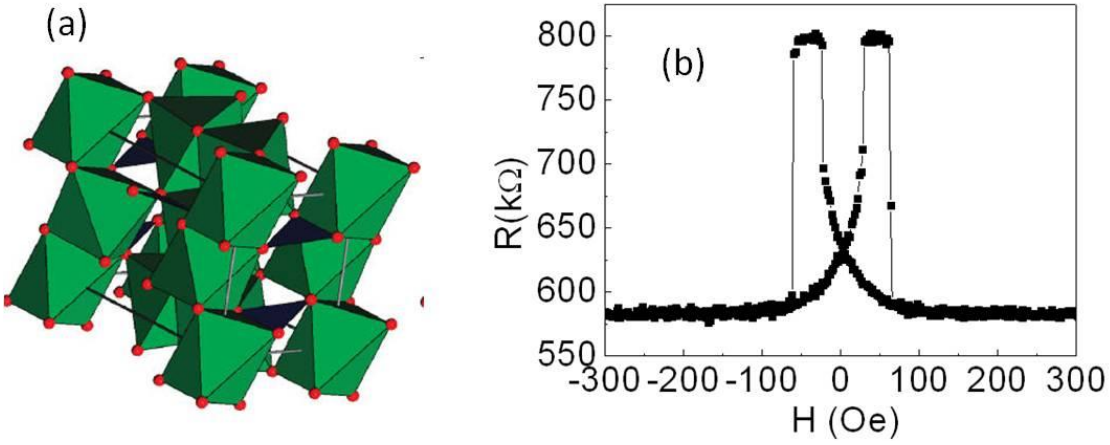

Figure 3-2 $Mg_3B_2O_6$ based MTJs (a) The lattice structure of $Mg_3B_2O_6$ and (b) the major R-H loop of $Mg_3B_2O_6$ based MTJs.

tungsten (W) as our spin hall material due to its large spin Hall angle measured by both ST-FMR and current switching measurements [3]. Since the phase of the W is really sensitive to the thickness of the thin film, in order to control the W thickness accurately, low power 30W was used during the DC sputtering. In this study, $Fe_{40}Co_{40}B_{20}$ was utilized as the ferromagnetic layer in most cases, but Py was also deposited for comparison. The thickness of the FeCoB varies from 0.7nm to 10nm to control its crystalline anisotropy, and a small DC power 30W is applied to get the lower deposition rate during the sputtering.

One possible issue in the thin film quality in my spin Hall studies is the roughness of the W surface. Figure. 3-2 shows the electron microscopy of X-ray mapping of substrate/W 4nm/FeCoB 5nm/Ta 1nm sample (Data are taken by Paul Cueva in Prof. Muller's group). Here 1nm Ta is capped to protect the FeCoB underneath, and EELS data suggest that Ta is fully oxidized, thus no spin current

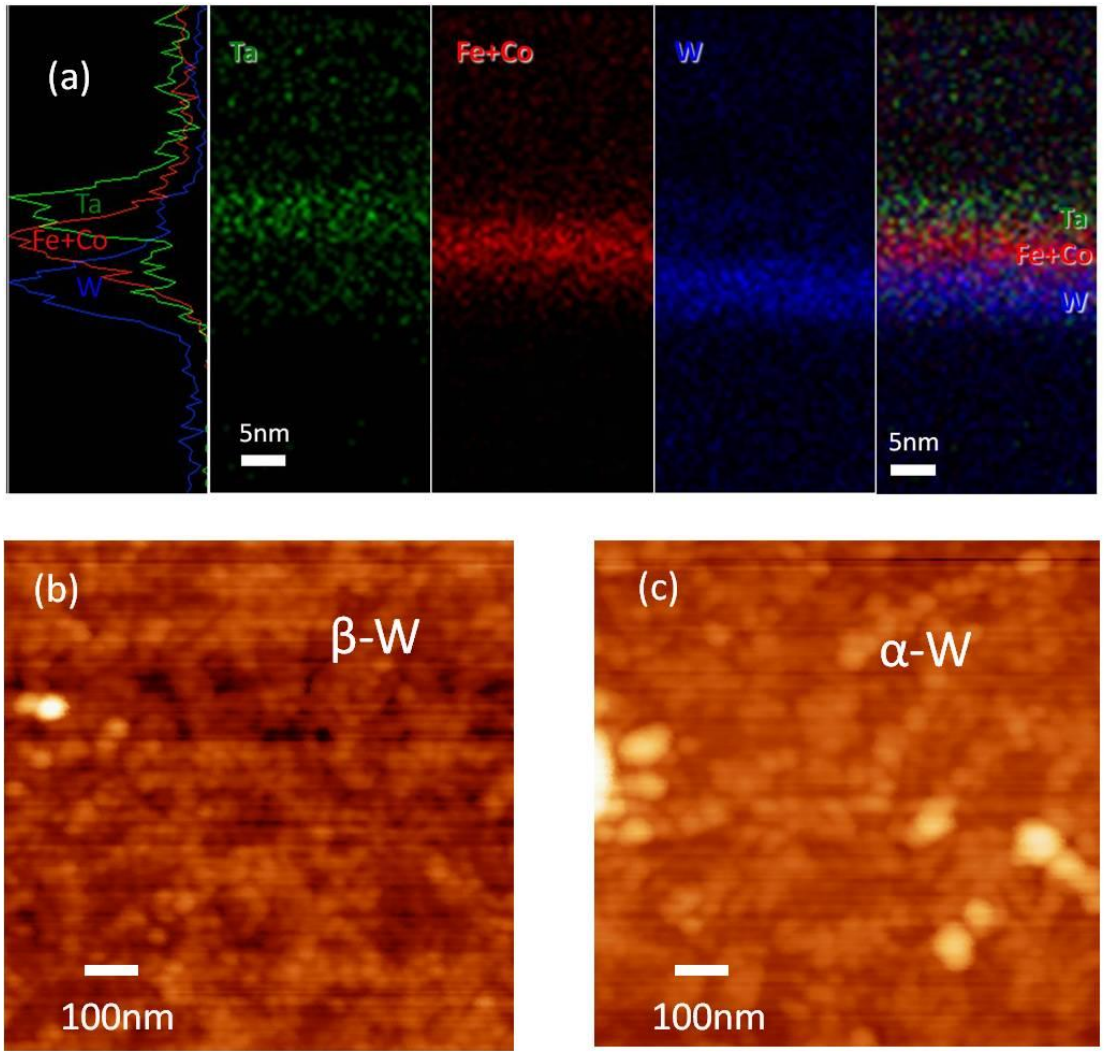

Figure 3-3. Electron microscopy and AFM images of W/ FeCoB structure (a) Electron microscopy of X-ray mapping of the sample with structure of substrate/W 4nm/$Fe_{40}Co_{40}B_{20}$ 5nm/Ta 1nm. (b-c) AFM images of (b) 4nm W and (c)20 nmW. Compared to the β-W, α-W has a smoother surface with larger gain size.

would be generated in Ta film when the charge current is flowing through all the layers. AFM images indicate that the grain size of β-W is larger than that of α-W (See Figure 3-2 b-c), and the surface RMS roughness for β-W and α-W is 2.12nm and

0.95nm respectively, much larger than the surface roughness of Si wafer, which is about 0.3nm. As a result, the film may become discontinuous when either W or FeCoB goes thinner. Our device measurement confirms that resistance of the device goes up sharply and the ST-FMR signal goes away when the W is below 2nm or FeCoB is thinner than 1.2nm.

In order to improve the surface roughness, RCA clean is recommended before the thin film deposition. Standard wafer clean process in the CNF can remove the organic and ionic contaminants on the SiO_x surface, providing a smoother SiO_x and W interface.

3.2 Fabrication: Lift-off process

3.2.1 Micron-size pillar

My coworker John Read developed the MgO based MTJ thin film growing process, and the high TMR was confirmed by Current In Plane Tunneling (CIPT) measurement at the National Institute of Standards and Technology [4] in Gaithersburg, MD. However, when we needed to explore the effect of various thin film structures on the MTJ properties, a quick and reliable way was needed locally at Cornell to characterize the TMR and RA-product of MTJ devices. Based on the recipe of a previous group member [5], I worked with my lab-mates to develop the three mask lift-off process for micron-pillar MTJ devices. For details of the 3-mask photolithography for MTJ fabrication, please refer to [1]. Here I want to point out that the second step is the crucial one. During the ion milling, I usually stop the etching in

the middle of the MgO layer to avoid any possible side-wall re-deposition. After that, a second low angle (15 degree away from the surface) ion milling is followed to further clean the side-wall. Then I keep our samples in a dry condition and deposit the 120nm thermal evaporated SiO_2 as soon as possible. With this recipe, it is possible for us to check the TMR and RA-product within three days of the thin film growth and it also provides us with a lot of micron-size devices for measurement.

I observed some interesting results in these micron-size devices. For example, I discovered that the exchange-bias of the reference layer can be modified by a current pulse in the presence of a small external field. Previous work has shown that the exchange-bias in both MTJs and spin valves can be degraded or reversed by electrical pulses [6-9], with the effect being attributed to heating or possibly to ST effects in the spin valve case. I have studied exchange-bias modification due to individual electrical pulses in the presence of a small external field (<50Oe) in FeCoB/MgO/FeCoB/IrMn MTJs as a function of MgO thickness (see Figure 3-4). For MgO thickness = 1.7 nm, RA = 5 x $10^3 \Omega\mu m^2$, pulses with J_c = 4 x $10^4 A/cm^2$ and V = 1.8 V, can repeatedly and reliably reverse the exchange-bias (results are shown in Figure 3-5). For 1.3 nm barriers, RA =150$\Omega\mu m^2$**,** much higher power pulses, J_c = 6 x $10^5 A/cm^2$ and V = 0.9 V, are required for reversal. The critical current slightly depends on the current direction (See Figure 3-5 (b)). Such results indicate that a combination of heating and ST, with the latter possibly involving the field-like spin torque component at high bias, is responsible for exchange-bias reversal in our MTJs.

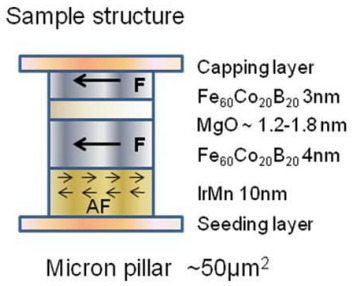

Figure 3-4. Layer structure of the device for exchange-bias modification study.

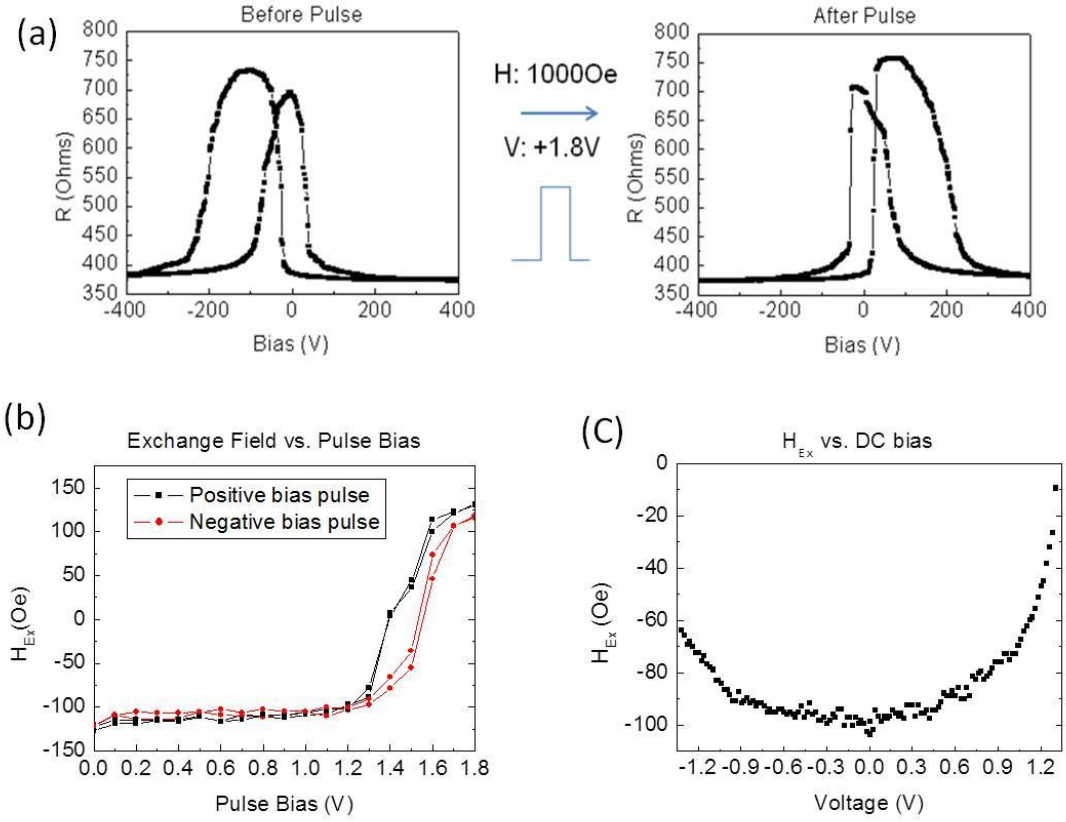

Figure 3-5. Data for the electrical pulse reversal of the exchange-bias experiment (a) Electrical pulse reversal of the exchange-bias with external field. (b-c) Exchange-bias field as a function of (b) pulse bias and (c) DC voltage. Asymmetry of the curve in terms of the bias direction indicates the effect of the in-plane spin transfer torque on exchange bias.

3.2.2 Nano-size pillar fabrication

In order to obtain a single-domain in the magnetic layer as well as to push the limit of the device size for potential high density ST-MRAM application, nano-size fabrication is desired for the spin-torque current. The traditional way of fabricating such junctions at Cornell, the carbon-based nanomask process, requires experienced CNF users one month or longer to complete the process, which hinders us when we are trying diverse structures. Considering that it requires relatively short time (about 3 days) to finish micron size device fabrication by life-off process, is it possible to apply the similar procedure in the nano-pillar fabrication? Liu in my group pointed out that using omni-coat/HSQ/PMMA as e-beam resist could make the lift-off process achievable. However, the pillar size of junctions fabricated with this omni-coat process was still too large to enable the magnetization of magnetic thin films to behave as a single-domain magnetic particle. Tseng and I decided to work on this recipe to push the pillar size to its minimum. So far we have found that devices with 75nm x 150nm size can be achieved in less than one week with almost 100% yield. Figure 3-6 shows the array we designed for this life-off process. The details of this fabrication technique can be found in the Ref [1]. The samples I measured in the following chapters were patterned by this omni-coat lift-off process.

3.3 Annealing treatment

3.3.1 Annealing condition for the FeCoB with in-plane anisotropy

Annealing MgO-based MTJs is essential to crystallize FeCo and achieve high TMR. The samples I measured in the next chapter were annealed at 350℃ for 1h under an easy-axis magnetic field of 0.2T in vacuum to enhance the TMR, following the traditional annealing recipe in our group. However, Hsin-wei and I have also annealed numerous samples in air with an AlN-based ceramic heater under external field. High and reliable TMR (>100%) is also achieved on those samples with annealing temperature at 350℃ and with annealing times as short as 1minute. As long as the device was capped by Ru, there is no evidence of oxidation of the top contact. We prefer this air annealing process since it saves us a lot of the time and enables us to try diverse annealing conditions, such as different annealing temperatures or external field directions. The H-R loop results indicate that the magnetic properties of our samples, especially those with IrMn pinned, are sensitive to the external field during the annealing. It affects the exchange bias of our devices as well as in-plane crystalline anisotropy.

3.3.2 Annealing conditions for the FeCoB with perpendicular anisotropy

Previous studies [10-12] show that interfacial perpendicular anisotropy can be obtained between the ferromagnetic electrodes and the tunnel barrier of the MTJ by employing the material combination of CoFeB–MgO when the CoFeB is thin enough. We have tested samples with the stack structure as Ta/ FeCoB/ MgO/Ta and W/FeCoB/MgO/Ta with of the FeCoB having a wedge structure across the wafer varying from 0.7nm to 2nm. All the samples are annealed in vacuum (pressure < 10^{-7} Torr) without an external field for 1 hour. To get a strong perpendicular anisotropy,

we found that the best annealing temperature is 200 ℃ (this is the displayed temperature in the Lindberg vacuum tube furnace and the real temperature on the wafer during the heating may be higher) for a Ta/FeCoB/ MgO/Ta stack structure, and 350 ℃ for W/FeCoB/MgO/Ta in our system. Figure 3-7 shows the perpendicular magnetization of a W/FeCoB/MgO/Ta sample with or without annealing treatment.

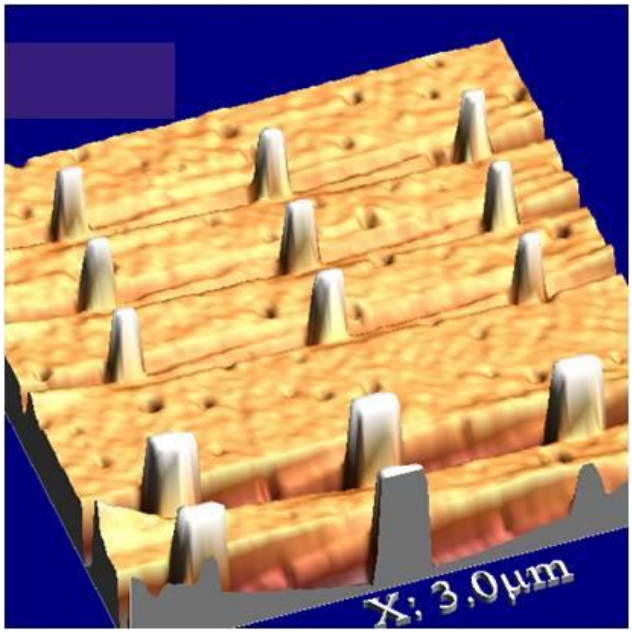

Figure 3-6. An AFM image of nano-size pillar array designed for lift-off process. The image was taken after the ion mill etching but before the SiOx deposition.

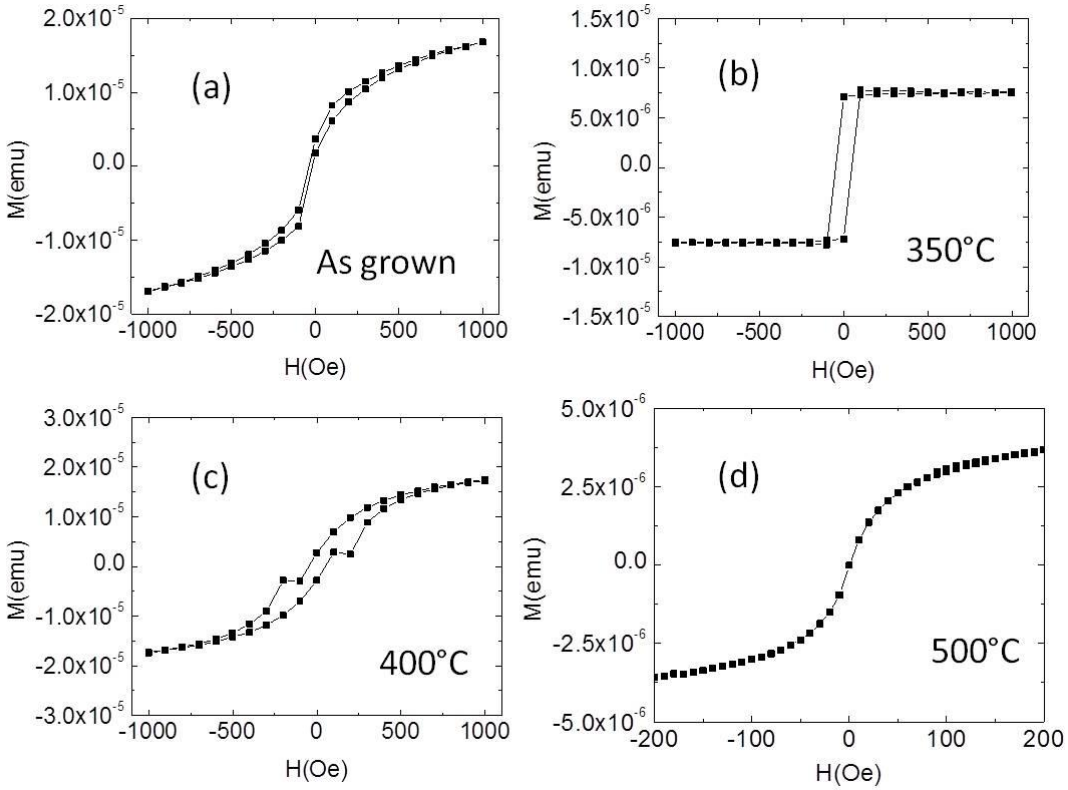

Figure 3-7. Out-of-plane magnetization curves for W20nm/FeCoB 1.5nm/MgO 2nm/ Ta 1nm annealed at different temperature.

3.4 Measurement setup

3.4.1 Measurement setup for MTJs

The basic measurement setup is shown in the Figure 3-8. Each device has four symmetric top contacts and four bottom contacts, so both 2 wire and 4 wire measurements can be applied. When the contact resistance is negligible compared to that of the tunneling junction, these two measurements give the similar results. The external in-plane magnetic field is applied by GNW 5403 C-frame magnet probe

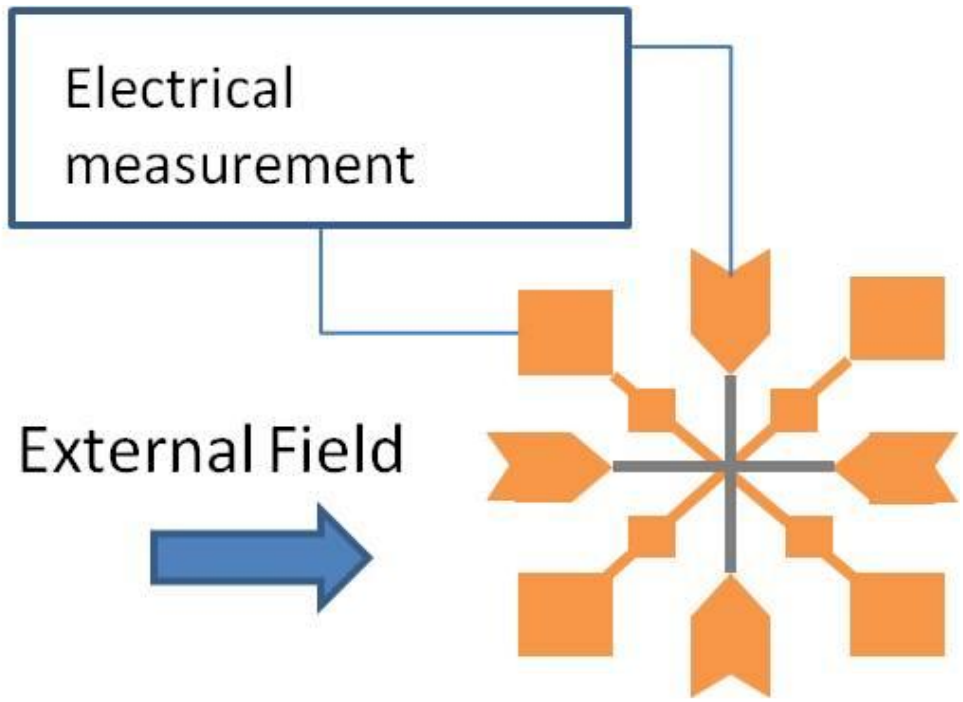

Figure 3-8. Measurement setup of MTJs.

system in CNS, which can provide field up to 0.2T. Electrical circuits are designed for different measurement purposes as following.

3.4.1.1 Field and current switching

The MTJs can be switched by external magnetic field or DC current. For the field switching measurement, I swept the external field while applying a small DC current (in the μA range) to detect the resistance of our device using the Keithley 2600 multi-meter. Figure 3-9 (a) and (b) show a typical major H-R loop withmulti-domain field switching for a micron size device and the minor loop of the single domain field switching for a nano size device respectively. From the above plots,

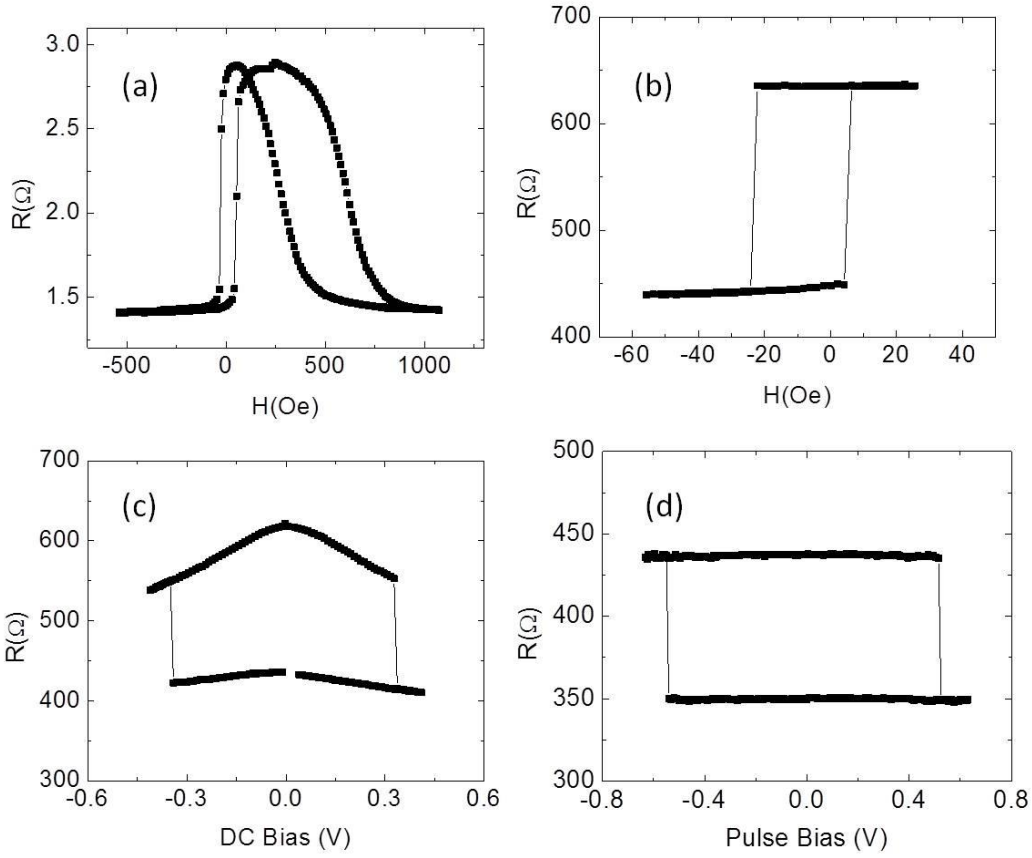

Figure 3-9. Field and current switching on MTJs (a-b) Field resistant loops for (a) a micron size MTJ device and (b) a single domain device ; (c-d) Current switching data for (c) a DC bias or (d) a pulse bias (200us pulse). The bias of dependent of resistant before switching confirms the property of a tunnel barrier.

the coercivity H_c and exchange-bias can be determined. For the current switching, a fixed external field is applied, and then a DC or pulse voltage is stepped to exert a spin transfer torque on the free magnetic layer. When the torque is strong enough, the state of resistance will be switched from AP to P or P to AP depending on the original state and current direction. The current switching plots are shown in Figure 3-9 (c-d).

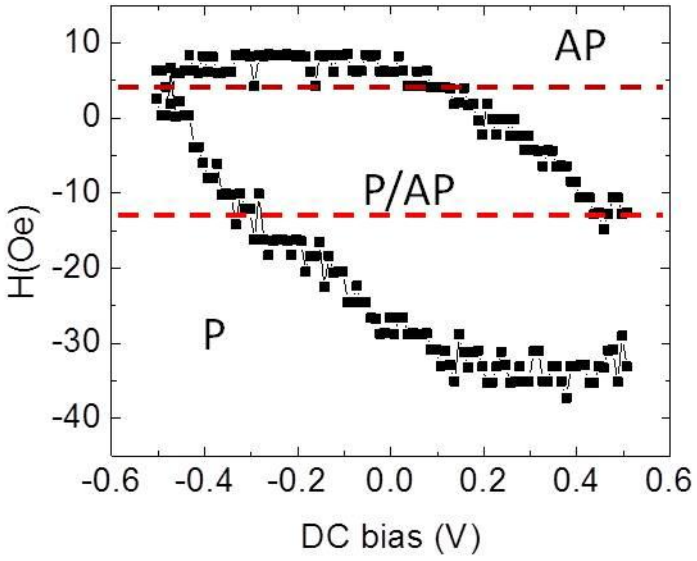

Figure 3-10. Switching phase diagram of a FeCoB/MgO/FeCoB MTJs. The regime between two dot lines is the area in which the MTJ is capable of performing bipolar switching.

3.4.1.2 Switching Phase Diagram Measurement

To investigate the spin torque switching properties and calculate the spin transfer torque vectors, obtained the switching phase diagram as plotted in Fig. 3-10, where the H_c is measured as a function of DC bias. The curves divide the diagram into mainly three parts: a region where the P state is stable, a region wherer the AP state is stable, and a region where either the P or AP state can be obtained depending on the original state, all as shown in the Figure 3-10. The two dotted lines in the SPD represent the region (between the lines) in which the a DC bias applied to the MTJ is capable of effecting bipolar switching.

The switching phase diagram provides an intuitive picture of the spin transfer torque: qualitatively the location of the points of intersection of the curves are determined by the STT. A larger in-plane torque will cause the boundary curves to cross at a lower voltage and a stronger field like torque will make the curves bend towards the negative field direction since the field like torque, or the interlayer exchange coupling, generally acts to promote the antiparallel alignment of the magnetic moments of the ferromagnetic electrodes of the MTJs [13].

To determine the bias dependence of the in-plane and the field-like torques, I used the thermal activation model [14-15]:

$$t^{\pm} = f_0^{-1} \exp\left(\frac{E_B^{\pm}(1 \mp V/|V_c^{\pm}|)}{k_B T^*}\right) \tag{3-1}$$

$$E_B^{\pm} = E_B^{0}(1 \pm (H_{eff} + b_J)/H_c^{0K})^{3/2} \tag{3-2}$$

Where the upper (lower) signs apply to AP-to-P (P to AP) switching, $t^{\pm}$ is the relaxation time, f_0 is the attempt frequency (which I assume to be $10^9 s^{-1}$), k_B is the Boltzmann constant, T^* is the junction temperature considering the bias-induced heating (here I assumed $T^* = T\sqrt{1+\alpha V^2}$) and $V_c^{\pm}$ is the critical voltage for magnetization switching at $T^* = 0K$. H_{eff} is the effective field and here I assumed it is equal to external field minus dipole field. H_c^{0K} is the coercive field at $T^* = 0K$, and b_J is the bias-induced field-like effect and here use the lowest-order expansion $b_J = C_1 V + C_2 V^2$ to capture the main effects. On the assumption that the in plane

torque linearly varies with V: $a_J^{\pm} = aV \propto V / V_C^{\pm}$, both bias dependence of in plane and field like torque can be determined.

3.4.1.3 ST-FMR measurement

The transfer of spin angular momentum from a spin-polarized current to a ferromagnet can generate sufficient torque to reorient the magnet's moment. The dynamics of the free magnetic layer near the resonance peak can be described by a simple macrospin approximation, so that Landua-Lifshitz-Gilbert (LLG) equation applies [16]

$$\frac{d\hat{m}}{dt} = -\gamma \hat{m} \times \vec{H}_{eff} + \alpha \hat{m} \times \frac{d\hat{m}}{dt} + \gamma \frac{\tau_{//}(V,\theta)}{M_s Vol} \hat{m} \times \frac{\hat{m} \times \hat{M}}{\left|\hat{m} \times \hat{M}\right|} + \gamma \frac{\tau_{\perp}(V,\theta)}{M_s Vol} \frac{\hat{m} \times \hat{M}}{\left|\hat{m} \times \hat{M}\right|} \qquad (3\text{-}3)$$

Here γ is the magnitude of the gyromagnetic ratio, α is the Gilbert damping parameter, $\vec{H}_{eff}$ is an effective field. $M_s Vol$ is the total magnetic moment of the free layer on the basis of the sample geometry Vol and the saturation magnetization of the ferromagnetic layer M_s. $\hat{m}$ and $\hat{M}$ are the moment directions of the free layer and fixed layer respectively.

To quantitatively measure the in-plane and field-like torques, ST-FMR measurement is utilized. FMR arises from the precessional motion of the magnetization of a ferromagnetic material in an external magnetic field *H*. The

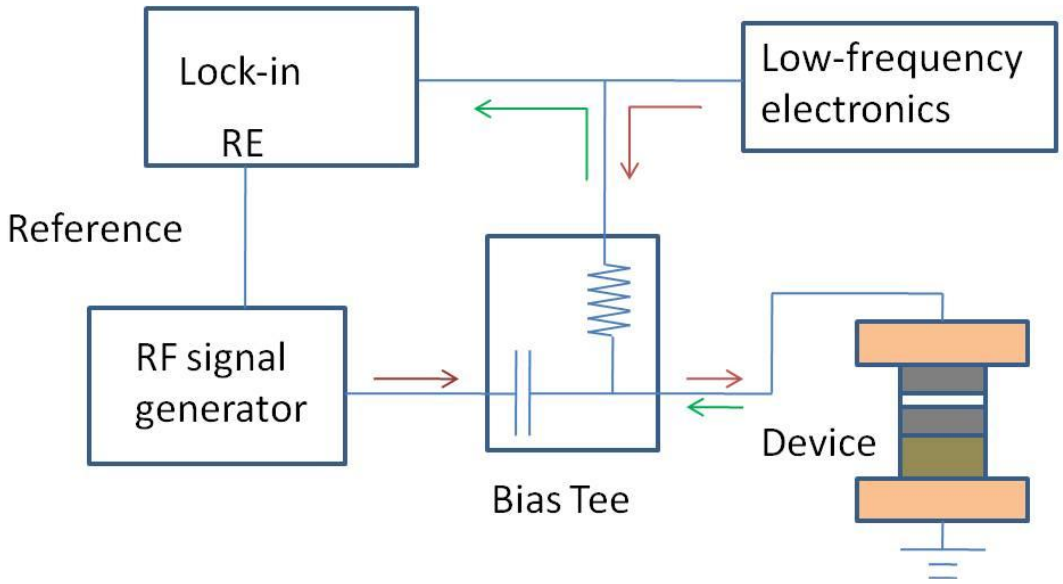

Figure 3-11. Schematic circuit for the ST-FMR measurement.

magnetic field exerts a torque on the sample magnetization which causes the magnetic moments in the sample to precess. The precession frequency of the magnetization depends on the orientation of the material, the strength of the magnetic field, as well as the macroscopic magnetization of the sample. The basic setup is shown in the Figure 3-11.

The ST-FMR measurements for the MTJs are made by first applying a sufficiently strong magnetic field H along the 90° direction to the easy axis, while the fixed $\hat{M}$ is also rotated to some degree due to the applied H. For example, in my case, the true angle between the magnetizations of the free layer and fixed layer is around 70 degree (See Figure 3-12(a)), as determined by a separate angle dependent resistant measurement. After that, a microwave-frequency current I_{RF} is applied and the frequency in 3.5GHz to 10GHz regime is swept. The spin-transfer torque from I_{RF}

excites resonant magnetic dynamics, which causes the resistance to oscillate at the driving frequency. The resonant DC voltage response, V_{mix}, is measured. To maximize the signal-to-noise ratio of the measurement, I chop I_{RF} at 1000 Hz and measure V_{mix} using a lock-in amplifier. It has been verified that that RF current is small enough that the FMR response is in the linear regime. The background are substrated to flatten the frequency dependence of the RF power reaching the sample.

The predicted ST-FMR signal is to a good approximation as following [17]

$$<V_{mix}>=\frac{1}{4}\frac{\partial^2 V}{\partial I^2}I_{RF}^2+\frac{1}{2}\frac{\partial^2 V}{\partial\theta\partial I}\frac{\hbar\gamma\sin\theta}{4eM_s Vol\sigma}I_{RF}^2(\zeta_{//}S(\omega)-\zeta_{\perp}\Omega_{\perp}A(\omega)) \qquad (3\text{-}4)$$

Here $\zeta_{//}=[(2e/\hbar)/\sin\theta]d\tau_{//}/dI$ is the differential in plane torque and $\zeta_{\perp}=[(2e/\hbar)/\sin\theta]d\tau_{\perp}/dI$ is the differential field like torque in dimensionless units. $S(\omega)=1/\{1+[(\omega-\omega_m)/\sigma]^2\}$ and $A(\omega)=[(\omega-\omega_m)/\sigma]S(\omega)$ are symmetric and antisymmetric lorentzians functions , σ is the linewidth, ω_m is the resonant precession frequency, and $\Omega_{\perp}=\gamma(4\pi M_{eff}+H)/\omega_m$.

The ST-FMR spectra under different DC bias are shown in the Figure 3-12 (b-d). From the plots, we can see that the degree of asymmetry in the ST-FMR peak shape versus frequency depends strongly on DC bias V with peak shapes for V = 0 being symmetric, and the sign of the asymmetry depending on the direction of current, indicating that the field-like torque is governed by the DC bias.

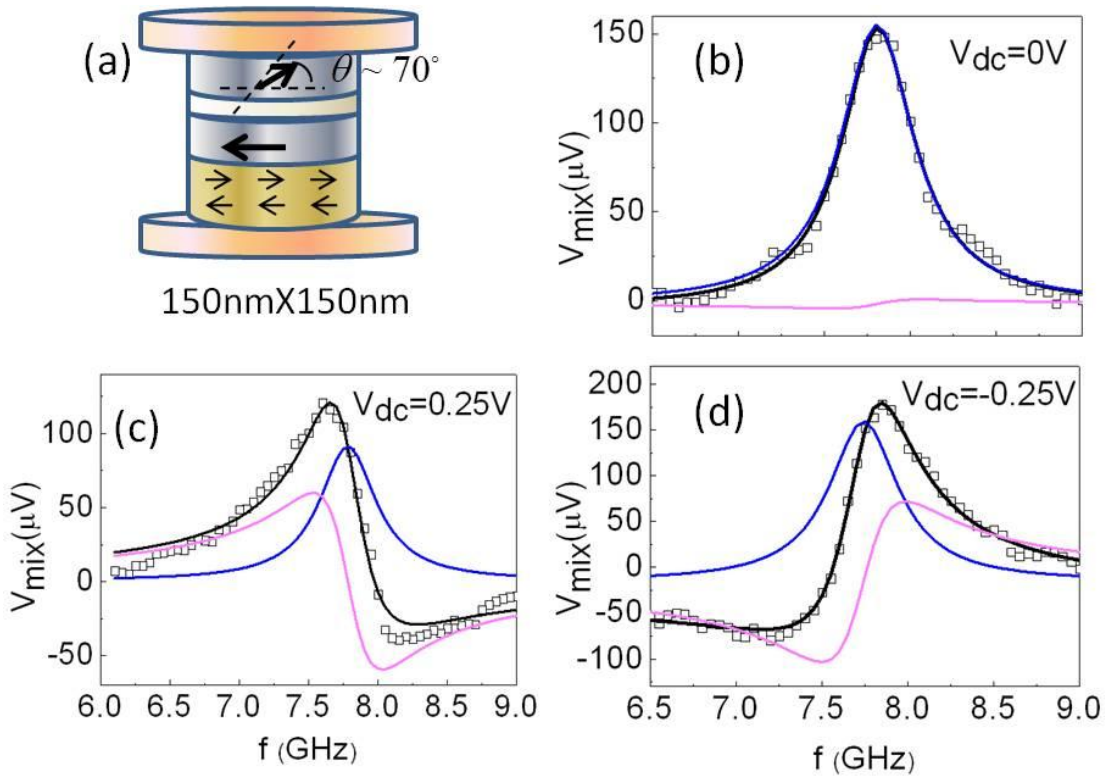

Figure 3-12. ST-FMR measurement (a) Schematic of sample layer structure. The angle between the magnetizations of the free layer and fixed layer is 70 degree during the measurement. (b-d) FMR spectra at room temperature. Spin-transfer FMR spectra at H =500 Oe for different DC biases. Symbols are data; lines are lorentzian fits or its symmetric and anti- symmetric lorentzians components. The frequency-dependent backgrounds for non-zero d.c. biases have been removed by fits.

When the oscillating current frequency ω and the magnitude of the applied external magnetic field H_0 satisfy the ferromagnetic resonance condition (peak location), the Kittel formula applies

$$\omega = \gamma / 2\pi [H_0 (H_0 + 4\pi M_{eff})]^{1/2} \tag{3-5}$$

where $4\pi M_{eff}$ is the effective demagnetization field of the free layer.

3.4.2 ST-FMR measurement in the spin Hall effect

In spin Hall effect measurement, the frequency of the RF power was fixed and then a sweeping magnetic field H_{ext} was applied in the film plane, with the angle between H_{ext} and micro- strip (charge current direction) kept at $45°$. I studied ferromagnetic layer (FM)/ normal metal layer (NM) bi-layer films with a microwave-frequency charge current applied in the film plane. An oscillating transverse spin current is generated in the NM by the spin Hall effect and injected into the adjacent FM. The exerted oscillating spin torque on the FM induces magnetization precession, which leads to an oscillation of the bilayer resistance due to the anisotropic magnetoresistance of FM. Similar to the case in MTJs, a resonant DC voltage, V_{mix} can be recorded as a function of external field. The output power of the microwave signal generator was varied from 0 to 25 dBm and the measured dc voltage was proportional to the applied power, indicating that the induced precession was in the small angle regime. All the measurements I present in the Chapter 5 were performed at room temperature with a microwave power of 15 dBm.

The LLG equation is also applied in analyzing the ST-FMR measurements of the spin Hall effect. The third and fourth terms on the right-hand side of the equation are the results of in-plane spin torque and the out-of-plane torque, with the former due to the ST from spin Hall effect and the latter due to the Oersted field. The mixing

signal in response to a combination of the in-plane and out-of-plane torques has been calculated as following [18]

$$<V_{mix}>=-\frac{1}{4}\frac{\partial R}{\partial \theta}\frac{\gamma I_{rf}\cos\theta}{\Delta H 2\pi(d\omega/dH)\big|_{H_{ext}=H_0}}[SF_S(H_{ext})+AF_AH_{ext})] \quad (3\text{-}6)$$

where $F_S(H_{ext})=\Delta H^2/[\Delta H^2+(H_{ext}-H_0)^2]$ is a symmetric Lorentzian function centered at the resonant field H_0 with line-width ΔH, $F_A(H_{ext})=F_S(H_{ext})(H_{ext}-H_0)/\Delta H$ is an anti-symmetric Lorentzian. The amplitude of the symmetric Lorentzian peak $S=\hbar J_{S,rf}/(2e\mu_0 M_s t)$ is proportional to the spin current density $J_{S,rf}$ and the amplitude of the antisymmetric peak $A=H_{rf}[1+(4\pi M_{eff}/H_{ext})]^{1/2}$ is proportional to H_{rf}, which is the Oersted field generated by the rf current. Here μ_0 is the permeability in vacuum, I_{rf} is the rf current through the microstrip, ω is the resonance frequency and θ is the angle between H_{ext} and the charge current direction.

The ratio of the spin current density to the charge current density is defined as the spin Hall angle as following:

$$\theta_{SH}=\frac{J_{S,rf}}{J_{C,rf}}=\frac{S}{A}\frac{e\mu_0 M_S td}{\hbar}[1+(4\pi M_{eff}/H_{ext})]^{1/2} \quad (3\text{-}7)$$

Here *t* and *d* is the thickness of FM and NM layer respectively. Furthermore, the damping coefficient can be measured by

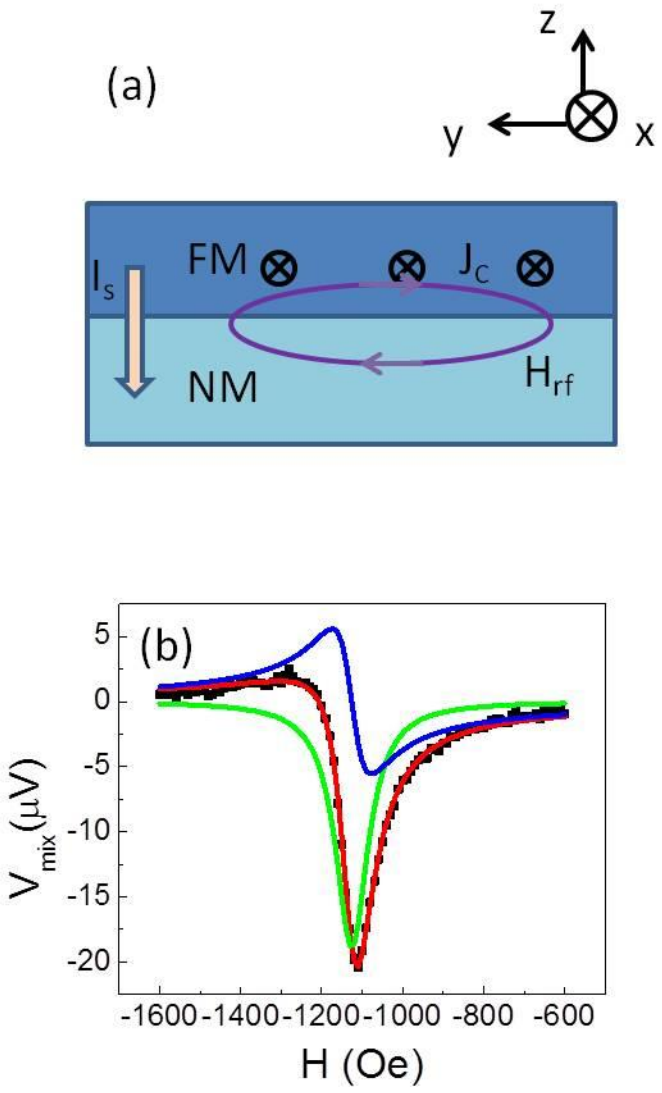

Figure 3-13 The spin Hall effect measurement: (a) Schematic of a bilayer thin film system illustrating the spin Hall effect. FM represents the ferromagnetic layer and NM stands for the normal metal, which is the spin Hall material here. (b) FMR spectra measured for the Py/W bilayer samples with fits (red line) and its symmetric lorentzians component (green line) and anti-symmetric lorentzians component (blue line).

$$\Delta H = \Delta H_0 + \frac{2\pi\omega}{\gamma}\alpha \tag{3-8}$$

Where ΔH_0 is the intrinsic line-width.

Thus with ST-FMR spectra, the spin transfer torque as well as the properties of ferromagnetic layer can be investigated.

3.5 Conclusion

In conclusion, in this chapter, I have presented the deposition conditions for MgO based MTJs as well as W based spin Hall bi-layer structures. I discussed micron-size and nano-size fabrication processes by the lift-off method, and considered the related major issues or problems associated with these fabrication processes. After that, I presented typical results for the field or current induced magnetic switching and discussed the resultant switching phase diagram. Finally, I introduced the theory and measurement setup for the ST-FMR study, which is the main method I used in the following chapters to measure the spin transfer torque.

BIBLIOGRAPHY

1. Tseng H. SPIN-TORQUE EFFECTS IN MGO-BASED MAGNETIC TUNNEL JUNCTIONS, Ph. D Thesis (2013).

2. Stewart D. A. New type of magnetic tunnel junction based on spin filtering through a reduced symmetry oxide: FeCo|Mg3B2O6|FeCo. *Nano letters* 10, 263(2010**)**.

3. Pai, C.-F., Liu, L., Li, Y., Tseng, H. W., Ralph, D. C., & Buhrman, R. a. Spin transfer torque devices utilizing the giant spin Hall effect of tungsten. *Applied Physics Letters*, 101, 122404 (2012).

4. J.C. Read MAGNESIUM BORON OXIDE TUNNEL BARRIERS, Ph. D Thesis (2009).

5. G. D. Fuchs. SPIN-TRANSFER EFFECTS IN NANOSCALE MAGNETIC TUNNEL JUNCTIONS AND SPIN VALVES, Ph. D Thesis (2007).

6. Wei, Z., Sharma, a., Nunez, a., Haney, P., Duine, R., Bass, J., MacDonald, a., et al. Changing Exchange Bias in Spin Valves with an Electric Current. *Physical Review Letters*, 98, 116603(2007).

7. Prejbeanu, I. L., Kerekes, M., Sousa, R. C., Sibuet, H., Redon, O., Dieny, B., & Nozi ères, J. P. Thermally assisted MRAM. *Journal of Physics: Condensed Matter*, 19 165218 (2007).

8. Papusoi, C., Sousa, R., Herault, J., Prejbeanu, I. L., & Dieny, B. Probing fast heating in magnetic tunnel junction structures with exchange bias. *New Journal of Physics*, 10, 103006(2008).

9. Papusoi, C., Sousa, R., Herault, J., Prejbeanu, I. L., & Dieny, B. Probing fast heating in magnetic tunnel junction structures with exchange bias. *New Journal of Physics*, 10, 103006(2008).

10. Ohldag, H., Scholl, a., Nolting, F., Arenholz, E., Maat, S., Young, a., Carey, M., et al. Correlation between Exchange Bias and Pinned Interfacial Spins. *Physical Review Letters*, 91, 017203 (2003).

11. Ikeda, S., Miura, K., Yamamoto, H., Mizunuma, K., Gan, H. D., Endo, M., Kanai, S., et al. A perpendicular-anisotropy CoFeB-MgO magnetic tunnel junction. *Nature materials*, 9, 721 (2010).

12. Meng, H., Sbiaa, R., Wang, C. C., Lua, S. Y. H., & Akhtar, M. a. K. Annealing temperature window for tunneling magnetoresistance and spin torque switching in CoFeB/MgO/CoFeB perpendicular magnetic tunnel junctions. *Journal of Applied Physics*,110, 103915 (2011).

13. Katayama, T., Yuasa, S., Velev, J., Zhuravlev, M. Y., Jaswal, S. S., & Tsymbal, E. Y. Interlayer exchange coupling in Fe/MgO/Fe magnetic tunnel junctions. *Applied Physics Letters*, 89,112503 (2006).

14. Oh, S.-C., Park, S.-Y., Manchon, A., Chshiev, M., Han, J.-H., Lee, H.-W., Lee, J.-E., et al. Bias-voltage dependence of perpendicular spin-transfer torque in asymmetric MgO-based magnetic tunnel junctions. *Nature Physics*, 5, 898 (2009).

15. Li, Z., & Zhang, S. Thermally assisted magnetization reversal in the presence of a spin-transfer torque. *Physical Review B*, 69,134416 (2004).

16. Kovalev, A., Bauer, G., & Brataas, A. Current-driven ferromagnetic resonance, mechanical torques, and rotary motion in magnetic nanostructures. *Physical Review B*, **75**, 014430 (2007).

17. Sankey, J. C., Cui, Y.-T., Sun, J. Z., Slonczewski, J. C., Buhrman, R. a., & Ralph, D. C. Measurement of the spin-transfer-torque vector in magnetic tunnel junctions. *Nature Physics*, 4, 67 (2008).

18. Liu, L., Moriyama, T., Ralph, D., & Buhrman, R. Spin-Torque Ferromagnetic Resonance Induced by the Spin Hall Effect. *Physical Review Letters*, 106, 036601 (2011).

CHAPTER 4

EFFECTS OF INTERFACIAL ELECTRONIC STRUCTURE ON IN-PLANE SPIN TRANSFER TORQUE IN MGO-BASED MTJS

In this chapter, I report the study of MgO-based MTJs with symmetric electrodes FeCoB in both the as-grown and annealed (350 ℃) state. The spin torque ferromagnetic resonance measurements (ST-FMR) indicate that the asymmetry of the bias dependence of the in-plane torque is due to changes of the MTJs that occur in the annealing process. Analysis of the adjusted torkance, which is sensitive to non-ideal tunneling mechanisms and effects of interfacial electronic structure, indicates that the annealing reduces the inelastic tunneling component of the junction conductance, and creates or enhances a peak at about 0.15V above the Fermi level in the density of states of the minority band of one or both of the electrodes. This peak location is essentially the same as the peak of the minority band states that has previously observed on the surface of bcc (100) Fe. Thus I conclude that the most likely source of the asymmetry of the bias dependent torkance is due to Fe minority band states that are localized at the electrode – tunnel barrier interface.

4.1 Background

4.1.1 Background: Asymmetric bias dependence of in-plane torque

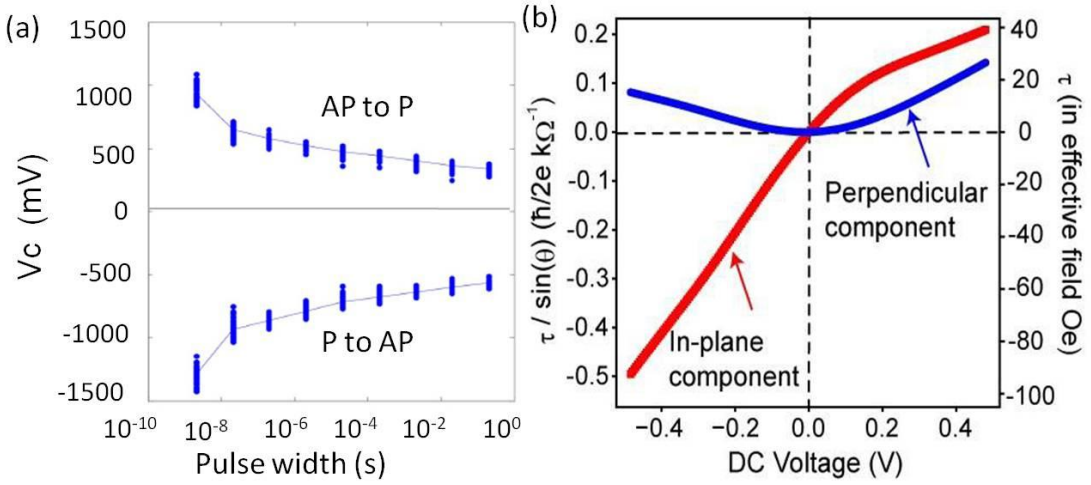

Figure 4.1 Asymmetric switching current. (a) Switching voltage versus current pulse-width. (Figure from Ref. 2); (b) Bias dependence of In-plane and perpendicular components of the spin-transfer torque (Figure from Ref.7).

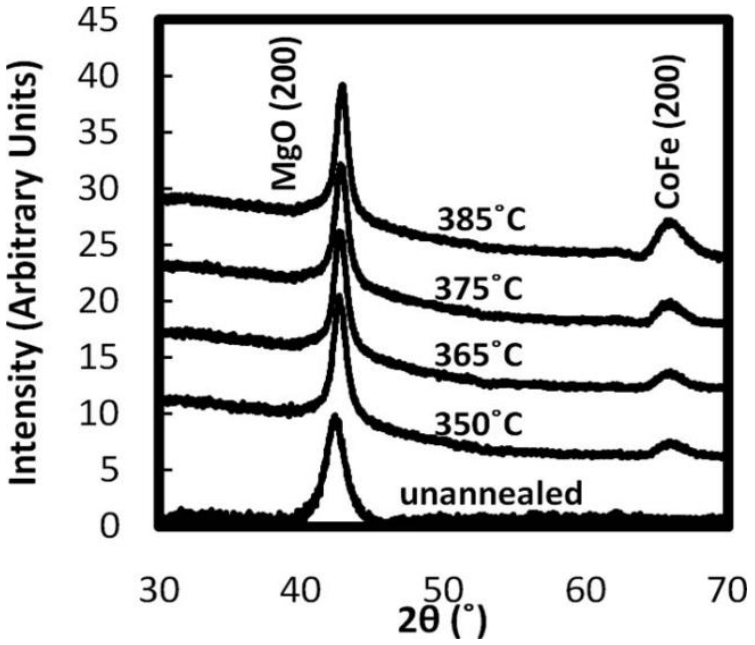

Figure 4-2: Relative XRD intensities as a function of 2θ is plotted with the anneal temperature as a parameter, showing the MgO (200) and the CoFe (200) peak (Figure from Ref.10).

Spin-transfer induced magnetization switching in MgO-based MTJs, typically in FeCoB/MgO/FeCoB systems, has been extensively studied for its potential applications in spintronics devices [1-3]. It was found that the switching voltage response is asymmetric going from the high resistance state to the low resistance state and vice versa [2]. It requires larger voltage to switch from P to AP state than AP to P (see Figure 4-1(a)), resulting in much larger switching current from P to AP than the other, considering that the resistance in P state is smaller than that in AP state. This must be considered to optimize the read-write margin for a 1T1R (single transistor, single MTJ) memory device design, since it requires the transistor to supply asymmetric driving current. This asymmetry can be attributed to the asymmetric bias dependence of the in-plane torque, which has been observed experimentally by several groups in magnetic tunnel junctions (MTJs) with symmetric electrodes [4-7]. Their results (e.g., see Figure 4-1(b)) show that the in-plane torque component is stronger in one bias direction than the other. Several explanations have been proposed, including asymmetric interfaces that can occur even with identical electrodes due to fabrication effects, impurity-mediated transport through the barrier, and bias dependent inelastic scattering effects [8-10]. I will discuss those mechanisms later in this chapter.

4.1.2 Effects of annealing in MTJs

Thermal annealing is essential for enhancing the TMR in MgO based MTJs [8-14]. XRD data (Figure 4-2) confirm that the amorphous CoFeB crystallizes in the (200) orientation after heat treatment, which is correlated with the diffusion of B from

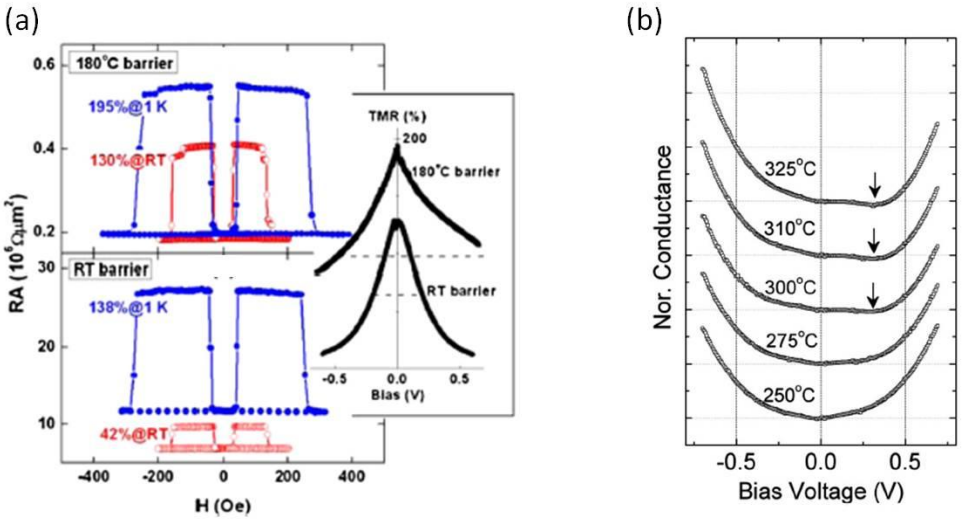

Figure 4-3. Annealing effects on TMR and conductance: (a) Comparison of the magnetoresistance loops at RT and 1 K for MTJs of the same 2.5 nm MgO barrier thickness but deposited at 180 ℃ and RT, Inset shows the corresponding TMR bias dependence at 1 K (From Ref. 8); (b) Normalized conductance in terms of the applied bias voltage for various thermal annealing temperatures (From Ref. 9).

ferromagnetic layers into the tunnel barrier [11]. Meanwhile, it is also found that the annealing not only dramatically enhances TMR, but also breaks the symmetry of bias dependent TMR [8] and differential conductance [9]. Figure 4-3 (a) demonstrates that the bias dependence of TMR becomes asymmetric with the thermal treatment on the tunnel barrier. The result from the conductance measurement (Figure4-3 (b)) shows that the conductance in a positive bias was lower than that in a negative bias and has a local minimum near a bias voltage of 0.3 V. Those studies give a hint that crystallization of electrodes may affect the symmetry of tunneling. Although the effect of annealing has been extensively studied [8, 10-14], most research focuses on the

effect on material properties [10,11,13] or electronic transport properties [8]. Studies on current induced magnetic switching and spin transfer torque (STT), which are essential to device performance and fundamental spin physics of hot electrons in low resistance-area (RA) product MTJs, are relatively scarce. Such a study on the effects of the annealing on current induced switching and STT which I present here can provide more detailed information about the relationship between material property, fundamental science and device performance, helping us to explore the tunneling mechanism for this asymmetry.

4.2 Sample preparation

In the sections 4.2-4.5, MgO-based MTJs of the composition (thickness in nanometers) bottom contact/IrMn 8/$Fe_{20}Co_{60}B_{20}$ 2/MgO 1/$Fe_{20}Co_{60}B_{20}$ 1.5/ top contact (See Figure 4-4(a)) has been studied. The top CoFeB is patterned by e-beam lithography and ion beam etching technique to produce an elliptical or circle cross-section with a nominal size of 200x120nm^2 for current induced switching or 150x150nm^2 for ST-FMR measurement. The RA product for the parallel configuration in our as-grown MTJs (annealed) is about 16Ωμm^2 (20Ωμm^2). The etching is stopped at the MgO barrier and thus the bottom layer is largely unpatterned to minimize the stray field from the bottom ferromagnetic electrode. After the patterning process, some of the MTJs are measured directly while others cut from the same wafer are annealed at 350℃ for 1h under an easy-axis magnetic field of 0.2T in vacuum to enhance the TMR. Each measurement is carried out on more than three samples and show similar results, while the data presented in this letter are from just one sample. All

measurements are performed at room temperature and positive current corresponds to electron flow from the free to the pinned layer.

In section 4-7, I also discuss results from another type of CoFe-based MTJs whic were provided by Jordan A. Katine at HGST Inc. Those devices had the following layer structure: IrMn(6.1nm) / CoFe(1.8nm) / Ru / CoFeB(2.0nm) / MgO / CoFe(0.5nm) / CoFeB(3.4nm) and round nanopillar shapes with coercivity H_C is zero at RT. The overall ratio between Co and Fe in these samples was 1.5:1 with the RA of the MTJs about 15 $\Omega\mu m^2$.

4.3 Experimental results

4.3.1 Field and current switching

An easy axis hysteresis loop is shown in Figure 4-4(b). The annealing process enhances TMR from about 13% to 90%, indicating a 120% increase in the tunnel current polarization from ~25% to ~56%. The annealed (as-grown) sample can achieve bipolar current driven switching with bias pulse width $20ms$ in the external magnetic field $-35Oe$ ($-54Oe$) (Figure 4-4(c)). Bipolar current driven switching has been observed in the annealed (as-grown) sample with bias pulse width between $200\mu s$ to $1s$ region.

I fit these experimental results to a thermal activation model expressed as [15]

$$V_c(t) = V_{c0}(1 - \frac{k_B T}{E_B} \ln(t/\tau_0)) \qquad (4\text{-}1)$$

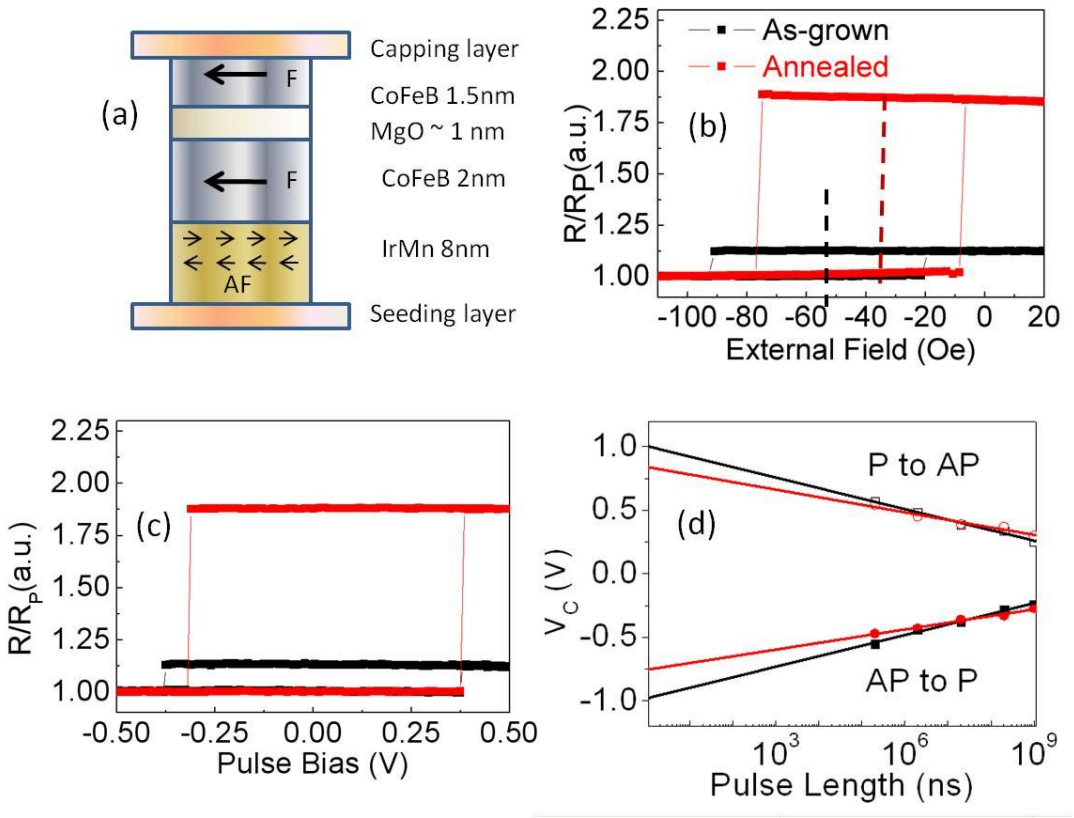

Figure 4-4. Field and current switching plots (a) MgO-based MTJ with the structure (thickness in nanometres) bottom contact/IrMn 8/$Co_{60}Fe_{20}B_{20}$ 2/MgO 1/$Co_{60}Fe_{20}B_{20}$ 1.5/ top contact; (b-d) Plots of the as-grown sample (black) and the annealed sample (red): (b) R/Rp versus external field, TMR is enhanced from about 13% to 90% after annealing (c) R/Rp versus bias. The bipolar current driven switching is achieved in the annealed (as-grown) sample with bias pulse width $20ms$ under the external magnetic field $-35Oe$ ($-54Oe$). (d) Critical switching current versus the pulse length bias at the long pulse range. Using a thermal activation model, the zero temperature critical voltage in that specific external field for annealed (as-grown) MTJ is $0.75V$ ($0.98V$) for AP to P switching and $0.84V$ ($1.0V$) for P to AP switching.

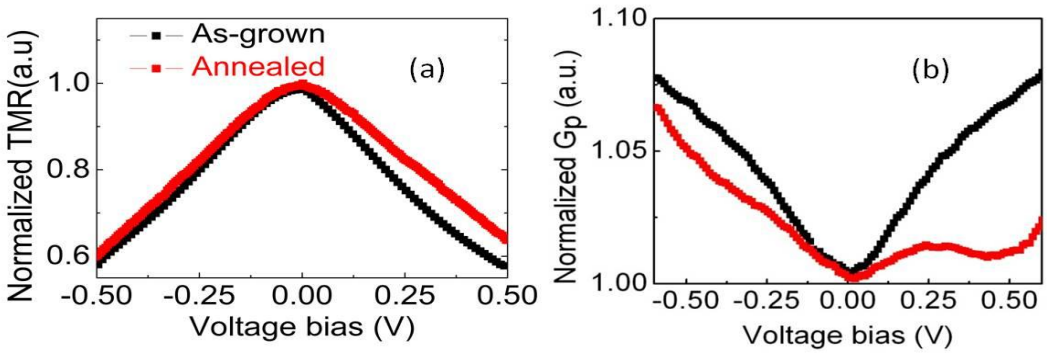

Figure 4-5. Plots of TMR and conductance of the as-grown sample (black) and the annealed sample (red): (a) Bias-voltage dependence of normalized TMR. (b) Bias-voltage dependence of normalized conductance (dI/dV) in parallel state.

Here, V_{C0}, k_B, T, E_B, and τ_0, respectively, denote the intrinsic switching voltage, Boltzmann's constant, temperature, energy barrier and attempt time. Data in this region can be fitted well (Figure 4-4 (d)), and I obtain that the zero temperature critical voltage for that specific external field for annealed (as-grown) MTJ is $0.75V$ ($0.98V$) for AP to P switching and $0.84V$ ($1.0V$) for P to AP switching. In the as-grown case, I applied the external field to cancel the H_{shift}. However, in the annealed case, in order to get roughly similar switching voltages for P to AP and AP to P, external field needs to be much closer to the P to AP boundary. Thus it can be expected that a larger current is needed for P to AP switching than AP to P switching without magnetic field assistance, and the switching voltage for P to AP has a larger chance to be above the breakdown voltage when the pulse width is shorter. This result clearly indicates that the symmetry of the critical current on bias direction can be adjusted by external field. However, ultimately those devices need to work in zero external field, and thus it is

important to reveal the mechanism for the asymmetry of current induced magnetic switching and optimize it by other methods. Another interesting result from this measurement is that although annealing can dramatically enhance TMR (~7 times) and spin polarization (~ twice), it will not reduce the critical voltage very much (~25%), which indicates that other factors extensively influence the magnitude of critical switching current.

4.3.2 Bias dependence of TMR and G_P

While the TMR as a function of bias is pretty symmetric in the as-grown sample, the bias dependence of TMR is stronger in the negative bias direction than the positive bias direction (Figure 4-5 (a)) in the annealed junction; also the curve of differential conductance in parallel condition (G_P) vs. voltage (Figure 4-5 (b)) has richer features: local minimums show up after annealing. The above results have been observed and discussed in the MTJs with a similar structure [16-18]. Here positive current corresponds to electron flow from the free to the pinned layer.

4.3.3 Switching phase diagram

To determine the bias dependence of the STT, I first plot the switching phase diagram, where the switching fields are measured as a function of DC bias (Figure 4-6. (a)-(b)). The boundary of switching phase diagram appears symmetric with the zero point of the coordinate for the as-grown sample, while this symmetry is markedly broken down after annealing. Considering that the cross point of the switching phase diagram boundary curves is directly determined by the in-plane spin transfer torque,

our results indicate that annealing enhances the asymmetry of the in plane torque in terms of bias direction. On the other hand, the field -like torque makes the curves bend toward to the negative field direction since interlayer exchange coupling prefers the AP configuration in MTJs with an ultrathin MgO barrier [19]. Therefore it can be concluded that annealing enhances the magnitude of the field-like torque at larger bias from our switching phase diagram plots for both bias directions.

Next, the thermal activation model [20,21] is applied to quantitatively calculate the voltage dependence of STT. The details of the model were discussed in Chapter 3. The best fit for the annealed (as-grown) sample is obtained with ($1.25V$), $V_c^+ = 1.56V$ ($1.35V$), $C_1 = 3.2\times10^{-3} Oe/V$ ($1.7Oe/V$) and $C_2 = 8.2Oe/V^2$ ($32Oe/V^2$) and those parameters fit the overall switching phase diagram reasonably well (Figure 4-6 (a-b)). On the assumption that the in-plane torque linearly varies with voltage: $a_J^{\pm} = aV \propto V / V_C^{\pm}$, the voltage dependence of the normalized in-plane torque (Figure 4-6(c)) and the field-like torque (Figure 4-6(d)) are plotted. Data are normalized by the maximum absolute number: absolute value of in plane torque at -0.6V in Figure (a) or value of the field-like torque at 0.6V in Figure (b) for the annealed sample). The plots show that annealing doubles or triples the in-plane torque on the AP to P switching direction but does not change the in-plane torque for P to AP switching very much at all; for the field-like torque, it is almost 4 times larger in the annealed sample.

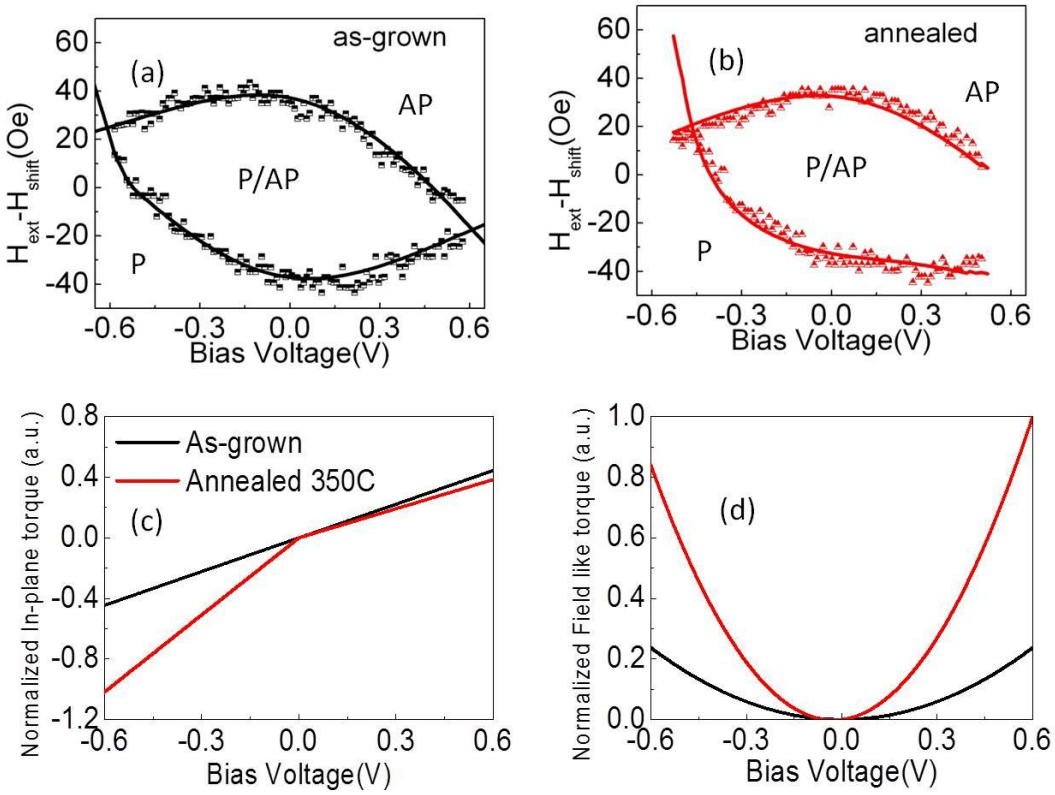

Figure 4-6. Switching phase diagram and fitting for STTs: (a-b) Switching phase diagram of (a) the as-grown junction and (b) the annealed junction. The lines are the best fits using the thermal activation model. P and AP labeled in the plots represent the regime where parallel (P) or anti-parallel (AP) configuration is stable, or the configuration can be either one, depending on the initial state (P/AP). (c) Normalized in-plane torque and (d) field-like torque as a function of the bias obtained from the best fit as a function of the voltage, assuming $\tau_{//+} = a_{+}V$, $\tau_{//-} = a_{-}V$ and $\tau_{\perp} = c_1 V + c_2 V^2$.

4.3.4 ST-FMR

In the switching phase diagram fitting, I assume that the in-plane torque is linearly dependent on the bias voltage, which is a first order approximation. To confirm the result from switching phase diagram measurement as well as get more detailed information, ST-FMR measurement [22,23] is performed in the MTJs with round shape ($H_c = 0$) and external field is applied on hard axis in plane. The results are shown in Fig 4-7(a-d). Due to the weaker signal, the as-grown sample can only be biased up to $\pm 0.25V$, while I could apply a DC voltage up to $\pm 0.4V$ to the annealed sample. I observed that the in-plane component of the spin transfer torkance (defined as the voltage derivative of the torque) has larger bias dependence in the annealed sample than that of the as-grown sample. It has two turning points around $+0.15V$ and $-0.15V$, with a negative slop between, significantly affecting the symmetry of the bias dependence of the in-plane torque. Moreover the appreciable field-like component of spin transfer torkance is observed in the annealed sample, which is 5 times larger than that of the as-grown sample at the $|V| = 0.25V$ points, resulting in bigger field like torque too. The above results are consistent with the conclusion from the switching phase measurement. This behavior of the bias dependent torques of the annealed samples agrees well with previous papers [6-7]. A similar behavior of the bias dependent spin transfer torques is also measured in devices with a different ferromagnetic electrode composition, $Fe_{20}Co_{60}B_{20}$. (See Figure 4-8).

In summary, I measured the field and current switching, bias dependence of differential conductance and TMR, switching phase diagram and ST-FMR. The results

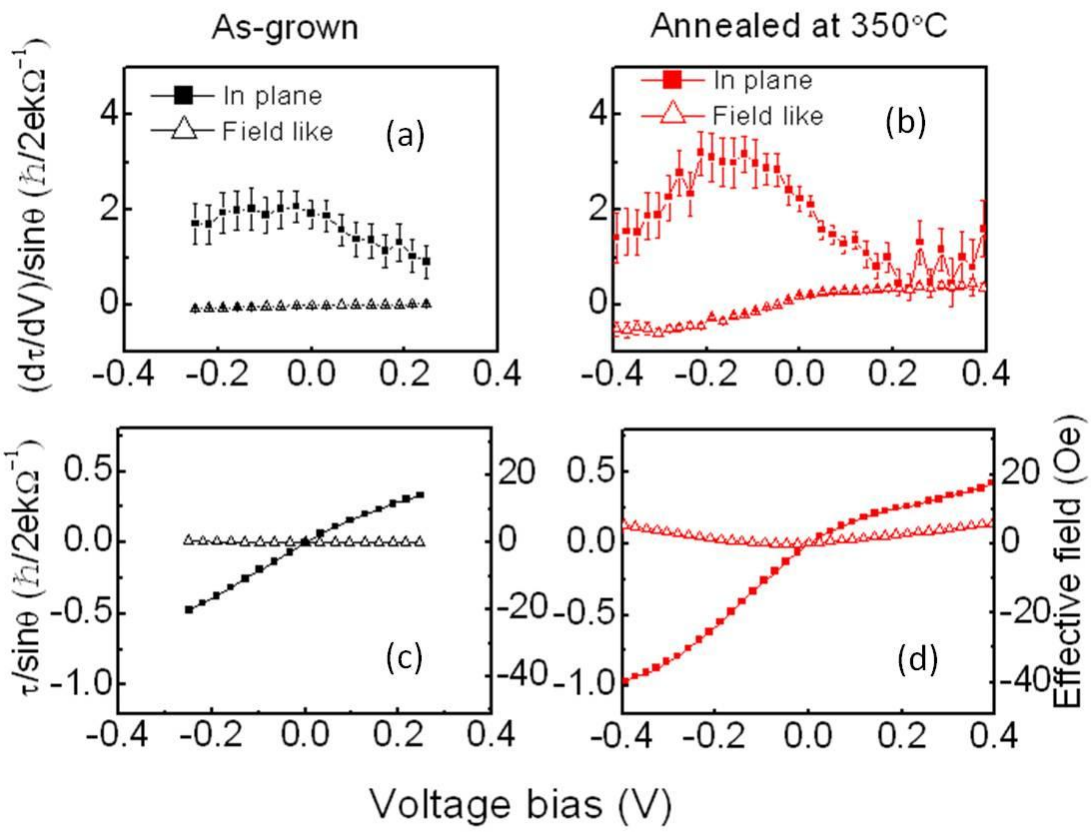

Figure 4-7. Bias dependence of spin transfer torkance and torque of a $Fe_{20}Co_{60}B_{20}$/MgO/$Fe_{20}Co_{60}B_{20}$ MTJ: (a-d) Spin transfer torkance and STT measured by ST-FMR: In-plane torkance and field-like torkance of (a) the as-grown sample and (b) the annealed sample. The in-plane torque and the field-like torque of (c) the as-grown sample and (d) the annealed sample. The data indicate more asymmetric in plane torque in terms of bias direction and stronger field like torque in the annealed device.

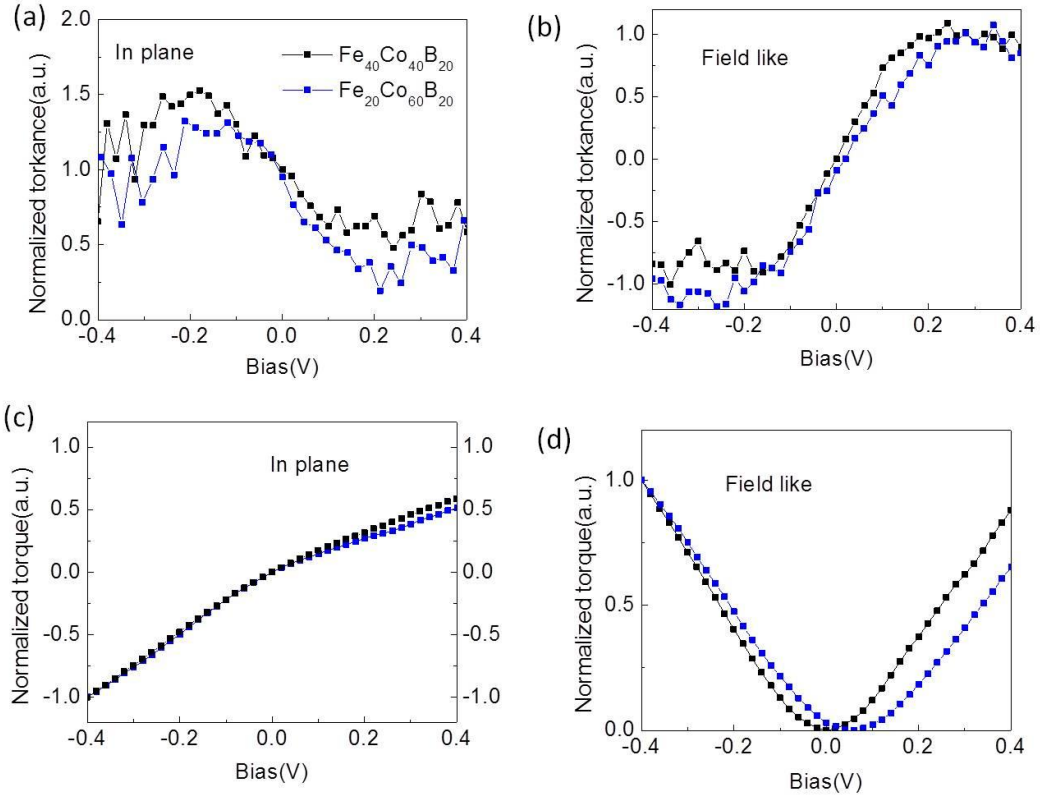

Figure 4-8. Normalized spin transfer torkance and STT measured by ST-FMR with $Fe_{20}Co_{60}B_{20}$ (black) or $Fe_{40}Co_{40}B_{20}$ (Blue) as electrodes: Bias dependent of (a) in-plane torkance, (b) field-like torkance, (c) in-plane torque and field-like torque. Similar asymmetric behavior of in plane torque in terms of bias direction is observed in both devices. In (a), the data was normalized by dividing the value at zero bias for the two devices respectively; in (b-d) the data was normalized by dividing the maximum absolute value for two devices respectively.

show that the asymmetric bias dependence of the in-plane spin transfer torque is induced during the annealing. Meanwhile, the symmetry of TMR and differential conductance is also broken. So the questions are whether the two phenomena are correlated and why annealing changes the symmetry.

4.4 Data Analysis

4.4.1 Bias dependent differential conductance and the in-plane torkance

In order to explore the origins of the asymmetry of the in-plane torque in our annealed sample, I first review here the definitions of the differential conductance and spin transfer torkance. In MTJs, if I use the coefficients $G_{\sigma,\sigma'}$ of cross-channel conductance amplitude through any of the four spin channel combinations σ, σ', where σ or $\sigma'=\pm$ is the (majority/minority))-spin channel in the left (L) electrode, and similarly $\sigma'=\pm$ in the right (R) electrode, the expressions for the differential conductance in the P and AP states and the in plane spin transfer torkance will be as following [16]:

$$G_P = G_{++} + G_{--} \tag{4-2}$$

$$G_{AP} = G_{+-} + G_{-+} \tag{4-3}$$

$$\frac{d\tau_{//}}{dV} = \frac{\hbar}{4e}(G_{++} - G_{--} + G_{+-} - G_{-+})\hat{m}\times(\hat{m}\times\hat{M}) \tag{4-4}$$

Here, $G_{\sigma,\sigma'}$ is determined by the tunneling coefficient and the state density of the channel. In an ideal system (TMR is very large), $G_{++} >> (G_{+-}, G_{-+}) >> G_{--}$, and the in-plane torkance is dominated by the spin majority to majority channel. However, the device for the current induced magnetic switching has an ultra-thin barrier, ~1nm, thus other channels cannot be neglected due to dislocations and disorder at the interfaces or barrier subsystem (TMR is 90% in our annealed sample, much smaller than that predicted by theory in the ideal case).

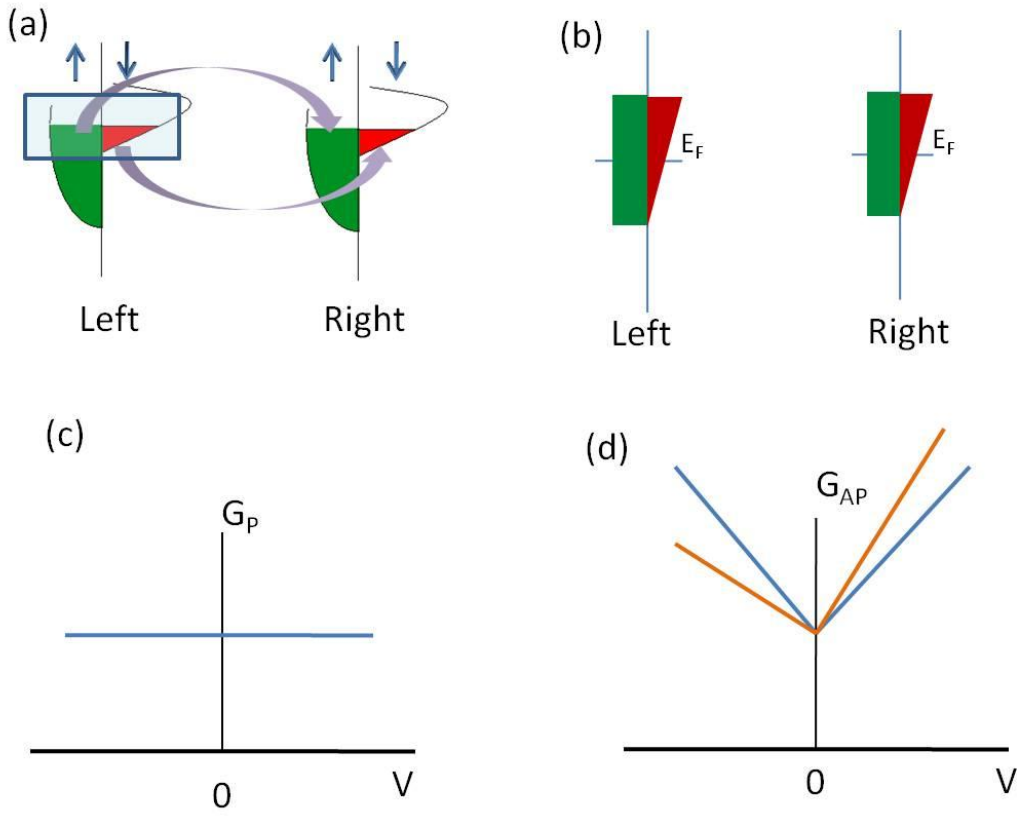

Figure 4-9. Model of the spin dependent tunneling. (a) Model of the spin dependent tunneling in MTJs. The majority bands are free electron like, thus small variation around Fermi energy level. The minority bands are dominant by the localized the d bands, strong bias dependent. (b) Simplified model by focusing on the low bias region, the blue window area in the (a), assuming $\rho_+ = const$ and $\rho_- = \rho_{-,0} + \frac{\partial \rho_-}{\partial V} V$ to first order in V in low bias region. (c-d) Schematic of predicted (c) parallel conductance G_P and (d) anti-parallel conductance G_{AP}. (Figure (d) is modified from Ref [16]).

In the paper [16], Slonczewski assumes $\rho_+ = const$ (electrons in majority bands are free electron-like) and $\rho_- = \rho_{-,0} + \frac{\partial \rho_-}{\partial V} V$ to first order in V. Considering both elastic tunneling and inelastic tunneling, $G_{\sigma,\sigma'}$ can be expressed as:

$$G_{++} = U_{++}\rho_+^0 \tag{4-5}$$

$$G_{--} = U_{--}\rho_{-,0}^2 \tag{4-6}$$

$$G_{+-} = G_{+-}^{el} + G_{+-}^{inel} = U_{+-}\rho_+(\rho_{-,0} + \rho_{-,1}V) + D_R|V| \tag{4-7}$$

$$G_{-+} = G_{-+}^{el} + G_{-+}^{inel} = U_{-+}\rho_+(\rho_{-,0} - \rho_{-,1}V) + D_L|V| \tag{4-8}$$

Here $U_{\sigma,\sigma'}$ is the elastic tunneling coefficient; D_L and D_R is the inelastic tunneling coefficient, reflecting the asymmetry of the concentration of defects or dopants in the interfacial microstructure;

Thus the G_P, G_{AP} and in-plane torkance are given by

$$G_P = G_{++} + G_{--} = U_{++}\rho_+^2 + U_{--}\rho_{-,0}^2 \tag{4-9}$$

$$G_{AP} = G_{+-} + G_{-+} = (U_{+-} + U_{-+})\rho_+\rho_{-,0} + (D_R + D_L)|V| + (U_{+-} - U_{-+})\rho_+ \frac{\partial \rho_-}{\partial V} V \tag{4-10}$$

$$\begin{aligned} \frac{d\tau_{//}}{dV} = \frac{\hbar}{4e}\sin\theta[&U_{++}\rho_+^2 - U_{--}\rho_-^2 + (U_{+-} - U_{-+})\rho_+\rho_{-,0} \\ &+ (D_R - D_L)|V| + (U_{+-} + U_{-+})\rho_+ \frac{\partial \rho_-}{\partial V} V] \end{aligned} \tag{4-11}$$

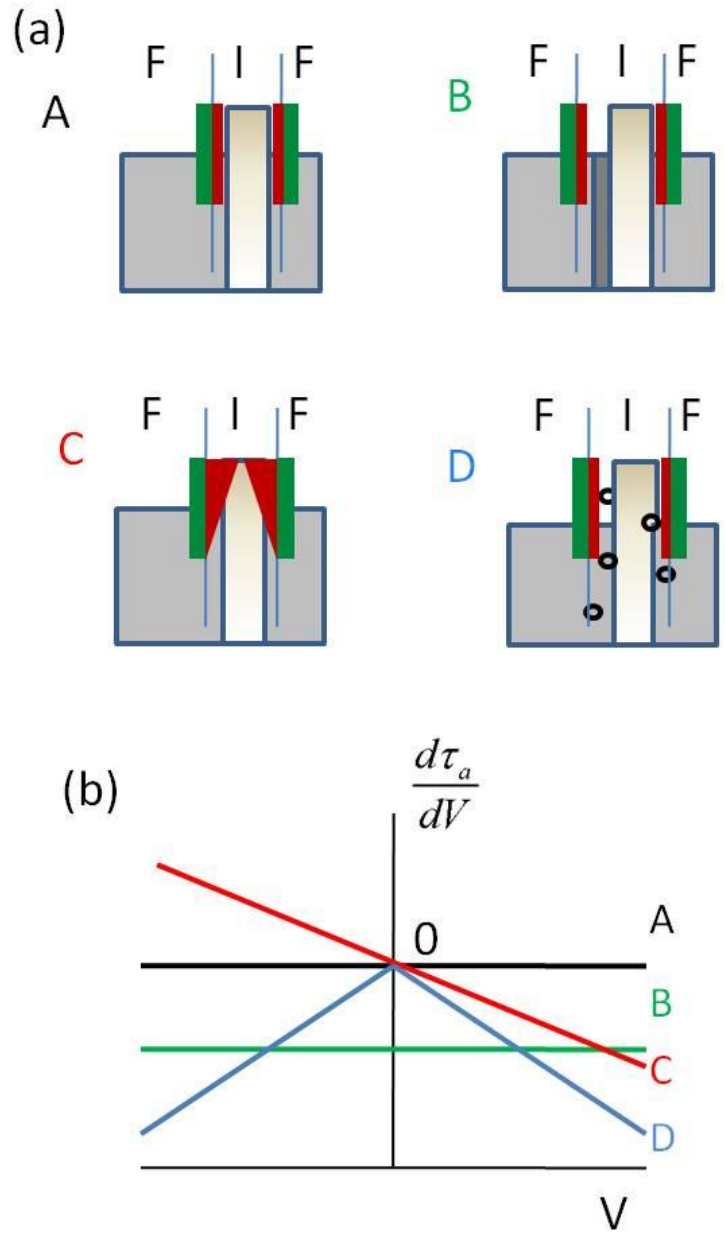

Figure 4-10. Schematic of tunnel and predicted adjusted torkance (a) Schematic of tunnel for A-D cases, F/I/F stands for FeCoB/MgO/FeCoB three layers and DOS at interface is shown in each case: The green plot is the DOS in majority bands and red represents minority DOS (b) Schematic of predicted adjusted torkance. The separate cases (A)–(D) are shown in the (a) and described in the text. ((b) is replotted from Ref [16]).

As shown in the Figure 4-9 (c-d), to the first order in bias, G_P is bias independent and G_{AP} is linearly dependent on positive and negative bias region respectively. The slope of the line in AP case is mainly determined by the inelastic tunneling coefficient D_R and D_L, while its asymmetry in terms of bias polarity is affected by the elastic-tunnel asymmetry $U_{+-} - U_{-+}$. To obtain a fuller representation of such data, I discuss the bias dependence of the in-plane torkance in the next section.

4.4.2 Adjusted torkance

To focus on the effects of interfacial microstructures of a compositionally symmetric MTJ, Slonczewski et al. compensate for the possible dependence of G_P on V by defining the adjusted torkance

$$\begin{aligned} d\tau_a / dV &= (\hbar / 4e)(G_{+-} - G_{-+})\hat{m} \times (\hat{m} \times \hat{M}) \\ &= d\tau_{//} / dV - (\hbar / 4e)G_p^{'}(V)\sin\theta \\ &= (\hbar / 4e)[(U_{+-} - U_{-+})\rho_+ \rho_{-,0} + (D_R - D_L)|V| \\ &\quad + (U_{+-} + U_{-+})\rho_+ \frac{\partial \rho_-}{\partial V} V]\sin\theta \end{aligned} \tag{4-12}$$

Where $G_P^{'} = [2P/(1+P^2)]G_P(V)$ and P is the spin polarization at $V = 0$ given by $P = \sqrt{(G_P - G_{AP})/(G_P + G_{AP})}$;

Since the term $d\tau_{//} / dV$ as a function of bias has been measured by ST-FMR (See Figure 4-6), with the results of $G_P(V)$ and zero bias polarization P, the bias dependence of $d\tau_a / dV$ can be plotted.

In the paper, five special cases are discussed, here we focus on the first four:

Case A: symmetric reference: $U_{+-} = U_{-+}$, $D_R = D_L$, $\frac{\partial \rho_-}{\partial V} = 0$, symmetric interfaces in both elastic tunneling and inelastic tunneling; no bias dependence of ρ_-. In that case, adjusted torkance is zero.

Case B: Asymmetry of elastic tunneling: $U_{+-} \neq U_{-+}$, $D_R = D_L$, $\frac{\partial \rho_-}{\partial V} = 0$, symmetric interfaces in terms of inelastic tunneling but asymmetric in elastic tunneling, ρ_- is constant. In that case, the adjusted torkance maintains constant but not zero.

Case C: First order dependence of DOS on energy: $U_{+-} = U_{-+}$, $D_R = D_L$, $\frac{\partial \rho_-}{\partial V} \neq 0$, symmetric interfaces in terms of elastic and inelastic tunneling, ρ_- is linearly dependent on bias. In that case, the adjusted torkance has a linear voltage dependence too.

Case D: Asymmetry of distribution of inelastic tunneling centers: $U_{+-} = U_{-+}$, $D_R \neq D_L$, $\frac{\partial \rho_-}{\partial V} = 0$, symmetric interfaces in terms of elastic tunneling but not in inelastic tunneling; no bias dependence of ρ_-. This gives a broken-linear dependence to the adjusted torkance. Depending on the sign of $D_R - D_L$, the torkance rises with

$|V|$, or falls, as shown in Fig. 4.10, which means that, in this example, there are more inelastic tunneling center on the left interface.

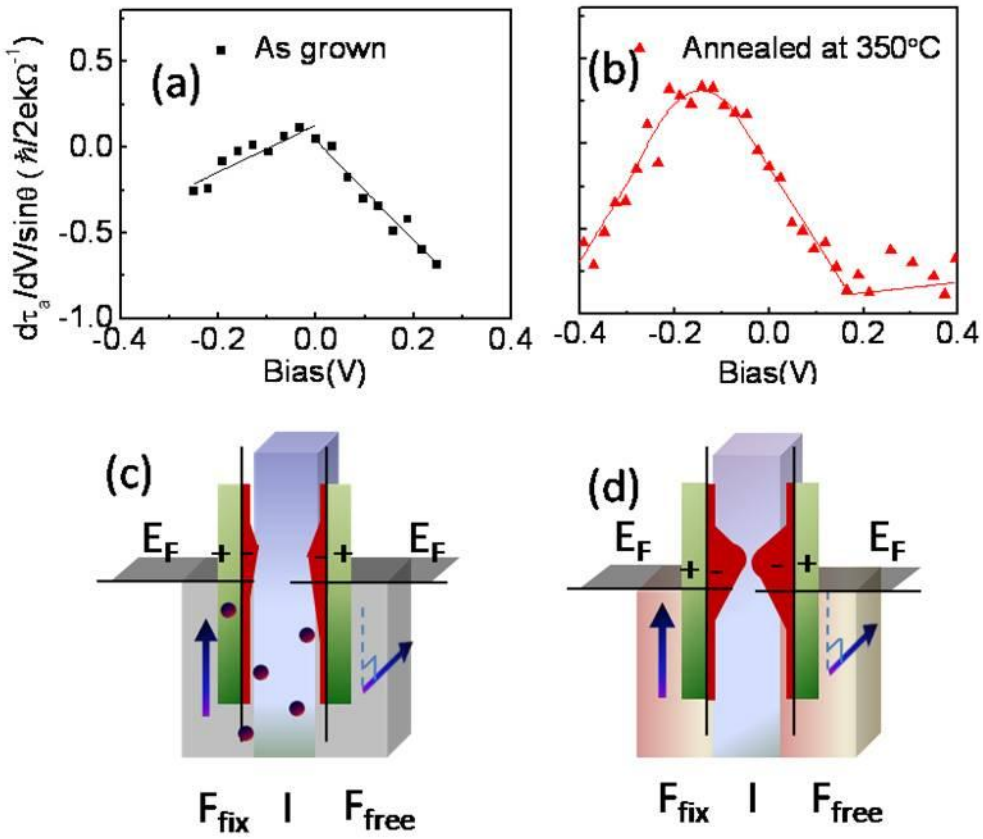

Figure 4-11. Adjusted torkance as function of voltage bias in (a) the as-grown case and (b) an annealed case in the $Fe_{20}Co_{60}B_{20}$/MgO/ $Fe_{20}Co_{60}B_{20}$ MTJs. (c-d) Schemas to show the tunneling cases: (c) As-grown: asymmetry of distribution of inelastic tunneling centers. (d) Annealed: elastic tunneling with a DOS peak in minority spin bands.

The plots of the bias dependent adjusted torkance in our as-grown and annealed samples are shown in Figure 4-11 (a-b). Compared with the four cases discussed above, I notice that the main features for the as-grown and annealed samples are quite different. For the as-grown MTJs, the adjusted torkance is mostly symmetric with $V = 0$, indicating that the $(D_R - D_L)|V|$ term is dominant. According to the adjusted torkance model, it can be attributed to an asymmetry in the distribution of inelastic tunneling centers cases with more scattering centers on the left interface. Besides the above main feature, the slopes of the adjusted torkance in the negative bias and positive bias regions are noticeably different, which means the term $(U_{+-} + U_{-+})\rho_+ \frac{\partial \rho_-}{\partial V} V$, the energy dependent DOS of minority band also plays a role in the bias dependence, although it is not as momentous as the effect from the inelastic tunneling.

In the annealed sample, the bias dependence of adjusted torkance has a distinctive signature. It linearly varies with voltage in the different bias regime, and roughly we can divide this behavior as following:

First region: $-0.4V$ to $-0.15V$, where the adjusted torkance is linearly varies with V, which means the term $(U_{+-} + U_{-+})\rho_+ \frac{\partial \rho_-}{\partial V} V$ dominates (elastic tunneling case with energy dependent DOS), and with the slope $(U_{+-} + U_{-+})\rho_+ \frac{\partial \rho_-}{\partial V} V > 0$, thus $\frac{\partial \rho_-}{\partial V} > 0$.

Second region: $-0.15V$ to $0.15V$, where the adjusted torkance is also linearly dependent on V, but with the slope $(U_{+-}+U_{-+})\rho_{+}\frac{\partial\rho_{-}}{\partial V}<0$, thus $\frac{\partial\rho_{-}}{\partial V}<0$.

Third region: $0.15V$ to $0.4V$: where the adjusted torkance plot is almost flat, corresponding to the simple elastic tunneling case with $\frac{\partial\rho_{-}}{\partial V}\approx 0$.

Looking at the three regions together, our results suggest that after annealing the DOS of minority spins cannot be considered as a constant; instead there is a peak located approximately $0.15V$ above the Fermi energy.

It has been previously reported that interface states can have a marked effect on the spin dependent tunneling [24-27]. A shape peak in DOS of the minority band located around $0.1V\sim 0.2V$ above the Fermi level in single crystalline Fe (100) has been investigated by STM (see Figure 4-12(a)), and separately by electrical and optical measurements (Figure 4-12(b)) [28-31]. Therefore, I attribute the peak in the DOS of minority band indicated in our adjusted torkance measurement to the interfacial state of crystalline Fe.

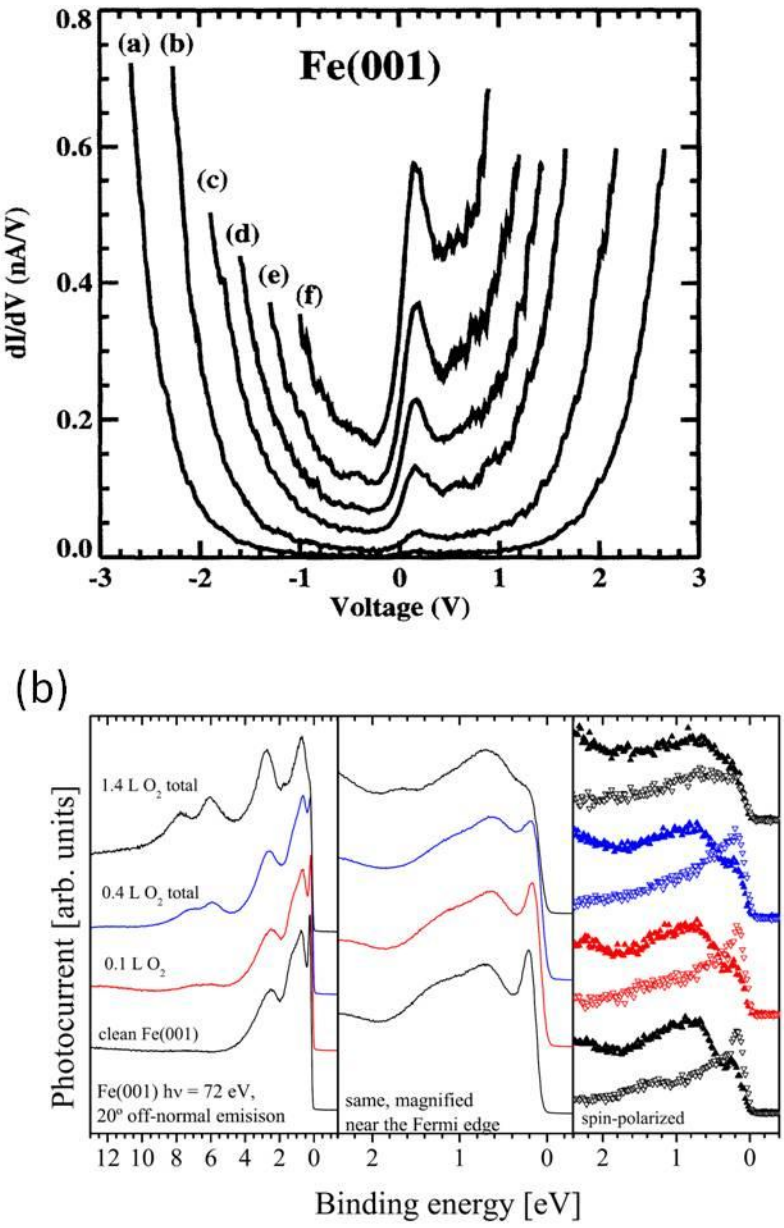

Figure 4-12. Interfacial minority states in Fe (100). (a) Tunneling conductance vs sample voltage measurements of an Fe(001) surface obtained at constant height above the Fe surface. (Figure from Ref. 28); (b) Oxygen adsorption on Fe (001); Both spin-integrated (left and center panels) and spin-polarized (right panel) spectra are shown; Δ majority states and ∇ minority states (Figure from Ref. 30).

I usded schematics as show in Fig. 4-11(c-d) to illustrate the tunneling mechanisms for two different cases, as-grown and annealed. For the as-grown sample, inelastic tunneling determines the bias dependence of the in plane torque. Specifically, the distribution of inelastic tunneling centers is asymmetric, with more scattering on the left side (interface with the bottom electrode). This asymmetry is probably due to the film growing process: the left interface (between the bottom electrode and the tunneling barrier) is further oxidized or damaged by oxygen plasma during the following MgO sputtering, which does not happen for the right interface (See Figure 4-14 (a) and (c)). After annealing, the dominant tunneling mechanism is elastic tunneling with DOS dependent on energy. Especially there is a DOS peak (probably interface states of electrodes) in minority bands located just above the Fermi level. Considering the main difference between those two samples is the crystalline structure of the $Fe_{20}Co_{60}B_{20}$ (Figure 4-13), our results indicate that: first, the inelastic tunneling is favored in the MTJs with amorphous electrodes, while the annealed samples exhibit more elastic tunneling. Since B can diffuse out of the electrode and react with ferromagnetic oxides at the interface with the MgO during the annealing (see Figure 4-14 (b) and (d)), the interfaces can be improved in this manner. With improved interfaces and a structurally more uniform tunnel barrier afer annealing, inelastic tunneling is depressed, leading to a much higher TMR. Second, samples with crystalline electrodes have much sharper feature in minority DOS close to Fermi level than those with amorphous FeCoB layers, which is reasonable because the disorder in crystalline structure usually acts to broaden the DOS peaks [32,33] (See Figure 4-15) .

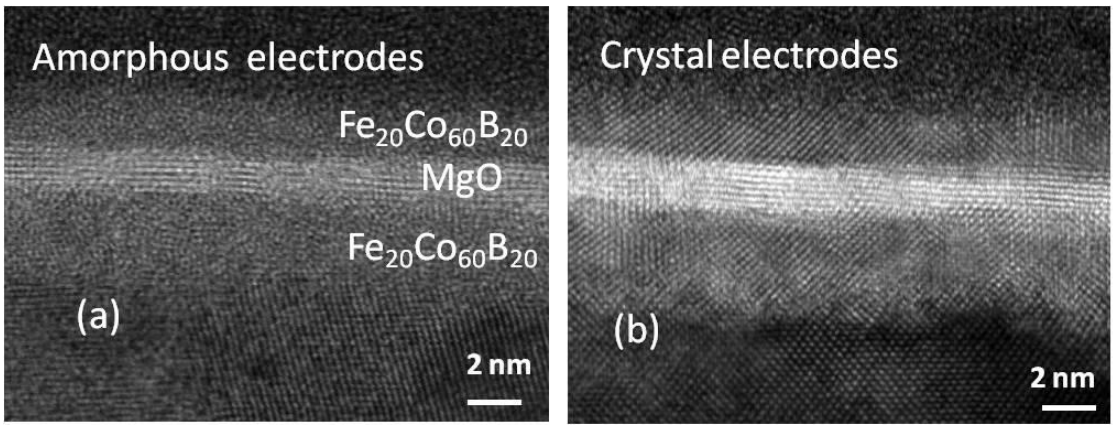

Figure 4-13. STEM images of a MTJ (a) the as-grown and (b) annealed junctions. The sample studied by TEM has the same layer structure as the device sample but with thicker barrier and electrodes (Data courtesy of Pinshane Huang).

4.4.3 Inelastic tunneling vs. elastic tunneling

Furthermore, the effects of interfacial microstructure can be expected in the bias dependence of G_P, G_{AP} and thus TMR.

For G_{AP}, according to Equation 4-10

$$G_{AP} = G_{+-} + G_{-+} = (U_{+-} + U_{-+})\rho_+\rho_{-,0} + (D_R + D_L)|V| + (U_{+-} - U_{-+})\rho_+ \frac{\partial \rho_-}{\partial V} V$$

Figure 4-16 (a-b) shows that the bias dependence of G_{AP} is weaker in the annealed sample, which means that the inelastic tunneling coefficient $(D_R + D_L)$ is reduced, consistent with our conclusion: the inelastic tunneling effect is diminished in the system with crystalline electrodes.

4.4.4 Interface states in the minority band

Moreover, regarding G_P as being directly related to the DOS of majority and minority spin, interface states may also be the explanation for the local maximum and minimum in the plot of G_P as a function of voltage in the annealed sample in low bias region (See Figure 4-16 (d)). With the assumption that $\rho_+ = const$ and $\rho_- = \rho_{-,0} + \frac{\partial \rho_-}{\partial V} V$, G_P can be presented as

$$G_P = G_{++} + G_{--} = U_{++}\rho_+^2 + U_{--}\rho_{-,0}^2 - \frac{1}{2}U_{--}(\frac{\partial \rho_-}{\partial V}V)^2 \qquad (4\text{-}13)$$

to second order of V. Thus the variation of the DOS in minority band will cause a decrease of G_p with increasing $|V|$ in low bias region, which is opposite to the effect of ideal ballistic tunneling, exponentially increase with bias. When two effects play together, rich features such as peaks and dips can be anticipated. And for the as-grown sample, the effect from the DOS is negligible, so the G_P is monotonicly dependent on bias. Another interesting result is that the plot of G_P vs. V shows an asymmetric behavior with bias direction. This feature may indicate either an asymmetry of the interfaces or of the barrier, which we will discuss later in this chapter.

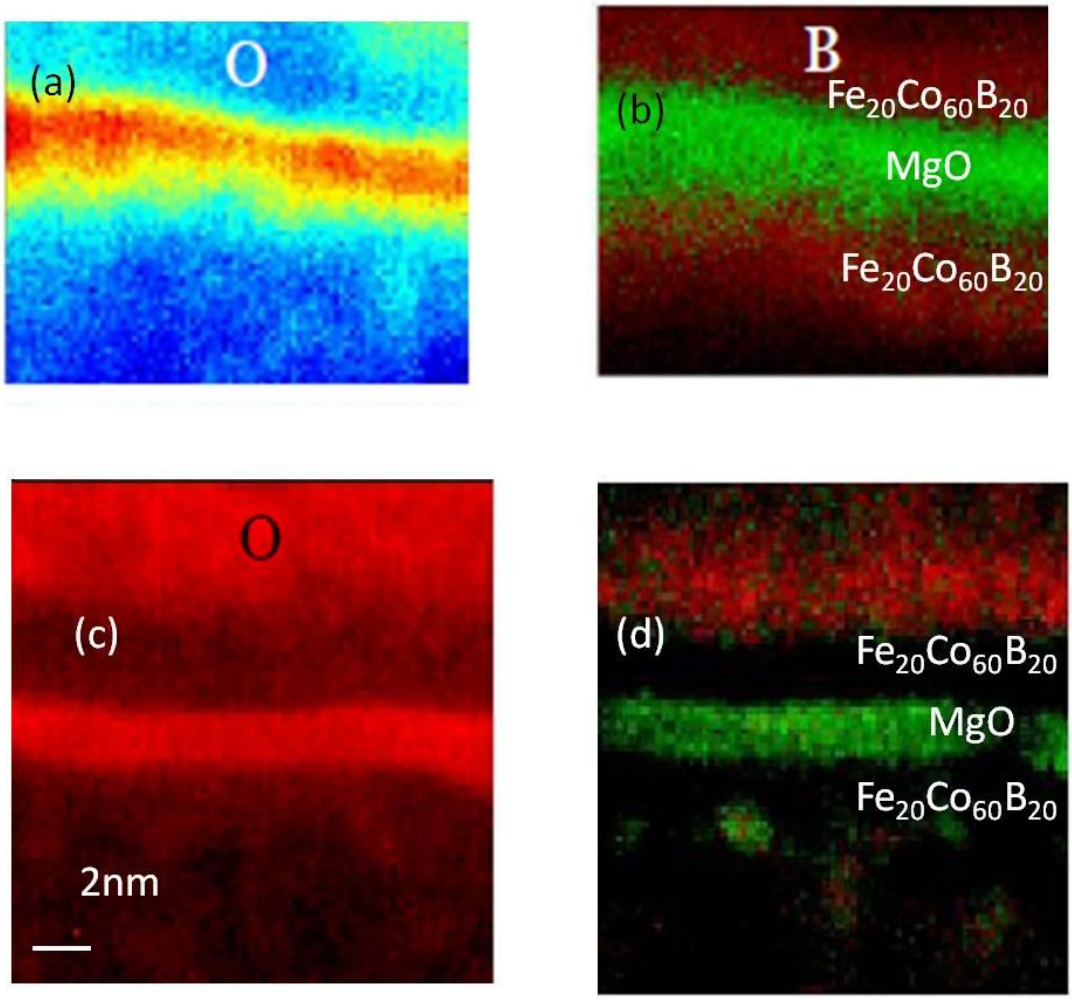

Figure 4-14. Spectroscopic images of the MTJ stack (a-b) before and (c-d) after annealing in a color scheme. (Data courtesy of Pinshane Huang). All the images are in the color scale. In (a), the color change from blue to red indicates the O density from zero to maximum, while in (c), black yields empty and red yields maximum. In (b) and (d) Red yields unreacted B and green yields B-oxide.

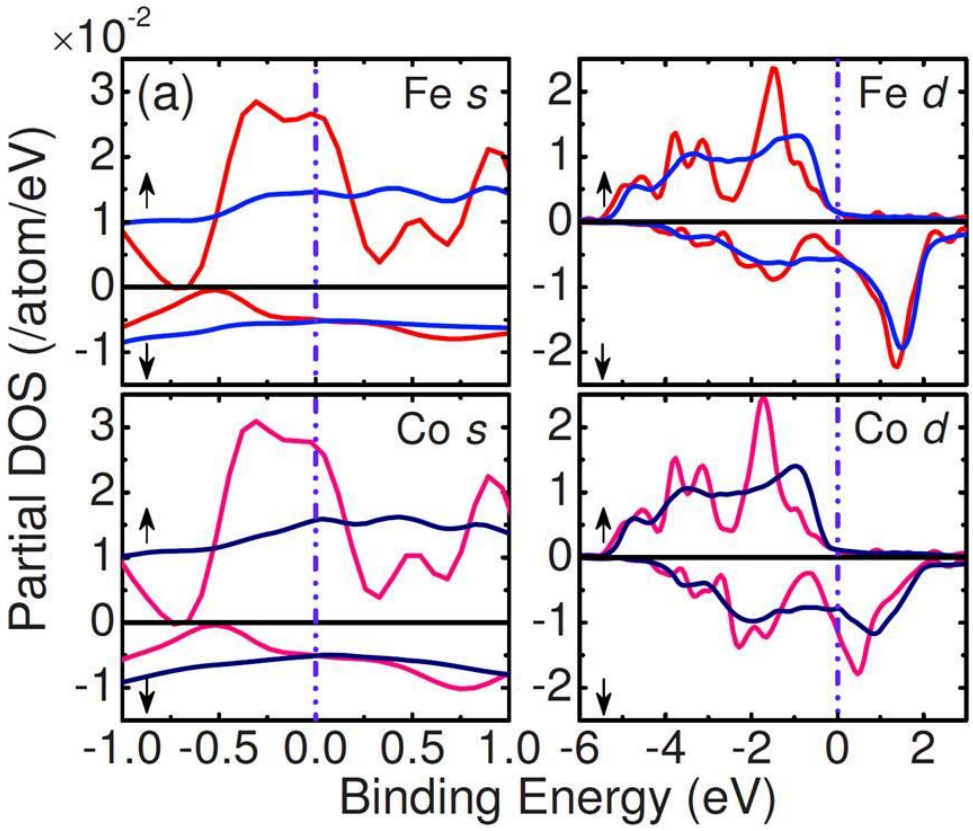

Figure 4-15. Spin-resolved *s*- and *d*-partial DOS for Fe and Co in amorphous (blue and navy) and bcc crystalline (red and pink) $Co_{70}Fe_{30}$ alloy structures. Upward (downward) black arrow denotes majority (minority) spin. (Figure from Ref. 32).

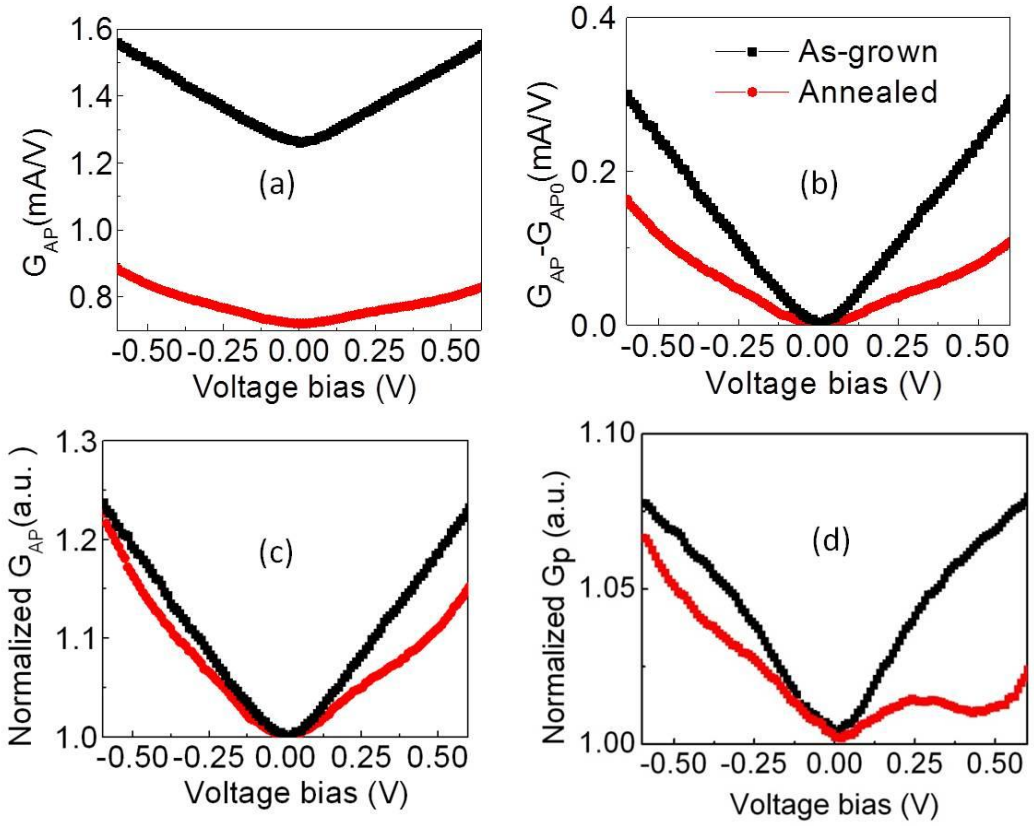

Figure 4-16. Bias dependence of conductance for both annealed and as-grown $Fe_{20}Co_{60}B_{20}/MgO/Fe_{20}Co_{60}B_{20}$ samples: (a) Differential conductance in the AP configuration, normalized differential conductance in (c) AP configuration and (d) P configuration. Plot (b) shows the relative change of with bias G_{AP} (defined as $G_{AP} - G_{AP0}$, here G_{AP0} is the differential conductance measured at zero bias), the bias dependence of G_{AP} is stronger in the as-grown sample, indicating that inelastic annealing plays a more significant role.

An energy dependent ρ_- can also explain the asymmetry of the bias dependent G_{AP} (Fig 4-16 (c)) and a bias dependent TMR (Figure 4-5 (a)). Since G_{AP} can be expressed as

$$G_{AP} = G_{+-} + G_{-+} = (U_{+-} + U_{-+})\rho_+\rho_{-,0} + (D_R + D_L)|V| + (U_{+-} - U_{-+})\rho_+ \frac{\partial \rho_-}{\partial V} V$$

The asymmetry comes from the term $(U_{+-} - U_{-+})\rho_+ \frac{\partial \rho_-}{\partial V} V$. As we discussed above, annealing could considerably increase $\left|\frac{\partial \rho_-}{\partial V}\right|$, and therefore affect the symmetry.

Meanwhile, owing to the peak in the minority band above the Fermi energy, more states will be available for channels G_{+-} and G_{-+} for a negative bias than for a positive bias, and this may be the reason for the smaller TMR in the negative bias direction

4.4.5 Other explanations

A wealth of mechanisms have been invoked to predict or explain the origin of asymmetry of the in plane spin torque. Generally, there are three main factors that can contribute to the asymmetry: (1) asymmetric interfaces; (2) impurities in the barrier and (3) intrinsic properties of the MTJ, which can be sensitively tuned by the exchange splitting [55] or s-d exchange energy [34] of the electrode material.

As I have noted above evne an MTJ with symmetric electrodes may have asymmetric interfaces due to details of the growth process [17] (See Figure 4-17 (a))

resulting in more B-oxide being formed at the bottom interface after annealing. However, this asymmetry is not observed in our STEM and EELS measurements. The STEM/ EELS chemical maps for B and Fe are shown in the Figure 4-17(b-c). In our annealed sample, B diffuses into the MgO, resulting in a Mg–B–O tunnel barrier and almost no B is left in the electrodes. Besides, I deposited two types of devices with the similar layer structure except that one is bottom pinned (IrMn underneath the junction) and one is top pinned (IrMn above the junction). (Details can be found in the section 4-6). In terms of G_P as function of voltage bias, the symmetry of the curves is similar in as-grown samples but opposite for the annealed sample. Thus I conclude that the chance that the asymmetry comes from dissimilar interfaces that resulted from deposition process is small.

Another possible explanation for the asymmetry in the torkance is that the non-equilibrium diffusion of the elements from the neighboring layers to the interfaces induces an asymmetry in the electronic states of the interfaces. Here I could not exclude that case, but even it is true, it's still hard to explain the turning points in the bias dependent in-plane torque. On the other hand, the explanation that a peak in the density of interfacial states above the Fermi level is responsible for the asymmetry does not require that the DOS of the minority states is the same at both interfaces . At least qualitatively similar behavior is predicted by the adjusted torkance model if the DOS peak exists at either one or both interfaces.

Impurities mediated tunneling is another candidate for the asymmetry of the bias dependent in-plane torque [8]. Disorder in the barrier (especially oxygen

vacancies) can create impurity energy levels and cause the presence of a bias asymmetry for the switching current or in-plane torque. However, it has been observed that annealing should improve the barrier quality and thus reduce the oxygen vacancies [11]. In that case, the asymmetry of the in-plane torque in our sample should be reduced instead of being enhanced upon annealing. For that reason, I argue that impurities and defects in the barrier are not the likely explanation for the asymmetry in our annealed sample.

Both the free electron model and the tight binding model predict an anomalous bias dependence of spin torque [34,55]. Theodonis et al. [55] point out the underlying mechanism for bias dependence is the interplay of spin currents in the antiferromagnetic configuration, or in other words, the term $(G_{+-} - G_{-+})$, which can be dramatically tuned by exchange splitting of the electrode. However, their simulation indicates that an increase of the exchange splitting can cause an enhancement of the field-like torque and and a reduction of the asymmetry term of the in-plane torque. Conversely, my experiment results show that annealing increases the field-like torque and at th same time enhances the asymmetry of the bias dependence of the in-plane torque. Thus, I conclude that a factor other than the exchange splitting, plays the more significant role in determining the anomalous bias dependence of the in-plane torque, and I propose that the minority spin band structure is the most likely candidate.

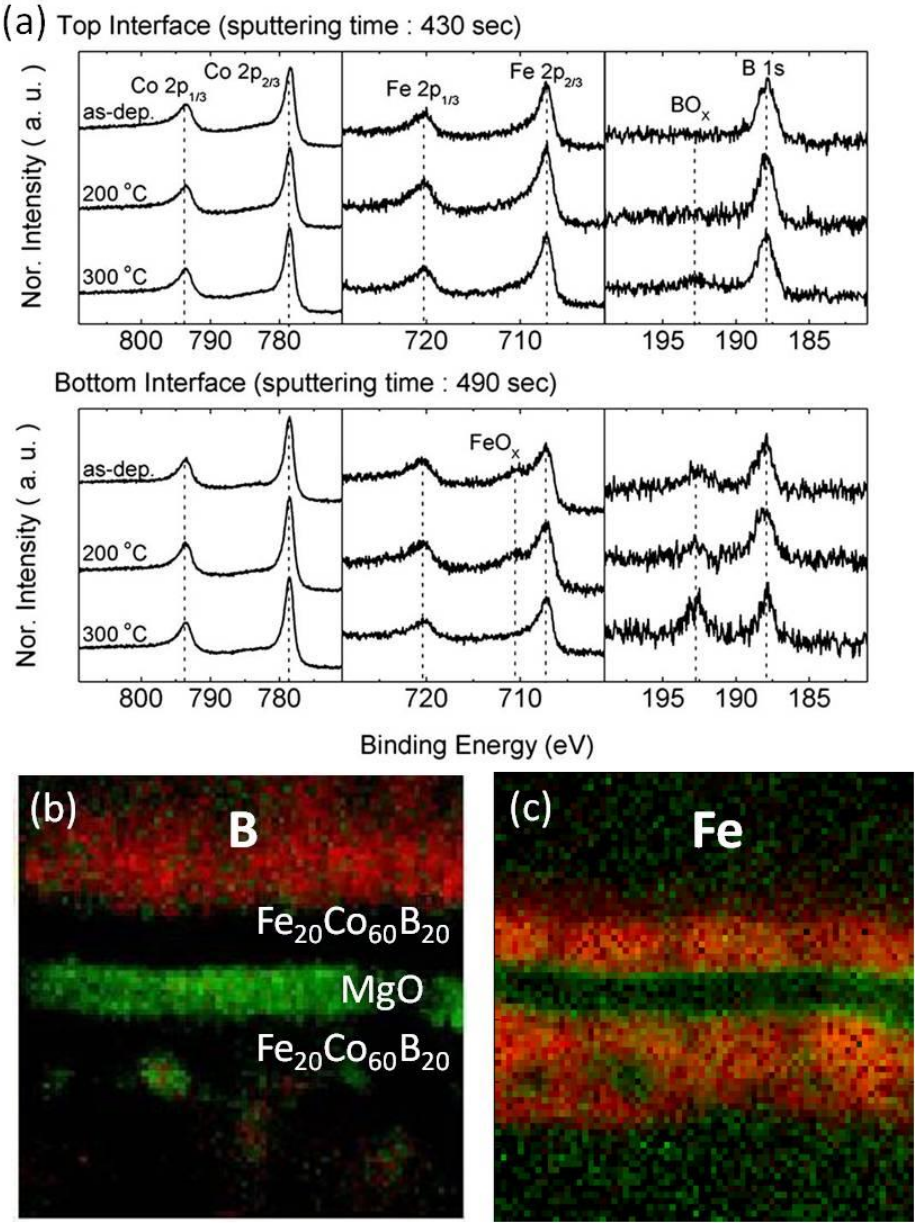

Figure 4-17. XPS and STEM data (a) Normalized XPS spectra of Co, Fe, and B in a $Fe_{20}Co_{60}B_{20}$/MgO/$Fe_{20}Co_{60}B_{20}$ tunnel junction at the top interface and the bottom interface. The data indicate more BOx at bottom interface (From Ref [17]) (b) STEM EELS chemical map for (b) B or (c) Fe of our annealed sample. In (b), Red yields unreacted B and green yields B-oxide; in (c) Red yields metal Fe and green yields Fe-oxide. (Data courtesy of Pinshane Huang).

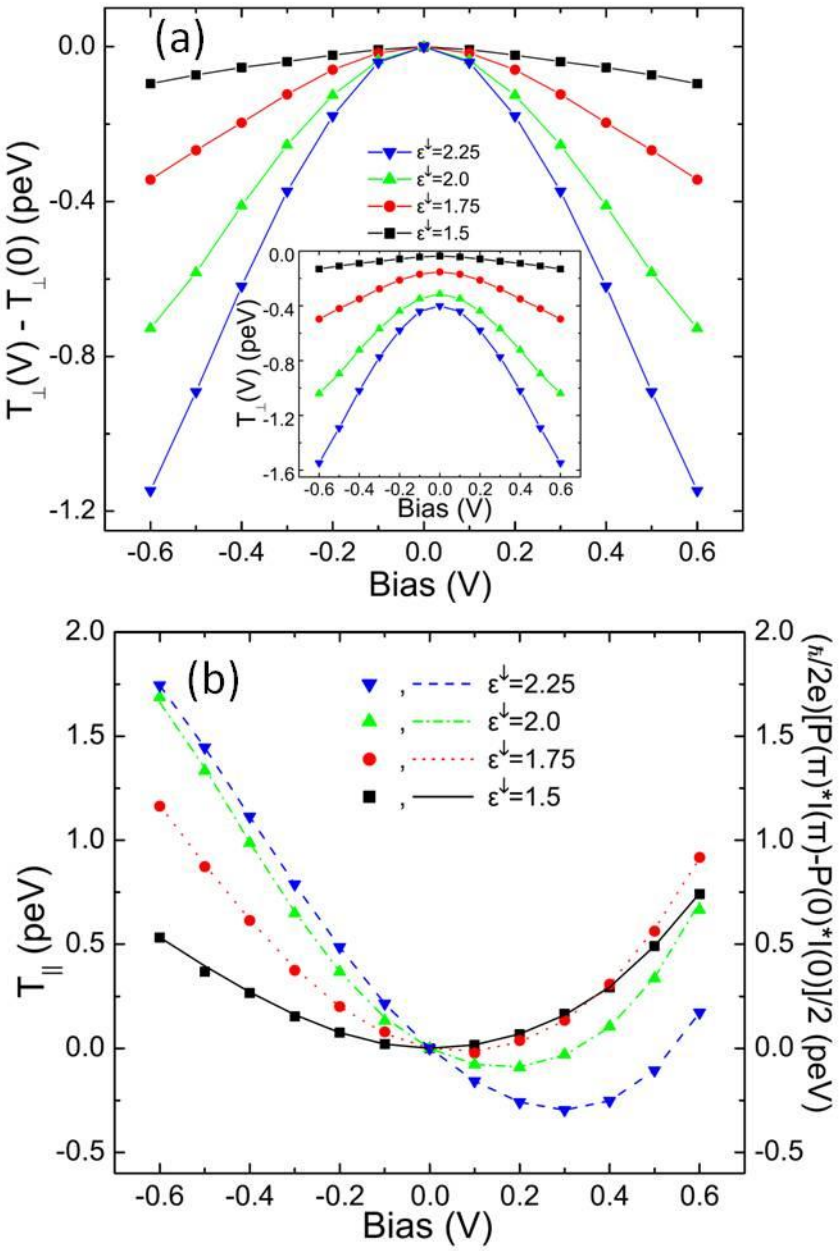

Figure 4-18. Predicted bias dependence of the current-induced STTs (a) perpendicular component of the net spin torque per unit area and (b) in-plane component with various values of $\varepsilon^{\downarrow}$, spin down energy term (From ref. 55).

4.4.6 Bias dependence of the field-like torque

Here I discuss possible reasons for the increase in the field-like torque strength during the annealing. Interlayer exchange coupling (IEC), dominated by coherent tunneling of the electrons below the Fermi energy, has a strong influence on the magnitude of the field like torque. Meanwhile, the IEC is extremely sensitive to the property of the interface. When interface becomes well-crystallized, the coefficient of elastic tunneling should increase, and consequently in the result can be expected to be an enhancement of the spin polarization as well as IEC. Furthermore, structural relaxation and oxidation conditions may also affect IEC in MTJs [35]. A significant amount of stress relief of the barrier as well as a reduction in the ferromagnetic oxide content at the interface as the result of annealing has been observed by STEM [10,11]. These effects can be reasonably be expected to further result in an increase in the field-like torque.

4.5 Samples with different RA product

In this chapter, I used ST-FMR for the measurement of the bias-dependent spin torkanc, detecting the resulting magnetic precession via the read-out of a resultant dc mixing voltage. In Ref [7,23], it is pointed out that this technique is only accurate at small $|V|$ due to an artifact associated with small changes in the dc resistance of MTJs that can result in response to a microwave drive. However, the sample studied in this paper has an higher RA ($\sim 20\Omega\mu m^2$) than the sample measured in [7] ($1.5\Omega\mu m^2$), thus I expected that our devices can be biased to higher DC voltage still with reasonable

accuracy as discussed [7,23]. Consistent with that expectation, I note that my high RA sample had the same layer structure but thicker MgO (RA ~ $15\Omega\mu m^2$) as the sample studied by time-domain techniques, and the results that I obtained are in good qualitativel agreement with the data shown in [7] in the range below 0.4V.

The above results also suggests that the feature of the in-plane torque as function of bias is not dependent on RA. As discussed above I attribute the asymmetry of the in-plane torque in the annealed sample to the feature of DOS of minority spin, which is related to the locations of the local minimums and maximums in *Gp* measurement. If it is true, those locations should not change with the RA variation. To check this I patterned high RA junctions into micron junctions formed from a wafer where the MgO was deposited wedge structure to obtain MTJs with different MgO thicknesses. Some results *Gp* vs. *V* are shown in Figure 4-19. The local minima in the $G_P(V)$ curves do not change with a decreasing RA product, indicating that this feature is indeed determined by the electrodes instead of the tunnel barrier.

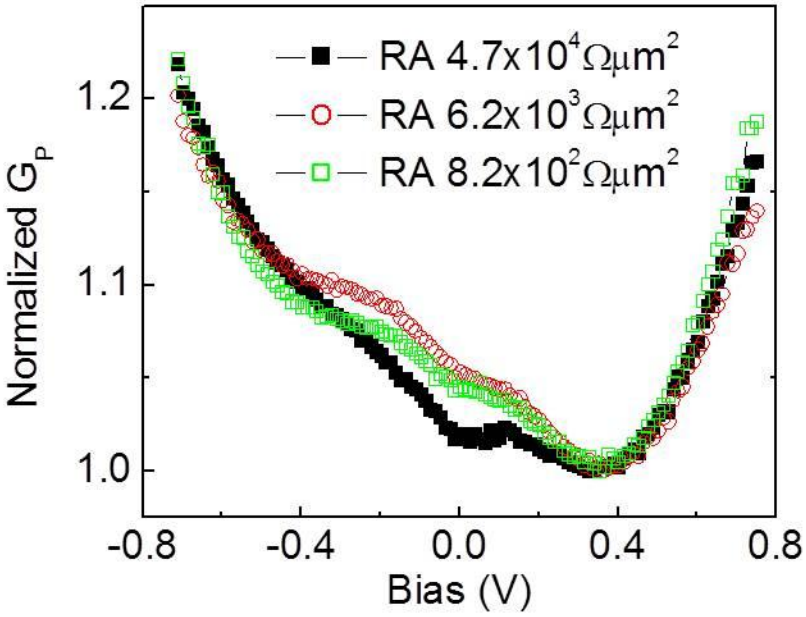

Figure 4-19. Bias dependence of normalized differential conductance in P configuration for the annealed InMn/ $Fe_{40}Co_{40}B_{20}$/ MgO/ $Fe_{40}Co_{40}B_{20}$ samples with different MgO tunnel barrier thickness.

4.6 Asymmetry of the bias dependence of differential conductance

In the previous section, I discussed the possible explanation for the local minimum and local maximum in the $G_P(V)$ curves, but another interesting behavior in the parallel conductance is its asymmetry in terms of the bias direction. To investigate the origin of this asymmetry and to study its relationship to the layer structure, I made and measured three different kinds of MTJs: bottom contact/IrMn 8 / $Fe_{40}Co_{40}B_{20}$ 2/ MgO1/ $Fe_{40}Co_{40}B_{20}$ 1.5/ top contact (in nm); bottom contact/ $Fe_{40}Co_{40}B_{20}$ 2/ MgO1/

$Fe_{40}Co_{40}B_{20}$ 1.5/IrMn 8/top contact and bottom contact/ $Fe_{40}Co_{40}B_{20}$ 1.5/ MgO1/ $Fe_{40}Co_{40}B_{20}$ 8/top contact.

Figure 4-20 shows $G_P(V)$ for the as-grown and annealed cases. For the as-grown samples, the asymmetry is independent of location of the IrMn pinning layer. Conseqeuntly I suspect that this asymmetry is due to the different degree of oxidation of the top and bottom interfaces. Owing to the thin film deposition process, the bottom interface is probably over-oxidized during the MgO sputtering. On the other hand f or the annealed samples, it seems clear that the asymmetry is determined by the location of the pinning layer.

This type of asymmetry suggests that a non-symmetric barrier profile could be the explanation. The bottom ferromagnetic electrode was grounded during the measurements. Under that bias condition, the electrostatic potential $\varphi(x)$ can be rewritten as

$$\Phi(x) = V_0 - Ex \tag{4-14}$$

where E is the simplified equivalent electric-field strength in the tunnel barrier area when the barrier layer is biased. V_0 is the mean inner potential and x is the distance across the barrier.

The barrier potential asymmetry can be strongly modified by the presence of an internal electric field. The tuning of the barrier asymmetry as a function of applied voltage is illustrated schematically in Figure 4-21. Here the left electrode, which

corresponds to the bottom electrode in the sample growth direction, is grounded. I assume a trapezoid-shaped barrier potential is formed under the zero bias condition (Figure 4-21(b)). When negative bias voltage is applied (Figure 4-21(c)), the left-hand side of the barrier is pushed up to lower the barrier height. In contrast, when a positive bias voltage was applied, the trapezoid shape is reversed as compared to the negative bias voltage (Figure 4-21(d)) and increases the effective barrier height first. Thus the asymmetry of $G_P(V)$ can be expected with this model.

Asymmetric tunnel conductance curves have been reported for MTJs with the same top and bottom electrode materials with various types of tunneling barriers; TaO_x [36], AlO_x [37] or MgO [38]. Such an asymmetry may be caused either by a difference in work function for the two electrodes, an inhomogeneous oxygen distribution in the barrier , resulting in a varying band gap, or a combination of the two. Since there is no direct evidence for an asymmetric oxygen distribution in the barrier, I suspect that this asymmetry in the $G_p(V)$ curves is related to asymmetry in the nature of the interfaces, which I tentatively attribute to the diffusion of Mn from the pinning layer which results, I suggest, in the generation of fixed negative charge in the part of the tunnel barrier that is closest to the IrMn layer.

4.7 Temperature dependence

The study of the temperature dependence of physical phenomena is offetn essential for obtaining a better understanding of the underlying physics, since it provides important clues into the detailed physical mechanism. Recently, temperature dependent studies

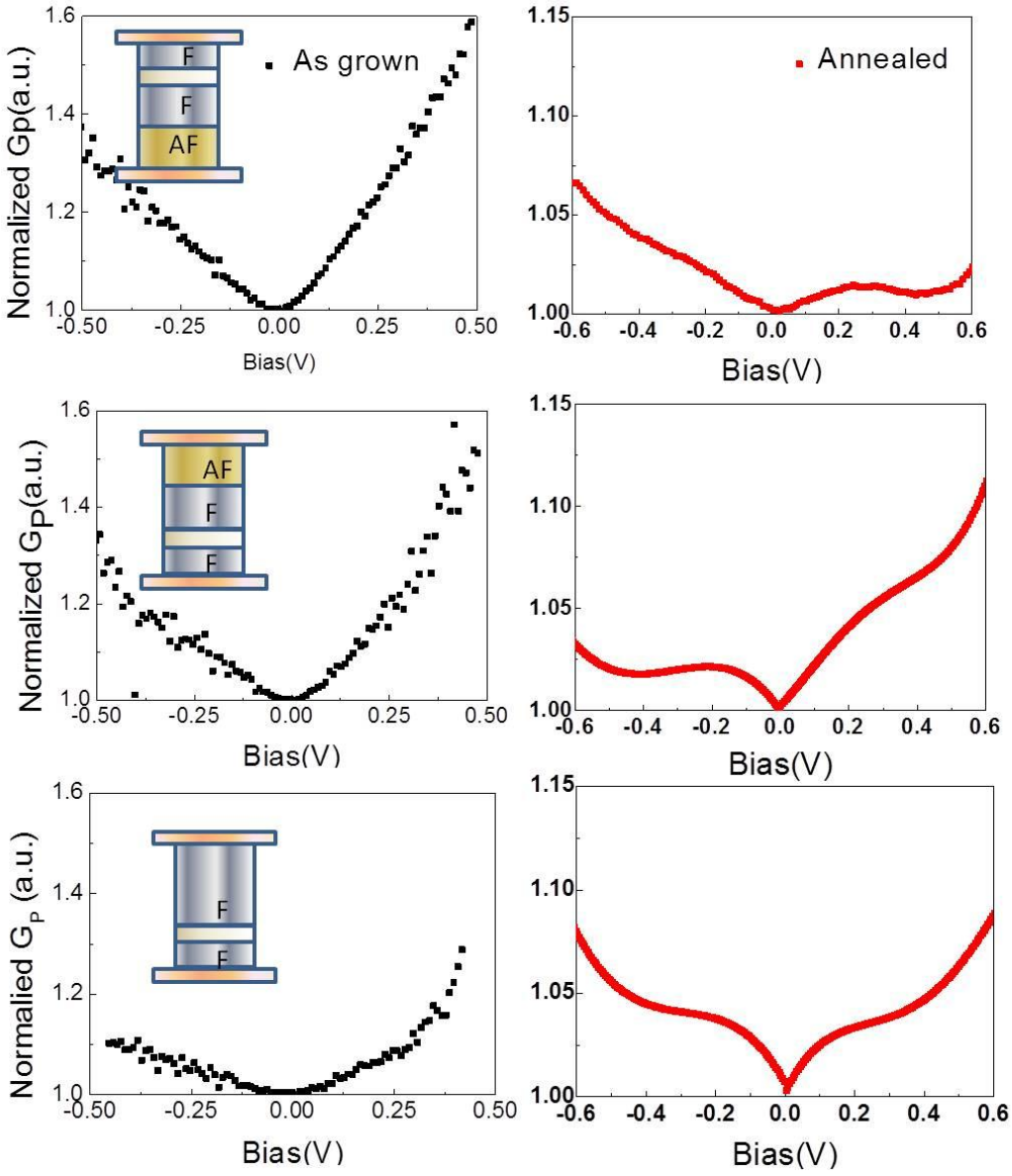

Figure 4-20. Bias dependence of normalized differential conductance in P configuration for both annealed (red dots) and as-grown (black dots) measured in the $Fe_{40}Co_{40}B_{20}$/ MgO/ $Fe_{40}Co_{40}B_{20}$ devices with various structure configurations: (a-b) IrMn at bottom, (c-d) IrMn on the top and (e-f) no IrMn pinning.

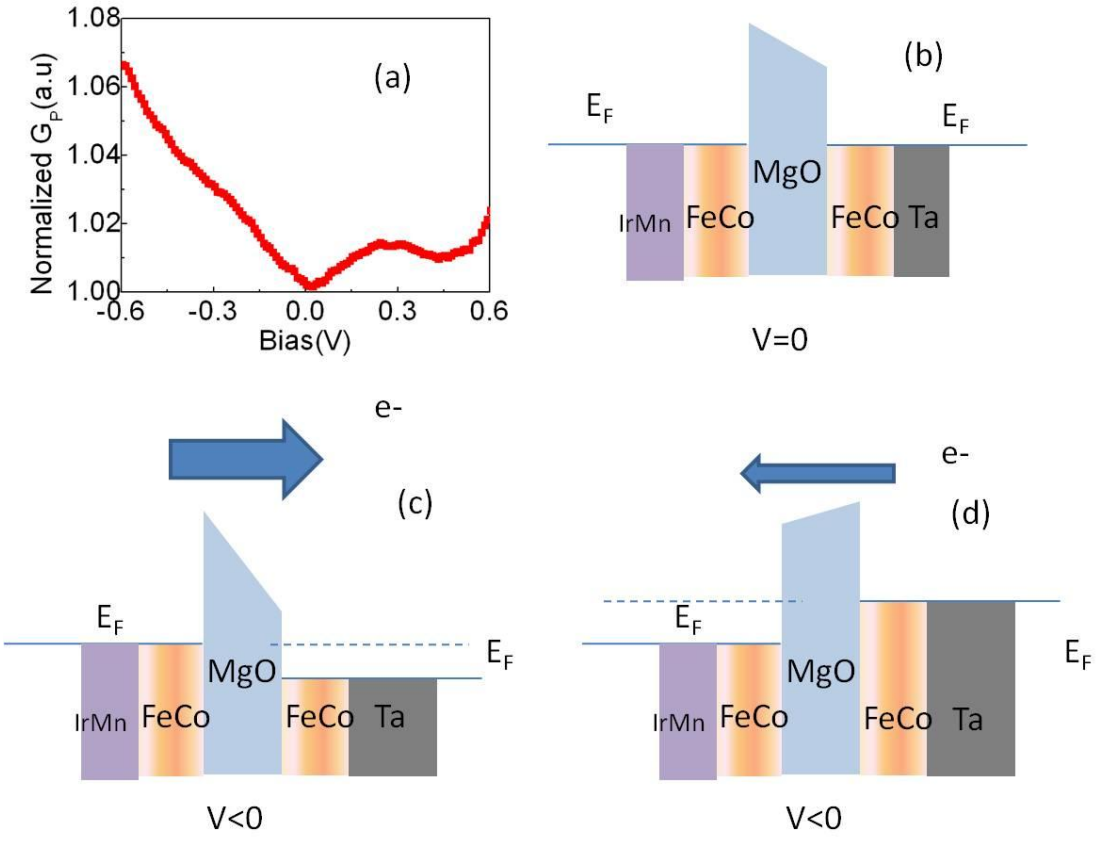

Figure 4-21. Schematic of asymmetric barrier potential. (a) Normalize differential conductance in P configuration for the annealed InMn/ $Fe_{40}Co_{40}B_{20}$/ MgO/ $Fe_{40}Co_{40}B_{20}$ sample as a function of bias. (b-d) Schematic of energy band diagrams with (b) V=0, (c) V<0 and (d) V>0.

on MTJs have mainly focused on the inelastic electron tunneling spectrum (IETS) [39-41,53], the conductance and the TMR behavior [42-44]. These results show that TMR is enhanced at the low temperature due to suppressed magnon scattering. In addition interfacial defects and defect-induced phonon and magnon states result in inelastic scattering of the tunneling electrons and enhance the low bias conductance by opening

new conductance channels above and below the Fermi energy. In the case of magnon scattering, spin- dependent contributions to the electrical conductivity can be expected because of the spin-flip scattering of tunneling electrons.

In Section 4-4 above, I discussed the use of the adjusted torkance model to fit ST-FMR data measured at room temperature. To better understand the temperature contribution on STT, I measure samples by ST-FMR from room temperature to 10K by cooling down in liquid helium.

4.7.1 Temperature dependence of TMR

The temperature dependence of magneto-electric properties of one of these MTJs is shown in Figure 4-22 (b-d). In these annealed devices, the resistance R_{AP} increases rapidly with decreasing temperature, whereas R_P hardly changes at all on cooling, resulting in a TMR ratio increase from 97% at RT to 130% at 10K under zero bias. Similar changes in the magneto-resistance of MTJs with temperature have been observed previously and have been explained by magnon assisted tunneling, which involves a spin-flip of the tunneling electron [40, 48, 49]. Interfacial magnons significantly contribute to the spin transport in MTJs. At low temperature, the magnon emission opens spin-flip channels for hot minority electrons that increase with the bias voltage. Consequently the conductivity in the AP state increases much faster than the conductivity in the P state, leading to a drop in TMR with increasing T.

I also investigated the bias dependent conductance in the P and AP states as a function of temperature. The plot shown in Figure 4-23(c) demonstrates that the local maximums and minimums in P configuration are more distinct at low temperature,

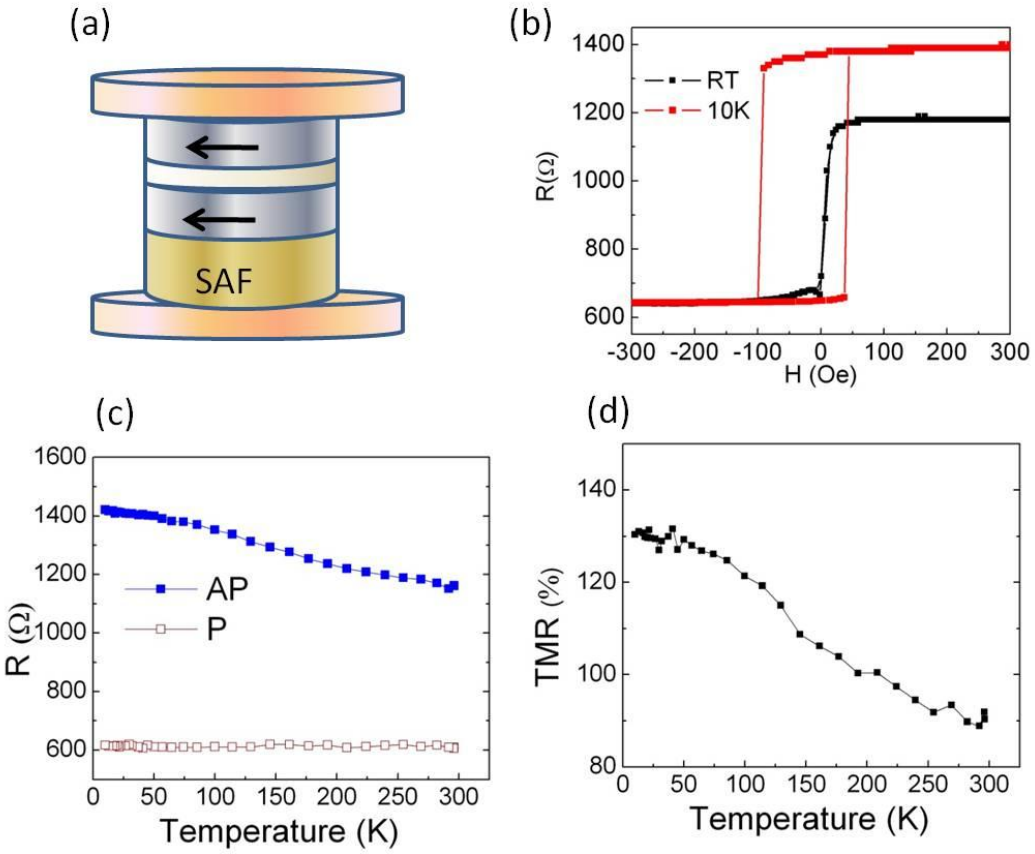

Figure 4-22. Temperature dependence of MR. (a) Schematic of the layer structure of our samples. (b) R-H loop measured in the room temperature and 10 K. (c) Resistance of the device as a function of the temperature in P or AP configuration. (d) Temperature dependence of TMR. TMR is enhanced from 97% at RT to 130% at 10K under zero bias.

with observation of other groups[45]. If I remove the anti-symmetric part of G_P (V), which may be due to asymmetric interfaces or non-uniform fixed charge in the barrier, as I discussed in Section 4-6, and only show the symmetric contribution, this feature is even clearer (See Figure 4-23(d)).

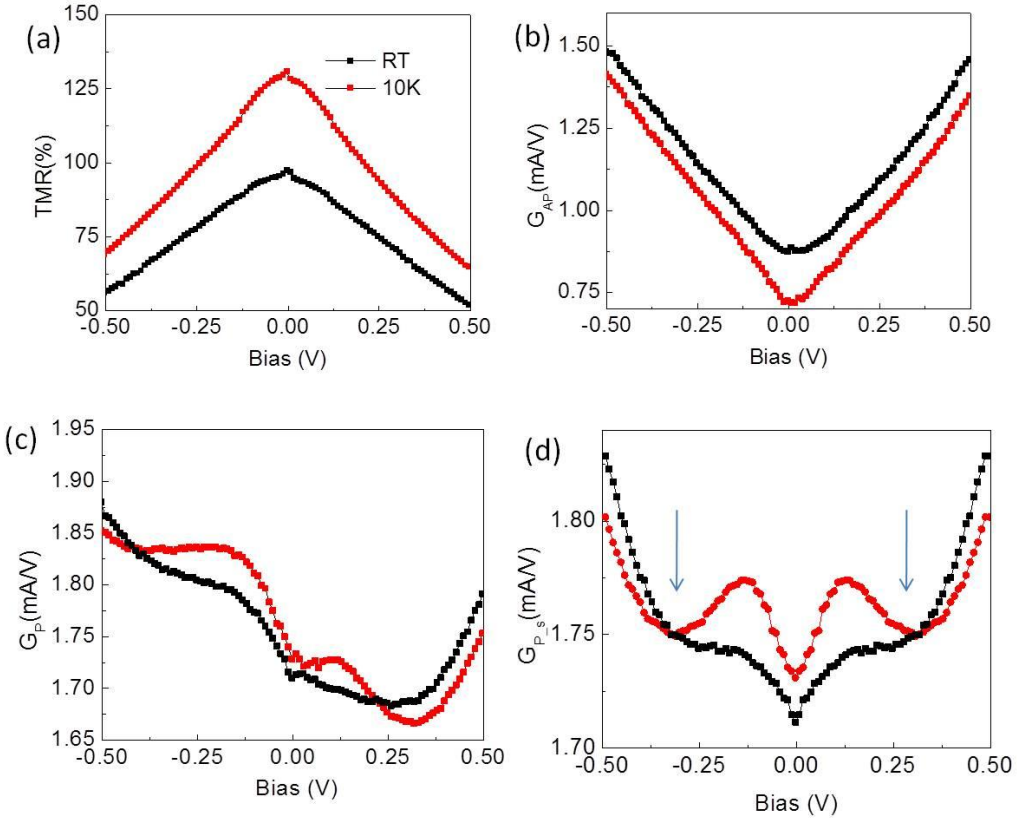

Figure 4-23. Bias dependence of conductance at RT and 10K (a) TMR differential conductance in (b) AP and (c) P magnetic configuration at RT and 10K. (d) Plot of the G_{PS} versus bias voltage. Here, $G_{PS}(V)$ is a symmetric part of $G_P(V)$ and $G_{PS}(V)=(G_P(V)+G_P(-V))/2$.

The fact that these local minimums are temperature independent, indicates that they are not related to the magnon absorption.

Figure 4-23(b) shows the plot of the G_{AP} as a function of the bias at RT and 10K. Compared to the P configuration 4-23(c), G_{AP} has a stronger bias dependence due to the inelastic tunneling channels. While the G_P varies little, zero bias

conductance in AP state decreases 15% from RT to 10K since the magnon absorption channels are frozen out during the cooling. It can be seen that G_{AP} raises more rapidly with bias at 10K than that at RT in low bias region (~0.15V) due to the magnon emission [6]. Considering the bias dependence of conductance is dominated by AP channels, a stronger bias dependent TMR can be expected at low temperature in low bias region (see Figure 4-23(a)).

4.7.2 Temperature dependent spin transfer torques

I made ST-FMR measurements on one device at 10K and show the results in Figure 4-24. Here I assume that I_{RF} does not change with temperature. A major finding is that overall the amplitude of the in-plane torkance is reduced at low temperature in comparison to its value at 300 K. However, the asymmetry (the local maximum in negative bias region) remains. For the field-like torkance, it has a roughly linear bias dependence at low temperature, whereas at RT it can be divided into two regions: in low bias region ($|V|<0.2V$) it varies linearly with bias while in the higher bias region, it is close to constant. Since the magnon-electron interaction plays a significant role in temperature dependence of MR, I suspect that the changes I observed here also can be attributed to magnon absorption, indicating that magnons assist both the in-plane torkance and the field-like torkance. Theoretical studies predicted a quadratic function [54] of the field-like STT on bias voltage in a symmetric MTJ, thus there is a linear bias dependence of the field-like torkance, in accord with our data at 10K. In the case of finite temperature, the contribution from the magnon needs to be considered too. Manchon et al. [47] predicts that the bias dependent STTs are different at the low and

high bias region defined by maximum magnon energy E_m, which is about 0.2V for FeCoB electrodes from the d^2I/dV^2 spectra [40], which may be the reason for the non-linear bias dependence of the field-like torkance at RT.

Figure 4-24 (a) and (b) show the STTs as a function of bias. Both the in-plane and the field-like component are smaller at 10K compared to RT. For the sample shown here, the amplitude of the in-plane torque (the field-like torque) is reduced to 82% (89%) under -0.4V and 71% (73%) under 0.4V. Since STT is sensitive to the nano-scale interface property, I found that the above values varied somewhat from sample to sample, but qualitatively I found that the spin transfer torkance is consistently weaker in all the devices I measured at low temperature. This is consistent with the theoretical prediction: the interfacial electron-magnon interaction at finite temperature gives rise to a positive contribution to the spin-transfer torque [47]. Since the effect of magnon absorption is removed by cooling, the contribution from the intrinsic properties (DOS of electrodes) is emphasized, resulting in more asymmetric behavior in the bias dependent in-plane torque at 10K. Thermal smearing of the tunneling electron's energy may also affect the MR or STT. However, the prediction on temperature dependences of the spin transfer torque calculated with the Keldysh non-equilibrium Green's function method [46] suggests that there is only a very weak temperature dependence for the in-plane torque and that this variation depends significantly on the bias voltage, which is not the case for our data. Moreover, in our devices, R_P is almost constant between 10K and 300K for our thin barrier devices, indicating the thermal smearing of electron's energy is negligible.

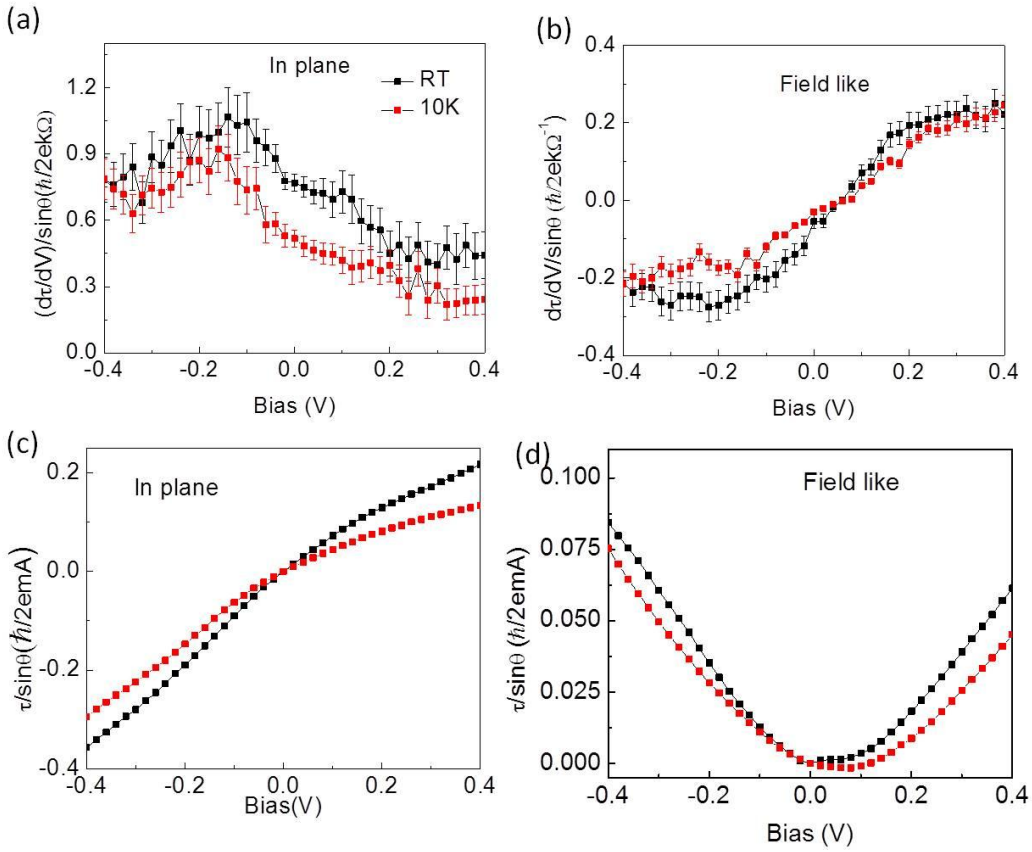

Figure 4-24. Bias dependence of STTs measured at RT and 10K. (a) The in-plane torkance and (b) the field-like torkance measured as a function of bias at room temperature and 10K. Both the in-plane torkance and the field-like torkance are weaker in the low temperature. (c-d) In-plane and perpendicular components of the spin-transfer torque as a function of bias, determined by integrating the data in (a) and (b)**,** here I assume the torques at zero bias are zero, which may not true for the field-like torque.

The temperature dependent in-plane torkance and field-like torkance at -0.4V, -0.2V, 0V, 0.2V, 0.4V respectively are plotted in the Figure 4-25(a-b). The results show that a major drop of the torkance occurs between 100K and 200K. Meanwhile, I

find that the coercivity of the H-R loop also has a stronger temperature dependence in the same region (See Figure 5-8(b)). Further studies are needed to get a good understanding of this interesting correlation.

4.7.3 Temperature dependence of interlay exchange coupling

The temperature dependence of H_{shift} is plotted in the Figure 4-25(d). Here, H_{shift} is the shift field, defined by the middle point of the minor loop, owing to the orange-peel coupling [50] as well as the interlayer exchange coupling (IEC) [19]. At room temperature, the orange-peel coupling seems to be dominant over IEC because IEC generates a negative H_{shift} for a tunneling barrier thickness about 1nm ([51]), whereas the observed H_{shift} is positive. However, this term changes sign when the device is cooled down from 10 Oe to -20 Oe. The orange peel coupling effect as the origin of the sign change H_{shift} can be excluded since roughness of Fe/MgO interfaces should be temperature independent, thus this dipole field shifting can be attributed to the stronger IEC at lower temperature. A similar trend is observed in the temperature dependence of zero bias field-like torkance.

In this section, I have studied the spin-torque excited ST-FMR and TMR properties of FeCoB/MgO/FeCoB MTJs as a function of temperature from 300K to 10K. I find that while the TMR increases by ~ 50% upon cooling to 10 K, the in-plane spin torque and the field-like torque both decrease substantially. The results demonstrate that while magnon-assisted tunneling degrades TMR, it acts to

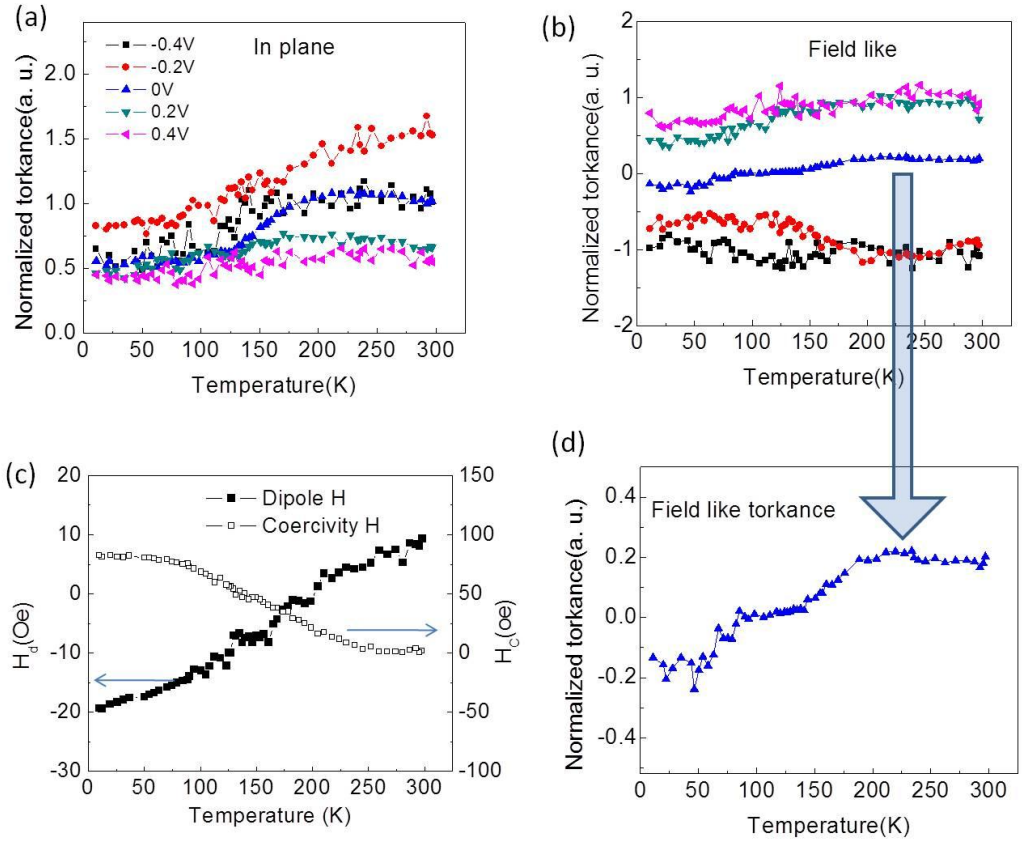

Figure 4-25. Temperature dependence of torkance measured at various voltages. (a) in-plane torkance and (b) field-like torkance at -0.4V, -0.2V, 0.005V, 0.2V, 0.4V respectively. (c) Temperature dependence of H_{shift} and H_c. The plots indicate stronger interlayer exchange coupling at low temperature. (d) The zoomed out plot of temperature dependence of the field-like torque at zero bias in (b).

significantly enhance ST in MTJs, in accord with theoretical prediction. Moreover, the bias-dependent structure in both the asymmetry of the in-plane ST and the parallel conductance of the MTJ remains at low temperature, indicating that the analysis I used in the previous sections is valid for both RT and low temperature.

4.8 Conclusion

In conclusion, I have observed that the symmetry of the bias dependence of TMR, conductance, as well as the STT is strongly affected by annealing in the CoFeB/MgO/CoFeB MTJ system. Especially for the STT, annealing enhances asymmetry of the bias dependent in-plane torque and increases the magnitude of the field-like torque. Based on the adjusted torkance model, I strongly suspect that the former is probably due to the interfacial DOS of the electrode, while the latter effect is related to changes in the interlayer exchange coupling. Both of these factors are very sensitive to the detailed property and quslity of the interface between the ferromagnetic layer and the insulating tunnel barrier. Therefore, to optimize the symmetry of the switching voltage and consequently lower the write margin, properly engineering the interfaces, especially reducing the density of interfacial states, will be very important.

BIBLIOGRAPHY

1. Parkin, S. S. P., Kaiser, C., Panchula, A., Rice, P. M., Hughes, B., Samant, M., & Yang, S.-H. Giant tunneling magnetoresistance at room temperature with MgO (100). tunnel barriers. *Nature materials*, 3, 862 (2004).

2. Zhu, W., Li, H., Chen, Y., & Wang, X. Current Switching in MgO-Based Magnetic Tunneling Junctions. *IEEE Transactions on Magnetics*, 47, 156 (2011).

3. Deac, A. M., Fukushima, A., Kubota, H., Maehara, H., Suzuki, Y., Yuasa, S., Nagamine, Y., et al. Bias-driven high-power microwave emission from MgO-based tunnel magnetoresistance devices. *Nature Physics*, 4, 803 (2008).

4. Jung, M. H., Park, S., You, C.-Y., & Yuasa, S. Bias dependences of in-plane and out-of-plane spin-transfer torques in symmetric MgO-based magnetic tunnel junctions. *Physical Review B*, 8, 134419 (2010).

5. Kubota, H., Fukushima, A., Yakushiji, K., Nagahama, T., Yuasa, S., Ando, K., Maehara, H., et al. Quantitative measurement of voltage dependence of spin-transfer torque in MgO-based magnetic tunnel junctions. *Nature Physics*, 4, 37 (2008).

6. Chen, E., Apalkov, D., Diao, Z., Driskill-Smith, a., Druist, D., Lottis, D., Nikitin, V., et al. Advances and Future Prospects of Spin-Transfer Torque Random Access Memory. *IEEE Transactions on Magnetics*, 46, 1873 (2010).

7. Wang, Chen, Cui, Y.-T., Katine, J. a., Buhrman, R. a., & Ralph, D. C. Time-resolved measurement of spin-transfer-driven ferromagnetic resonance and spin torque in magnetic tunnel junctions. *Nature Physics*, 7, 496 (2011).

8. G Miao, G., Park, Y., Moodera, J., Seibt, M., Eilers, G., & Münzenberg, M. Disturbance of Tunneling Coherence by Oxygen Vacancy in Epitaxial Fe/MgO/Fe Magnetic Tunnel Junctions. *Physical Review Letters*, 100, 246803 (2008).

9. Jang, Y., Lee, K., Lee, S., Yoon, S., Cho, B. K., Cho, Y. J., Kim, K. W., et al. Origin of asymmetry of tunneling conductance in CoFeB/MgO/CoFeB tunnel junction. *Journal of Applied Physics*, 105, 07C901 (2009).

10. Mukherjee, S. S., Bai, F., MacMahon, D., Lee, C.-L., Gupta, S. K., & Kurinec, S. K. Crystallization and grain growth behavior of CoFeB and MgO layers in multilayer magnetic tunnel junctions. *Journal of Applied Physics*,106, 033906 (2009).

11. Cha, J. J., Read, J. C., Egelhoff, W. F., Huang, P. Y., Tseng, H. W., Li, Y., Buhrman, R. a., et al. Atomic-scale spectroscopic imaging of CoFeB/Mg–B–O/CoFeB magnetic tunnel junctions. *Applied Physics Letters*, 95, 032506 (2009).

12. Hindmarch, A. T., Dempsey, K. J., Ciudad, D., Negusse, E., Arena, D. A., & Marrows, C. H. Fe diffusion, oxidation, and reduction at the CoFeB/MgO interface studied by soft x-ray absorption spectroscopy and magnetic circular dichroism. *Applied Physics Letters*, 96, 092501 (2010).

13. Rumaiz, A. K., Woicik, J. C., Wang, W. G., Jordan-Sweet, J., Jaffari, G. H., Ni, C., Xiao, J. Q., et al. Effects of annealing on the local structure of Fe and Co in CoFeB/MgO/CoFeB tunnel junctions: An extended x-ray-absorption fine structure study. *Applied Physics Letters*, 96, 112502 (2010).

14. He, H., Zhernenkov, K., Vadalá, M., Akdogan, N., Gorkov, D., Abrudan, R. M., Toperverg, B. P., et al. The effect of annealing on the junction profile of CoFeB/MgO tunnel junctions. *Journal of Applied Physics*, 108, 063922 (2010).

15. Aoki, T., Ando, Y., Watanabe, D., Oogane, M., & Miyazaki, T. Spin transfer switching in the nanosecond regime for CoFeB/MgO/CoFeB ferromagnetic tunnel junctions. *Journal of Applied Physics*, 103, 103911 (2008).

16. Slonczewski, J. C., & Sun, J. Z. Theory of voltage-driven current and torque in magnetic tunnel junctions. *Journal of Magnetism and Magnetic Materials*, 310, 169 (2007).

17. Jang, Y., Nam, C., Lee, K.-S., Cho, B. K., Cho, Y. J., Kim, K.-S., & Kim, K. W. Variation in the properties of the interface in a CoFeB⁄MgO⁄CoFeB tunnel junction during thermal annealing. *Applied Physics Letters*, 91,102104 (2007).

18. K Kubota, H., Fukushima, A., Ootani, Y., Yuasa, S., Ando, K., Maehara, H., Tsunekawa, K., et al. Dependence of spin-transfer switching current on free

layer thickness in Co–Fe–B/MgO/Co–Fe–B magnetic tunnel junctions. *Applied Physics Letters*, 89,032505 (2006).

19. Katayama, T., Yuasa, S., Velev, J., Zhuravlev, M. Y., & Jaswal, Interlayer exchange coupling in Fe / MgO / Fe magnetic tunnel junctions, *Applied Physics Letters* 89,112503 (2006).

20. Oh, S.-C., Park, S.-Y., Manchon, A., Chshiev, M., Han, J.-H., Lee, H.-W., Lee, J.-E., et al. Bias-voltage dependence of perpendicular spin-transfer torque in asymmetric MgO-based magnetic tunnel junctions. *Nature Physics*, 5, 898 (2009).

21. Li, Z., & Zhang, S. Thermally assisted magnetization reversal in the presence of a spin-transfer torque. *Physical Review B*, 69, 134416 (2004).

22. Sankey, J. C., Cui, Y.-T., Sun, J. Z., Slonczewski, J. C., Buhrman, R. a., & Ralph, D. C. Measurement of the spin-transfer-torque vector in magnetic tunnel junctions. *Nature Physics*, 4, 67 (2008).

23. Wang, C., Cui, Y.-T., Sun, J., Katine, J., Buhrman, R., & Ralph, D. Bias and angular dependence of spin-transfer torque in magnetic tunnel junctions. *Physical Review B*, 79,224416 (2009).

24. Butler, W., Zhang, X.-G., Schulthess, T., & MacLaren, J. Spin-dependent tunneling conductance of Fe|MgO|Fe sandwiches. *Physical Review B*, 63, 054416 (2001).

25. Belashchenko, K., Velev, J., & Tsymbal, E. Effect of interface states on spin-dependent tunneling in Fe/MgO/Fe tunnel junctions. *Physical Review B*, 72, 140404 (2005).

26. Belashchenko, K., Velev, J., & Tsymbal, E. Effect of interface states on spin-dependent tunneling in Fe/MgO/Fe tunnel junctions. *Physical Review B*, 72, 140404 (2005).

27. Tiusan, C., Bellouard, C., Hehn, M., Jouguelet, E., & Schuhl, A. Interfacial Resonance State Probed by Spin-Polarized Tunneling in Epitaxial Fe/MgO/Fe Tunnel Junctions Pd Energy (eV). Physical *Review Letters*, 93, 106602 (2004).

28. Stroscio J. A., Pierce D. T., Davies A. Celotta, Tunneling Spectroscopy of bcc(100). Surface States, *Physical Review Letters*, 75, 2960 (1995).

29. Zermatten, P.-J., Gaudin, G., Maris, G., Miron, M., Schuhl, a., Tiusan, C., Greullet, F., et al. Fe diffusion, oxidation, and reduction at the CoFeB/MgO interface studied by soft x-ray absorption spectroscopy and magnetic circular dichroism. *Physical Review B*, 78, 033301 (2008).

30. Plucinski, L., Zhao, Y., Schneider, C. M., Sinkovic, B., & Vescovo, E. Surface electronic structure of ferromagnetic Fe(001).. *Physical Review B*, 80, 184430 (2009).

31. Tsymbal, E., Belashchenko, K., Velev, J., Jaswal, S., Vanschilfgaarde, M., Oleynik, I., & Stewart, D. Interface effects in spin-dependent tunneling. *Progress in Materials Science*, 52, 401 (2007).

32. Gao, L., Jiang, X., Nicholson, D. M. C., Topuria, T., & Parkin, S. S. P. Role of the electronic structure on the relationship between the crystallinity of CoFe and its tunneling magnetoresistance. *Applied Physics Letters*, 95, 012508 (2009).

33. Gradhand, M., Heiliger, C., Zahn, P., & Mertig, I. Tunneling magnetoresistance with amorphous electrodes. *Physical Review B*, 77, 134403 (2008).

34. Manchon, a, Ryzhanova, N., Vedyayev, a, Chschiev, M., & Dieny, B. Description of current-driven torques in magnetic tunnel junctions. *Journal of Physics: Condensed Matter*, 20, 145208 (2008).

35. Yang, H. X., Chshiev, M., Kalitsov, a., Schuhl, a., & Butler, W. H. Effect of structural relaxation and oxidation conditions on interlayer exchange coupling in Fe|MgO|Fe tunnel junctions. *Applied Physics Letters*, 96, 262509 (2010).

36. Koller, P. H. P., Swagten, H. J. M., De Jonge, W. J. M., Boeve, H., & Coehoorn, R. Direct observation of the barrier asymmetry in magnetic tunnel junctions. *Applied Physics Letters*, 84, 4929 (2004).

37. Brückl, H., Schmalhorst, J., Reiss, G., Gieres, G., & Wecker, J. Evolution of barrier asymmetry in magnetic tunnel junctions. *Applied Physics Letters*, 78, 1113 (2001).

38. Liu, Y., Chiaramonti, A. N., Schreiber, D. K., Yang, H., Parkin, S. S. P., Heinonen, O. G., & Petford-Long, A. K. Effect of annealing and applied bias on barrier shape in CoFe/MgO/CoFe tunnel junctions. *Physical Review B*, 83, 165413 (2011).

39. WeiH-X., Qin, Q.-H., Ma, Q.-L., Zhang, X.-G., & Han, X.-F. Inelastic electron tunneling spectrum from surf ace magnon and magnetic impurity scatterings in magnetic tunnel junctions. *Physical Review B*, 82, 134436(2010).

40. Bang, D., Nozaki, T., Djayaprawira, D. D., Shiraishi, M., Suzuki, Y., Fukushima, a., Kubota, H., et al. Inelastic tunneling spectra of MgO barrier magnetic tunneling junctions showing large magnon contribution. *Journal of Applied Physics*, 105, 07C924 (2009).

41. Drewello, V., Schäfers, M., Schebaum, O., Khan, A., Münchenberger, J., Schmalhorst, J., Reiss, G., et al. Inelastic electron tunneling spectra of MgO-based magnetic tunnel junctions with different electrode designs. *Physical Review B*, 79, 174417 (2009).

42. Wang, S., Ward, R., Du, G., Han, X., Wang, C., & Kohn, A. Temperature dependence of giant tunnel magnetoresistance in epitaxial Fe/MgO/Fe magnetic tunnel junctions. *Physical Review B*, 78, 180411 (2008).

43. Chao, C.-T., Chen, C.-C., Kuo, C.-Y., Wu, C.-S., Horng, L., Isogami, S., Tsunoda, M., et al. Temperature Dependence of Electrical Transport and Magnetization Reversal in Magnetic Tunnel Junction. *IEEE Transactions on Magnetics*, 46, 2195(2010).

44. Zeng, Z. M., Wang, Y., Han, X. F., Zhan, W. S., & Zhang, Z. Bias voltage and temperature dependence of magneto-electric properties in double-barrier magnetic tunnel junction with amorphous Co-Fe-B electrodes. *The European Physical Journal B*, 52, 205 (2006).

45. Wang, W., Liu, E., Kodzuka, M., Sukegawa, H., Wojcik, M., Jedryka, E., Wu, G. H., et al. Coherent tunneling and giant tunneling magnetoresistance in

CoFeAl/MgO/CoFe magnetic tunneling junctions. *Physical Review B*, 81, 140402 (2010).

46. You, C.-Y., Song, S.-H., & Kim, H. Temperature dependences of the spin transfer torque and tunneling magneto-resistance in magnetic metallic and tunneling junctions. *Applied Physics Letters*, 99,092504 (2011).

47. Manchon, A., & Zhang, S. Influence of interfacial magnons on spin transfer torque in magnetic tunnel junctions. *Physical Review B*, 79, 174401 (2009).

48. Zhang, S., Levy, P., Marley, a., & Parkin, S. Quenching of Magnetoresistance by Hot Electrons in Magnetic Tunnel Junctions. *Physical Review Letters*, 79, 3744 (1997).

49. Drewello, V., Schmalhorst, J., Thomas, a., & Reiss, G. Evidence for strong magnon contribution to the TMR temperature dependence in MgO based tunnel junctions. *Physical Review B*, 77, 014440 (2008).

50. Schrag, B. D., Anguelouch, A., Ingvarsson, S., Xiao, G., Lu, Y., Trouilloud, P. L., Gupta, A., et al. Neel orange-peel coupling in magnetic tunneling junction devices. Applied Physics Letters 77, 2373 (2000).

51. Faure-Vincent, J., Tiusan, C., Bellouard, C., Popova, E., Hehn, M., Montaigne, F., & Schuhl, A. Interlayer Magnetic Coupling Interactions of Two Ferromagnetic Layers by Spin Polarized Tunneling. *Physical Review Letters*, 89, 107206 (2002).

52. Georges, B., Grollier, J., Cros, V., Fert, a., Fukushima, a., Kubota, H., Yakushijin, K., et al. Origin of the spectral linewidth in nonlinear spin-transfer oscillators based on MgO tunnel junctions. *Physical Review B*, 80, 060404 (2009).

53. Ma, Q. L., Wang, S. G., Wei, H. X., Liu, H. F., Zhang, X.-G., & Han, X. F. Evidence for magnon excitation contribution to the magnetoresistance behavior during thermal annealing in CoFeB/MgO/CoFeB magnetic tunnel junctions. *Physical Review B.* 83, 224430 (2011).

54. Slonczewski, J. C. Currents, torques, and polarization factors in magnetic tunnel junctions. *Physical Review B*, 71, 024411 (2005).

55. Theodonis, I., Kioussis, N., Kalitsov, A., Chshiev, M., & Butler, W. Anomalous Bias Dependence of Spin Torque in Magnetic Tunnel Junctions. *Physical Review Letters*, 97, 237205 (2006).

CHAPTER 5

SPIN-HALL AND SPIN-PUMPING EFFECTS OBSERVED IN W/FECOB THIN FILMS

The spin-Hall effect (SHE) and its reciprocal, the inverse spin-Hall effect (ISHE), are of great importance in spintronics since they enable, respectively, the conversion of a longitudinal charge current to a transverse spin current and the reverse process. Here I report on a ferromagnetic resonance (FMR) study of FeCoB/W thin film bi-layer structures that incorporate different W thicknesses and hence difference phases. A very large negative spin Hall angle has been observed in the β-W samples and confirmed by spin-torque switching studies. Alternatively FMR measurements with bi-layers containing α-W suggests a strong positive SHE, but this interpretation of the experiment is not consistent with spin torque switching studies utilizing α-W. Since the α-W FMR result show a greatly enhanced magnetic damping coefficient for the $Fe_{40}Co_{40}B_{20}$ layer we tentatively attribute these results to a significantly enhanced spin pumping effect in α-W, relative to that in β-W. Magnetization measurements indicate that the two different types of $Fe_{40}Co_{40}B_{20}$/W bilayers also have substantially different interfacial magnetic anisotropy coefficients.

5.1 Background

The spin Hall effect has been a very active focus of study over the past few years due to its potential for application in memory and logic devices [1-2]. This effect occurs when an unpolarized longitudinal charge current flows through a material with

a strong spin-orbit interaction, leading to a transverse spin current where "up" spins accumulate on one edge of the sample and "down" spins accumulate on the other (Figure 5-1(c)). Although the spin Hall effect was predicted over three decades ago [3], it did not receive much attention until a large spin Hall effect in strongly spin-orbit coupled materials was predicted and observed experimentally[4-5]. Recent studies have demonstrated that the magnitudes of the spin Hall angles in the 5d elements Pt and high resistivity Ta and W can be relatively large, e.g. $\theta_{SH}^{\beta-W} \approx -0.30$ [6], generating the spin current efficiently enough to be of interest for magnetization manipulation via the spin transfer torque mechanism. However, the largest spin Hall angle our group measured is in the β phase W thin film with resistivity ~200 μΩ·cm, while the α phase W, which would be preferred in memory applications since its resistivity is much lower ~20 μΩ·cm and thus would require less power for switching, is not an efficient spin Hall materials. In this chapter, I will present my results of ST-FMR measurements on α-W and β-W, and discuss the possible mechanism behind their different behavior.

5.2 The spin Hall effect and the spin pumping effect

The W films studied here were produced by dc-magnetron sputtering onto oxidized Si substrates. Previous work has shown that unlike Ta, the resistivity of sputtered W films has strong thickness (d) dependence [6]. For example, 4nm W films exhibit a high resistivity, which is a signature of the β-W phase and previously determined to have the A15 crystal structure associated with very strong electron-phonon scattering [7]. But when thickness $d \geq 10nm$, the films are typically purely α-

W phase with a bcc crystal structure. For thickness between 5 to 9 nm, our W films tend to be of a mixed α and β composition with, and thus the resistivity greatly depends on the W thickness (See Figure 5-2(a)). This result is consistent with our X-ray diffraction (XRD) measurement.

I determined the spin Hall angle of β-W first by performing ST-FMR measurements on patterned micron-sized substrate/$Co_{40}Fe_{40}B_{20}$ 5nm/ W d nm bi-layer structures. Figure 5-1(a-b) shows the ST-FMR signals measured on the device with d=4 (β-phase W) and d=20 (α-phase W). As expected, the resonance peak shapes can be very well fit by the sum of symmetric (S) and antisymmetric (A) Lorentzian curves with the same line-width for a given frequency (fits are shown as lines in Figure 5-1(a-b)). From the fitting, it is found that the symmetric peak changes its sign when the W thin film goes thicker. If spin pumping and ISHE is negligible, S and A components can be expressed as following [8]

$$S = \hbar J_{S,rf} /(2e\mu_0 M_s t) \tag{5-1}$$

$$A = H_{rf}[1+(4\pi M_{eff} / H_{ext})]^{1/2} \tag{5-2}$$

Here $J_{S,rf}\hbar/2e$ represents the oscillating spin current density injected into FeCoB, μ_0 is the permeability in vacuum, M_s is the saturation magnetization of FeCoB, t is the thickness of the FeCoB layer, H_{rf} is the Oersted field generated by the rf current, M_{eff} is the demagnetization field and H_{ext} is applied in the film plane.

Since S is proportional to $J_{S,rf}$ and A is proportional to H_{rf} , the different results suggest that the contribution from the spin current is different between our α-W and β-W devices. If I assume the spin Hall angle

$$\theta_{SH} = \frac{J_{S,rf}}{J_{C,rf}} = \frac{S}{A}\frac{e\mu_0 M_S td}{\hbar}[1+(4\pi M_{eff}/H_{ext})]^{1/2} \quad (5\text{-}3)$$

I get $\theta_{SH}^{\beta-W} = -0.35$ and $\theta_{SH}^{\alpha-W} = 1.08$ respectively. The first term agrees with the result from the switching data, but the latter, huge positive spin Hall effect is not supported by current switching experiments in our three terminal devices. Instead from those experiments, the spin Hall angle is $\theta_{SH}^{\alpha-W} \leq 0.07$ [6].

In the above analysis, I only consider the spin Hall effect. An additional contribution to the dc voltage can arise from spin pumping in combination with the inverse spin Hall effect in the spin Hall material layer, as observed in Ref. [9-10]. In that case, spin current leads to a damping of the ferromagnetic precession, resulting in a faster alignment of the magnetization with the effective applied magnetic field H_{eff}, and the pumped spins are absorbed by the attached reservoirs (See Figure 5-1(d)). Since spin-flip scattering is an important fact of life in magneto-electronics, the spin current due to the spin pumping effect can be expressed as

$$I_S = I_S^{pump} - I_s^{back} \quad (5\text{-}4)$$

which vanishes in the absence of spin-flip scattering. Here I_S^{pump} is the spin pumping current and I_s^{back} is the spin-accumulation-driven current back into the ferromagnet. [11].

5.3 Effective spin mixing conductance

Considering both the spin Hall effect and the spin pumping effect, Leao in our group did the calculation and modified the expression of the measured spin Hall angle. Assuming $H_{ext} << 4\pi M_{eff}$, the modified spin Hall angle would be:

$$\theta'_{SH} = \frac{eM_S td}{\mathsf{h}}[1+(4\pi M_{eff} / H_{ext})]^{1/2}\left(\frac{S}{A}\right) = \theta_{SH} + \theta_{SP} \tag{5-5}$$

Here d is the thickness of the normal metal, θ_{SH} is the true spin Hall angle (contribution from spin Hall effect) and θ_{SP} is the spin pump angle (contribution from spin pump effect) with the correlation as

$$\theta_{SP} = -\theta_{SH}\Gamma \tag{5-6}$$

Γ is a coefficient that indicates how strong the spin pumping effect is in comparison to the spin Hall effect, and is determined by

$$\begin{aligned}\Gamma = \frac{CeM_S tdH_{ext}}{\hbar}\frac{e\gamma}{16\pi}\lambda_{NM}\left(\frac{\rho_{FM}}{\Delta\rho}\right)\left(\frac{\sigma_{NM}d}{\sigma_{NM}d+\sigma_{FM}t}\right) \\ \times\tanh\left(\frac{d}{2\lambda_{NM}}\right)g_{eff}^{\uparrow\downarrow}\left(\frac{1+(4\pi M_{eff}/H_{ext})}{(1/\gamma)\Delta H(\partial\omega/\partial H)}\right)_R\end{aligned} \tag{5-7}$$

Here ρ_{FM} is the density of ferromagnetic layer and σ_{NM} and σ_{FM} are the conductivities of the normal metal and the ferromagnetic layer, respectively. λ_{NM} is the spin diffusion length in the normal layer, $g_{eff}^{\uparrow\downarrow}$ is the effective spin mixing conductance of the ferromagnet–normal metal interface, ω is the frequency of the rf current, *C* is a constant and ΔH is the resonance line-width.

From the above equations, it can be seen that θ_{SP} has the opposite sign of θ_{SH} and its value is determined by several parameters, such as thickness of the normal layer, thickness of the ferromagnetic layer and the effective interfacial spin mixing conductance. Clearly, θ_{SP} is larger when d goes up. When the spin pumping effect is strong enough, then the sign of θ'_{SH} will be decided by θ_{SP} , thus a positive S/A ratio can be expected. Figure 5-2(b) shows the W thickness dependence of θ'_{SH} as measured experimentally. The plot suggests that the contribution of the spin pumping effect becomes more important as W become thicker and this effect dominates when d=20nm.

If I assume λ_{NM} is similar in β-W and α-W, then in the equation 5-7, the W thickness dependent terms are as following:

$$\Gamma_d = d\left(\frac{\sigma_{NM} d}{\sigma_{NM} d + \sigma_{FM} t}\right)\tanh\left(\frac{d}{2\lambda_{NM}}\right)\frac{g_{eff}^{\uparrow\downarrow}}{\Delta H} \qquad (5\text{-}8)$$

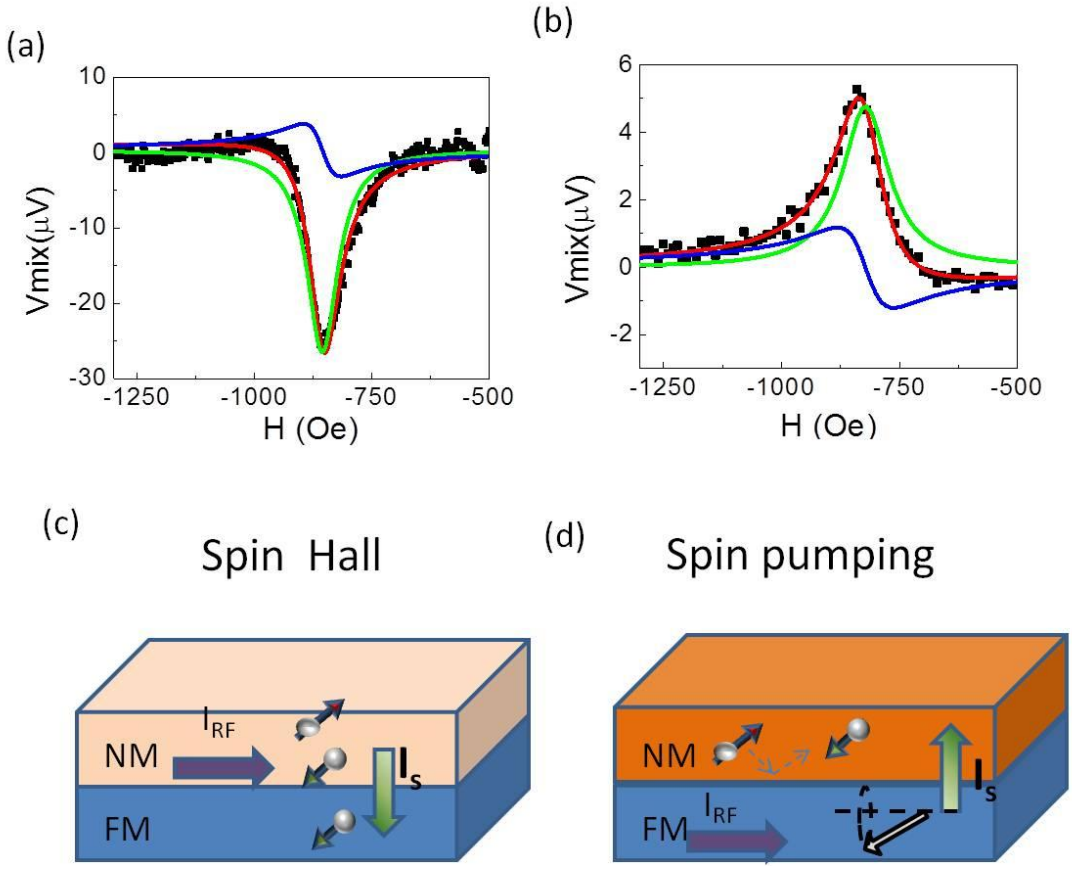

Figure 5-1. FMR spectra and schematic of the spin Hall effect and spin pumping effect. (a-b)FMR spectra measured for (a) $Fe_{40}Co_{40}B_{20}$ 5nm/ W 4nm and (b) $Fe_{40}Co_{40}B_{20}$ 5nm/ W 20nm with fits to the Lorentzian function. (c-d) Schematic of a bilayer thin film illustrating (c) the spin Hall effect and (d) spin pumping effect.

Since λ_{NM} is small, around 1nm in β-W and 2nm in α-W, when $d \geq 4nm$, $\tanh\left(\frac{d}{2\lambda_{NM}}\right) \approx 1$. With the results from the resistivity and ST-FMR measurement, σ_{NM}, σ_{FM} and ΔH can be determined, thus I get:

$$\frac{\Gamma_{d\,20nm}}{\Gamma_{d\,4nm}} \approx 5\frac{g^{\uparrow\downarrow}_{eff\,20nm}}{g^{\uparrow\downarrow}_{eff\,4nm}} \tag{5-9}$$

The effective spin mixing conductance $g^{\uparrow\downarrow}_{eff}$ can be calculated by measuring the frequency dependence of line-width [11]

$$\Delta H = \Delta H_0 + \left(\frac{\omega}{\gamma}\right)\left(\frac{g_L \mu_B}{4\pi M_S t} g^{\uparrow\downarrow}_{eff} + \alpha_0^{'}\right) \tag{5-10}$$

Here ΔH_0 is the intrinsic line-width and g_L is the coefficient, $\alpha_0^{'}$ is frequency dependent intrinsic damping of ferromagnetic layer. In my experiment, ST-FMR spectra are taken with different ac frequency ω, ΔH is measured for each ω, and thus ΔH_0 can be determined from the intercept. $\alpha_0^{'}$ can be calculated by ferromagnetic layer thickness dependence of line-width data. Since the intrinsic damping of amorphous FeCoB and crystalline FeCo is small (<0.01), I assume that the $\alpha_0^{'}$ is independence of W thickness and the broader line-width in α-W is mainly attributed to the spin pumping effect. The W thickness dependent $g^{\uparrow\downarrow}_{eff}$ are shown in the Figure 5-2 (c-d). From the plots, I can see that the line-width of the ST-FMR signal as well as $g^{\uparrow\downarrow}_{eff}$ go up when the thickness of the tungsten thin film increases, consistent with the above prediction. The measured $g^{\uparrow\downarrow}_{eff}$ ranges from $4\times10^{18} m^{-2}$ to $2\times10^{19} m^{-2}$ as the W thickness varies from 4nm to 20nm and the phase changes from β to α. The latter value is close to the number reported by the previous papers: $(4\pm3)\times10^{19} m^{-2}$ on several spin pumping systems with Ni, Co, Fe, Co_2FeAl, Co_2FeSi, Fe_3O_4, and

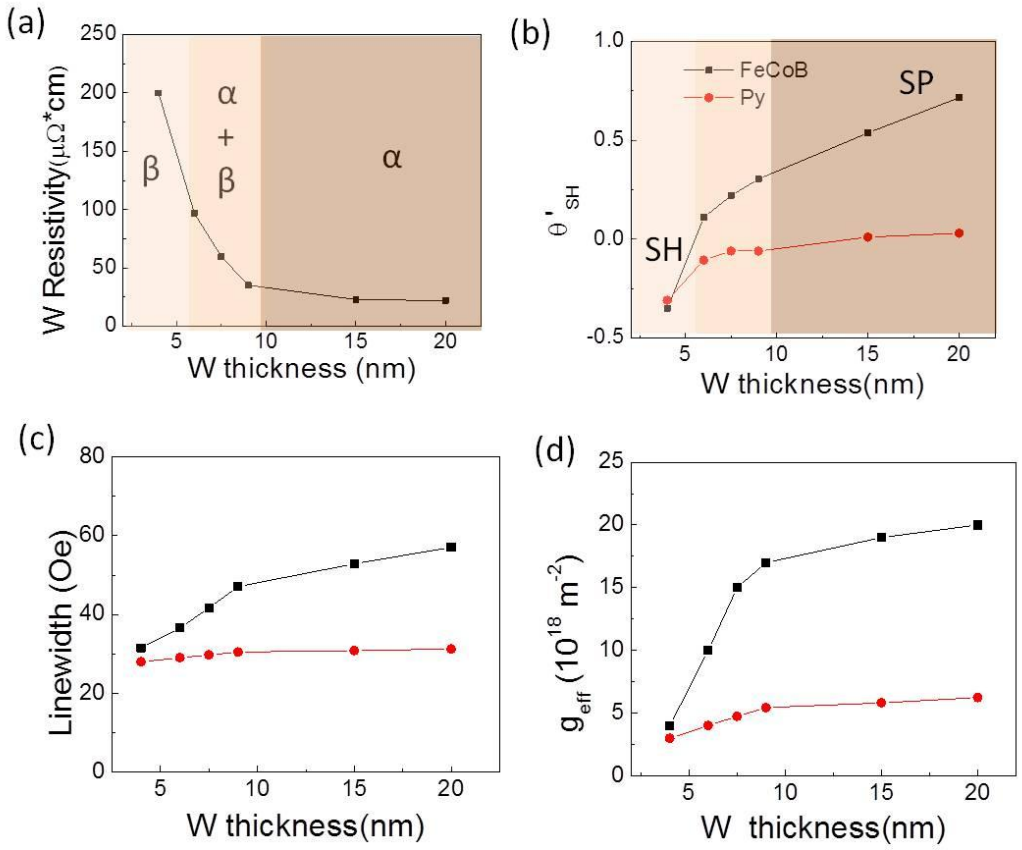

Figure 5-2. Resistivity and spin Hall angle as a function of W thickness. (a) Resistivity of our sputtered W films as a function of thickness. Resistivity variation indicates a phase change of W from β phase to α phase when the tungsten thin film gets thicker. (b) The measured spin Hall angle as a function of W thickness. (c-d) W thickness dependence of (c) line-width and (d) effective spin mixing conductance.

(Ga,Mn)As on the Pt [13] and $2.58\times10^{19}m^{-2}$ on Py/Pt [14], but the former, β-W value is remarkably small for a typical high Z-ferromagnetic interface.

The above calculation gives $g^{\uparrow\downarrow}_{eff\,20nm} / g^{\uparrow\downarrow}_{eff\,4nm} \sim 5$. Using that value in the equation (5-9), I get $\frac{\Gamma_{20nm}}{\Gamma_{4nm}} \approx \frac{\Gamma_{d\,20nm}}{\Gamma_{d\,4nm}} \approx 25$. The coefficient Γ becomes about 25 times larger as the thickness of W changes from 4nm to 20nm.

The above analysis qualitatively explains our plot in the Figure 5-2(b): in the β-phase W, the spin Hall effect plays a significant role and the spin pumping effect is negligible, thus the spin Hall angles calculated by the ST-FMR and current switching data are close to each other. However, in the α-W case, spin pumping effect dominates and the S/A changes its sign.

So far I have assumed that θ_{SH} as well as λ_{NM} are the same for α-W and β-W. This however is a crude approximations and there is no direct evidence to confirm that so far. Considering α-W has a higher conductivity than β-W, it is reasonable to assume λ_{NM} is larger in α-W than in the β-W, and then the $\Gamma_{20nm} / \Gamma_{4nm}$ ratio will be even bigger than the value estimated above. However since $\Gamma_{20nm} / \Gamma_{4nm}$ is independent of θ_{SH}, even if θ_{SH} varies with W phase, the conclusion that the spin pumping effect is stronger in α-W and all the analysis on $g^{\uparrow\downarrow}_{eff}$ are still valid.

This result also shows that effective interfacial spin mixing conductance $g^{\uparrow\downarrow}_{eff}$, one of the most important parameters to value the spin pumping effect, greatly depends on W thickness. The theoretical models for the spin mixing conductance suggest that [11]

$$g_{eff}^{\uparrow\downarrow} = \frac{g^{\uparrow\downarrow}}{1+\left[\sqrt{\varepsilon}\tanh\left(\frac{d}{\lambda_{NM}}\right)\right]^{-1}} \tag{5-11}$$

Here $g^{\uparrow\downarrow}$ is the intrinsic spin mixing conductance and ε is spin-flip to spin-conserving scattering probability, which can be expressed as

$$\varepsilon = \tau_{el} / \tau_{sf} \tag{5-12}$$

τ_{el} is the elastic mean free path relaxation time and τ_{sf} is the spin-flip relaxation time.

As $\varepsilon \to 1$, the material becomes a perfect spin sink. Typically heavier elements with *p* or *d* electrons in the conduction band, such as Pt can be good or nearly perfect spin sinks with $\varepsilon \geq 0.1$[12].

When $\varepsilon \to 0$, it is the low spin-flip case. Usually lighter metals, such as Cu, and heavier metals with only *s* electrons in the conduction band and thus a relatively small spin-orbit coupling, such as Ta typically, corresponded to $\varepsilon \leq 0.01$ [11].

According to the free electron model, τ_{el} is proportional to the conductivity as $\sigma = \frac{ne^2}{m_e}\tau$. If I assume that τ_{sf} is constant in the α-W and β-W, then ε is proportional to the σ. Since the resistivity of the W thin film strongly depends on its crystalline structure, I can expect that in the β-phase W with low conductivity, spin flip rate ε is small, resulting in the weak spin pumping effect. The α-W, on the other hand, has high conductivity and leads to the large effective spin mixing conductance.

$$g_{eff}^{\uparrow\downarrow} \approx \frac{g^{\uparrow\downarrow}}{1+\left[\sqrt{\frac{\sigma m_e}{ne^2\tau_{sf}}}\right]^{-1}} \tag{5-13}$$

Recalling the W thickness dependence of the resistivity (Figure 5-2(a)) $\sigma_{20nm}/\sigma_{4nm} \sim 10$, thus $\varepsilon_\alpha/\varepsilon_\beta \sim 10$ it can be estimated that

$$2 < \frac{1}{1+\left[\sqrt{\varepsilon_\alpha}\right]^{-1}} \Big/ \frac{1}{1+\left[\sqrt{\varepsilon_\beta}\right]^{-1}} < 3.3 \tag{5-14}$$

As I mentioned above $g_{eff\,20nm}^{\uparrow\downarrow}/g_{eff\,4nm}^{\uparrow\downarrow} \sim 5$, which yields $1.5 < g_{20nm}^{\uparrow\downarrow}/g_{4nm}^{\uparrow\downarrow} < 2.5$. Considering that the measured $g_{eff\,20nm}^{\uparrow\downarrow} = 2\times10^{19} m^{-2}$ is a large number, close to the value of the intrinsic mixing conductance of Pt, which is identified as a perfect spin sink, it is reasonable to classify α-W as a good spin sink too, with $\varepsilon_\alpha \geq 0.1$.

Typically in the case $\varepsilon_\alpha \to 1$, the result is $\frac{1}{1+\left[\sqrt{\varepsilon_\alpha}\right]^{-1}} \Big/ \frac{1}{1+\left[\sqrt{\varepsilon_\beta}\right]^{-1}} \approx 2$ and $g_{20nm}^{\uparrow\downarrow}/g_{4nm}^{\uparrow\downarrow} \sim 2.5$ with $0.01 \leq \varepsilon_\beta \leq 0.1$

The reason for the difference of the intrinsic spin mixing conductance between α-W and β-W is not clear yet. The simplest explanation is that it is due to the different band structures of α-W and β-W, since the former has a bcc structure, the same as the typical ferromagnetic layer, while the latter has a very different A-15 structure. Another possibility is that it is the interfacial effect, which is governed by the properties of both the normal layer and the ferromagnetic layer.

5.4 FeCoB thickness dependence of effective spin mixing conductance and in-plane anisotropy

In the previous section, I discuss the W thickness dependence of $g_{eff}^{\uparrow\downarrow}$, here I show that this parameter is also affected by the thickness of the ferromagnetic layer (See Figure 5-3 (a) (c)). The $g_{eff}^{\uparrow\downarrow}$ is almost constant with a small value about $4\times10^{18}m^{-2}$ in β-W, while this number is almost one order of magnitude larger in α-W, and it is governed by the FeCoB thickness: The thicker FeCoB sample is the larger $g_{eff}^{\uparrow\downarrow}$. According to equation (16), this result indicates that intrinsic $g_{\beta}^{\uparrow\downarrow}$ is constant while $g_{\alpha}^{\uparrow\downarrow}$ changes as FeCoB becomes thicker.

Interestingly, VSM measurements show that in the β-W samples, the shape of the M-R loops is independent on the FeCoB thickness with H_c about 5Oe, while in the α-W samples, H_c is determined by the FeCoB thickness and typically larger than the value in the FeCoB/ β-W. Combined with the above spin mixing conductance data, it indicates that $g^{\uparrow\downarrow}$ is correlated with in-plane anisotropy and affected by the phase of the capping layer W.

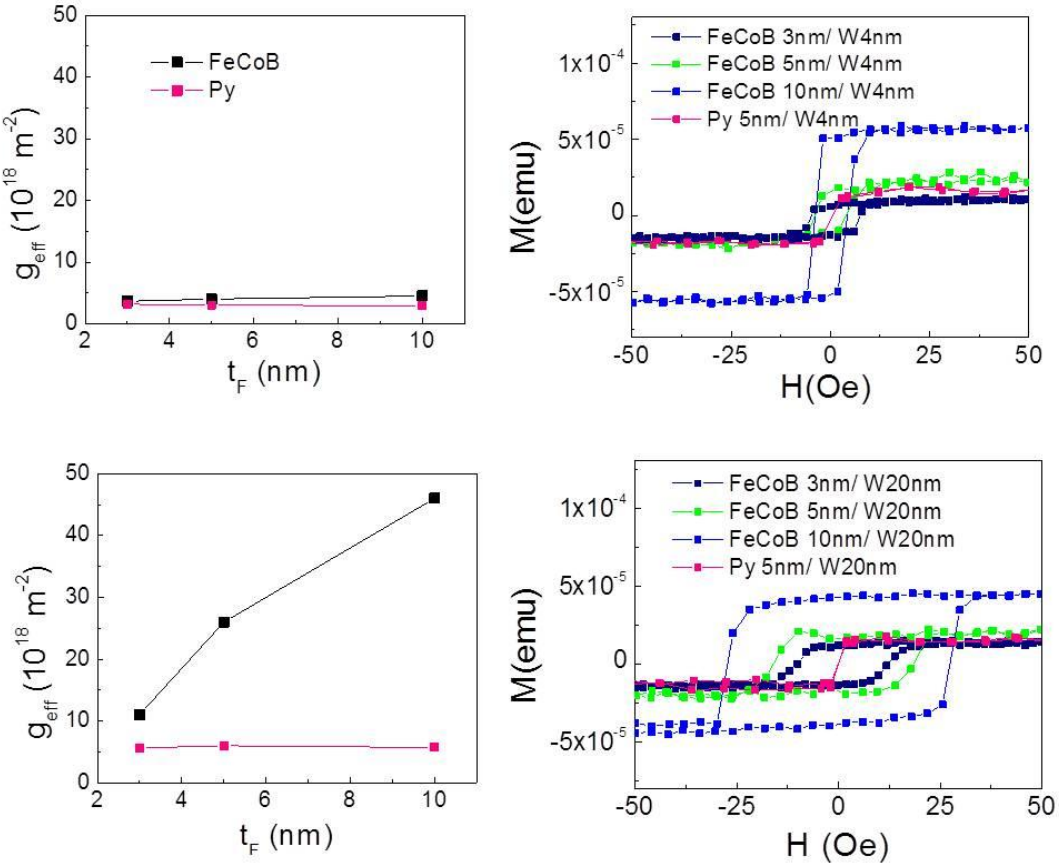

Figure 5-3. Effective spin mixing conductance and coercivity as a function of the FeCoB thickness. (a-b) Effective spin mixing conductance as a function of the FeCoB thickness measured for sample (a) F / β-W and (b) F/ α-W; (c-d) Hysteresis loops of (c) F/ β-W and (d) F/ α-W measured by VSM with the external field in-plane. Here F stands for the ferromagnetic layer: FeCoB (black) or Py (red).

Figure 5-4(a) shows the hysteresis loops of FeCoB/ α-W bi-layer thin film measured by the VSM with different deposition conditions: sputtered without external magnetic field or with the external magnetic field H, 90°, 0° and 45° away from Si (100) direction in-plane. The external field applied during the VSM measurement is

always along the Si (100) direction. It can be seen that the coercivity of the samples is adjustable by the external magnetic field direction during the thin film growth. While the value of M_{eff} does not change in those four samples, the spin mixing conductance is greatly dependent on the growth condition and correlated to the coercivity of the thin films.

The correlation between the spin mixing conductance and in-plane anisotropy is not understood yet. A previous study has shown that in a perpendicular magnetic anisotropy (PMA) system (Co/Pt), the damping coefficient in Co is found to be inversely proportional to the Co layer thickness and that there is linear relation between the PMA and the damping. The authors explain this enhanced damping as the result of *d-d* hybridization at the interface and spin pumping [15]. In our in-plane anisotropy case, further study is needed to understand the change in in-plane anisotropy and spin mixing conductance.

5.5 Control samples

I also studied control samples with the layers Py 5nm/ W 4nm and Py 5nm/ W 20nm, with results as shown in Figure 5-5(c-d). While Py 5nm/ W 4nm gives a negative spin Hall angle as I expected, a Py 5nm/ W 20nm bilayer sample shows a purely antisymmetric signal, indicating that only the Oersted field contribution is present, which is not consistent with the signal of FeCoB 5nm/ W 20nm, where a positive S/A ratio is observed (Figure 5-5 (b)). With the similar calculation as in the

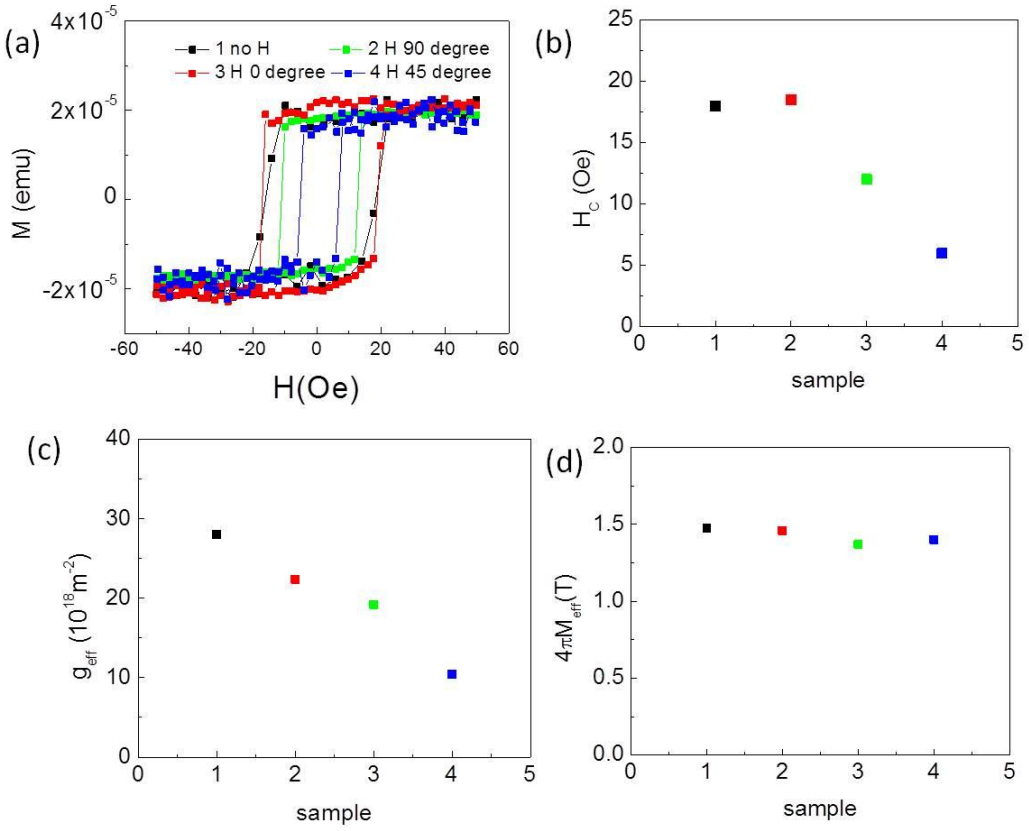

Figure 5-4. Effects of the external field during deposition. (a) Hysteresis loops of FeCoB/ α-W bi-layer thin film with different deposition conditions: sputtered without external magnetic field (black, sample 1) or with the external magnetic field H. In the latter case, the angle between the H and Si (100) direction is 90 ° (red, sample 2), 0 ° (green, sample 3) and 45 ° (blue, sample 4) measured by the VSM. The external field applied during the VSM measurement is always along the Si (100) direction. (b) The coercivity of the above four samples calculated from the Figure (a). (c-d) (c)Line-width and (d) $4\pi M_{eff}$ of those four samples measured by ST-FMR.

previous section, I get in Py/W system $g^{\uparrow\downarrow}_{eff\,4nm} \sim 3\times10^{18} m^{-2}$ and $g^{\uparrow\downarrow}_{eff\,20nm} \sim 6\times10^{18} m^{-2}$, thus $g^{\uparrow\downarrow}_{eff\,20nm} / g^{\uparrow\downarrow}_{eff\,4nm} \sim 2$, $\frac{\Gamma_{20nm}}{\Gamma_{4nm}} \approx 15$, $\theta_{SH} = -0.31$, $\Gamma_{20nm} \sim 1$ and $\Gamma_{4nm} \sim 0.06$. This

result suggest that the spin pumping effect is negligible in Py/β-W, but with the similar magnitude as the spin Hall effect in the Py/α-W. And as 4nm β-W, the value of $g_{eff\_Py}^{\uparrow\downarrow}$ is close to that of $g_{eff\_FeCoB}^{\uparrow\downarrow}$ ($4\times10^{18}m^{-2}$), while for 20nm α-W, $g_{eff\_Py}^{\uparrow\downarrow}$ is much smaller than $g_{eff\_FeCoB}^{\uparrow\downarrow}$ ($2\times10^{19}m^{-2}$).

As I discussed in the FeCoB/W case, the increase of the conductivity due to the W phase change would cause the increase of $g_{eff}^{\uparrow\downarrow}$ by a factor of 2, thus this result may also suggest that the intrinsic $g_{Py/W}^{\uparrow\downarrow}$ is independent of the W thickness. Considering Py is soft ferromagnetic material with $H_c \approx 0$ in all cases, it may be reasonable. The reason for the larger $g^{\uparrow\downarrow}$ in the α-W/FeCoB than α-W/Py is not well understood. One possible explanation might be that there is better lattice matching at the α-W/FeCoB interface than α-W/Py, since α-W is bcc structure and as-grown FeCoB is generally considered to be amorphous but with B out-diffusion or segretation can develop a bbc structure, while permalloy is fcc.

The fact that $g^{\uparrow\downarrow}$ varies in W/FeCoB system but keeps constant in W/Py may also indicate that the change of $g_{FeCoB}^{\uparrow\downarrow}$ is governed by the properties of the interface rather than just the band structure of W itself.

ST-FMR spectra on FeCoB 5nm/ Ta 4nm , FeCoB 5nm/ Ta 20nm, Py 5nm/ Ta 4nm and Py 5nm/ Ta 20nm are plotted out in the Figure 5-6 (a-d). Both FeCoB 5nm/ Ta 4nm and Py 5nm/ Ta 4nm samples give a negative spin Hall angle ~ -0.15, which agrees well with our previous measurement [2]. In FeCoB 5nm/ Ta 20nm and Py

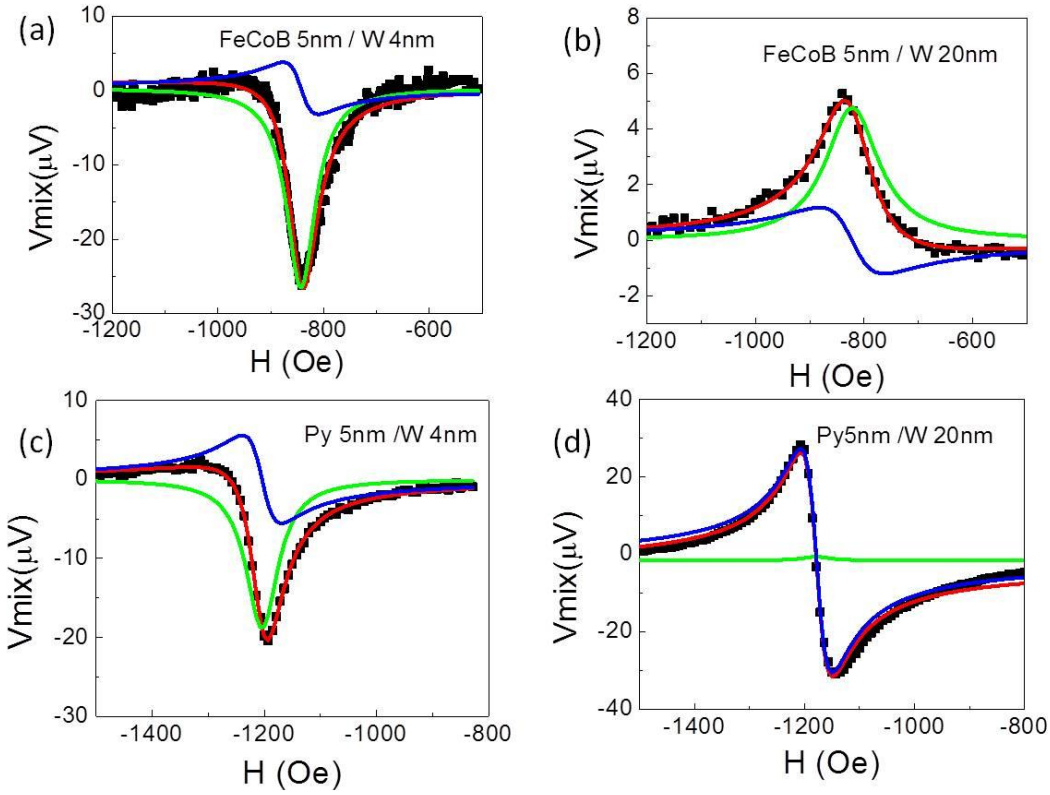

Figure 5-5. FMR spectra of bi-layer structures with FeCoB or Py as ferromagnetic layer. FMR spectra measured for (a) FeCoB 5nm/ W 4nm, (b) FeCoB20 5nm/ W 20nm, (c) Py 5nm/ W 4nm, (d) Py 5nm/ W 20nm. The spectra are similar for the Py and FeCoB with β-W covered but diverse with α-W on the top.

5nm/ Ta 20nm samples, no positive symmetric component of the ST-FMR signal is observed and the measured spin Hall angles ~ -0.10, which gives $\Gamma_{4nm} \sim 0.03$, and also $\Gamma_{20nm} \sim 0.3$in the Ta system. It is reasonable that $\Gamma$is smaller in Ta than W as Ta is a low spin-flip material.

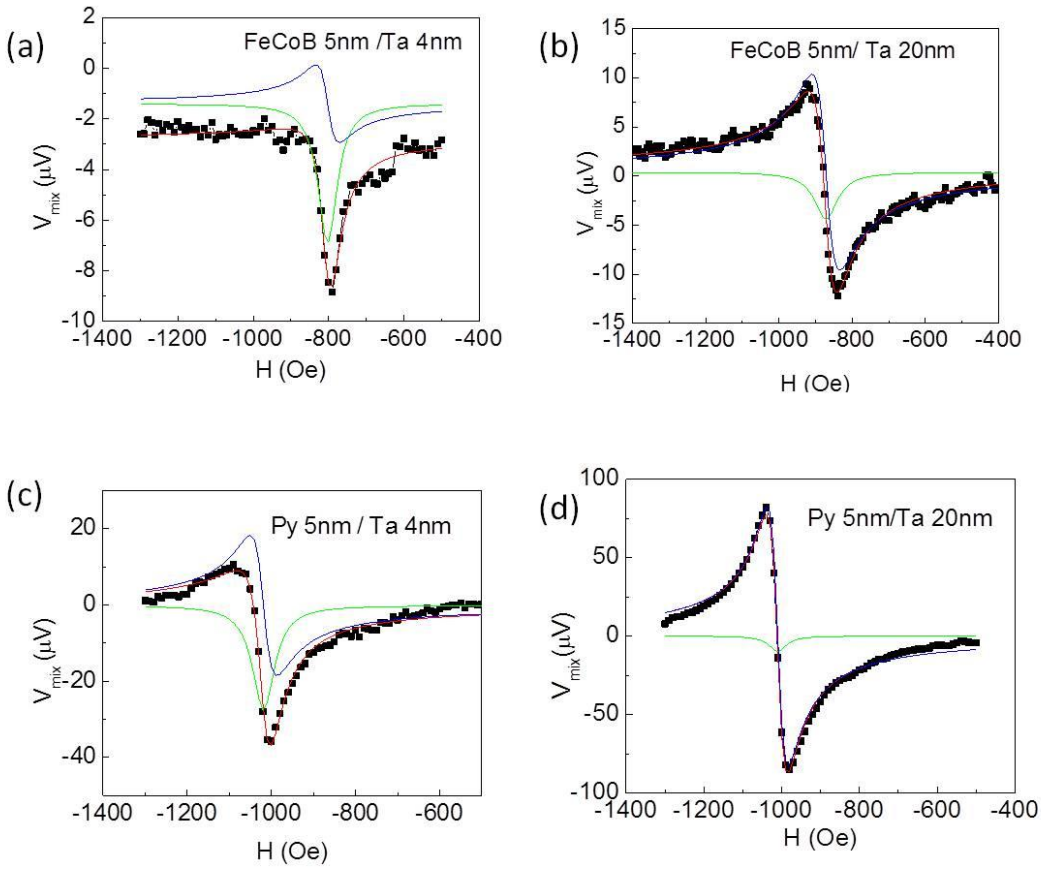

Figure 5-6. FMR spectra on control samples: (a) FeCoB 5nm/ Ta 4nm, (b)FeCoB 5nm/ Ta 20nm , (c) Py 5nm/ Ta 4nm and (d) Py 5nm/ Ta 20nm. No positive symmetric component of signal is observed on those samples.

5.6 Out-of-plane anisotropy

According to the Kittel Formula for in-plane resonance:

$$f = \gamma / 2\pi [H_0 (H_0 + 4\pi M_{eff})]^{1/2} \qquad (5\text{-}14)$$

The effective magnetization can be calculated by a one-parameter fit to the resonance frequencies in ST-FMR spectra, and its value indicates the crystalline anisotropy as following:

$$4\pi M_{eff} = 4\pi M_S - H_K^{\perp} \tag{5-15}$$

Figure 5-7 (a-b) plots out the extracted effective magnetization M_{eff} against film thickness. It can be seen that M_{eff} deceases dramatically when FeCoB is thinner than 4nm in both α-W and β-W cases. Furthermore, it is noticed that M_{eff} is close to zero at around t=1.8 nm, below which the surface anisotropy will overcome demagnetization field and cause the magnetic easy axis to be out-of-plane. This is also confirmed by SQUID measurements with the magnetic field applied out-of plane. Fgure 5-8 (a-d) shows the magnetization as a function of out-of- plane field for as-grown FeCoB 1.5nm / β-W, FeCoB 1.5nm / α-W, β-W/FeCoB 1.5nm/MgO 2nm and α-W/FeCoB 1.5nm/MgO 2nm. It seems that there is a sharp switching in low field region with long tails in high field region in all the samples, which is the indication of an induced partial perpendicular anisotropy. Moreover, the coercivity of the main loop is affected by the adjacent layers: W and MgO.

After annealing α-W/FeCoB 1.5nm/MgO sample, a small field of 50 Oe is required to saturate the magnetization, indicating that the magnetic easy axis is out-of-plane. Our result is consistent with recent reports that PMA is realized when the CoFeB free layer thickness (with a proper capping layer) is reduced to the thin film limit [16]. The origin of the induced perpendicular surface anisotropy is however not

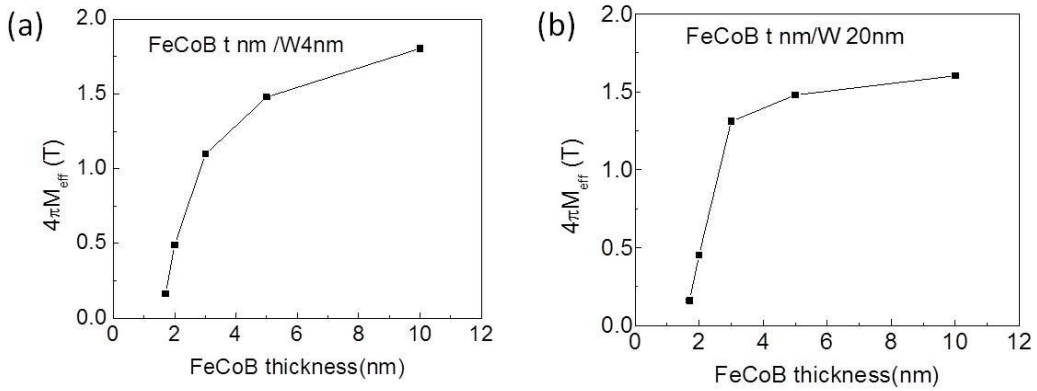

well understood

Figure 5-7. $4\pi M_{eff}$ measured by ST-FMR as a function of the FeCoB thickness with (a) β-W and (b) α-W on top.

but may be related to hybridization of Fe 3d and O 2p orbits at Fe/MgO interface [17]. In most studies, Ta is used as the capping layer and it is found out that Ta/ CoFeB interface also makes a key contribution [28]. However, the critical thickness to observe full perpendicular anisotropy from our sample with a W/FeCoB interface is found to be 1.5nm, which is larger than what is reported in Refs [17] (0.78 nm) with Ta as capping, which indicates W/$Fe_{40}Co_{40}B_{20}$/MgO has relatively larger Ks value than that of Ta/$Fe_{40}Co_{40}B_{20}$/MgO . Moreover, W/CoFeB is probably more thermal stable than Ta /FeCoB. The best annealing temperature for W/FeCoB/MgO with PMA is 350℃, while PMA of Ta/FeCoB/MgO grown in our system is damaged after the heating treatment at the same temperature, which is suspected due to the diffusion of the Ta atoms during the high temperature annealing. Thus α-W/FeCoB/MgO may be

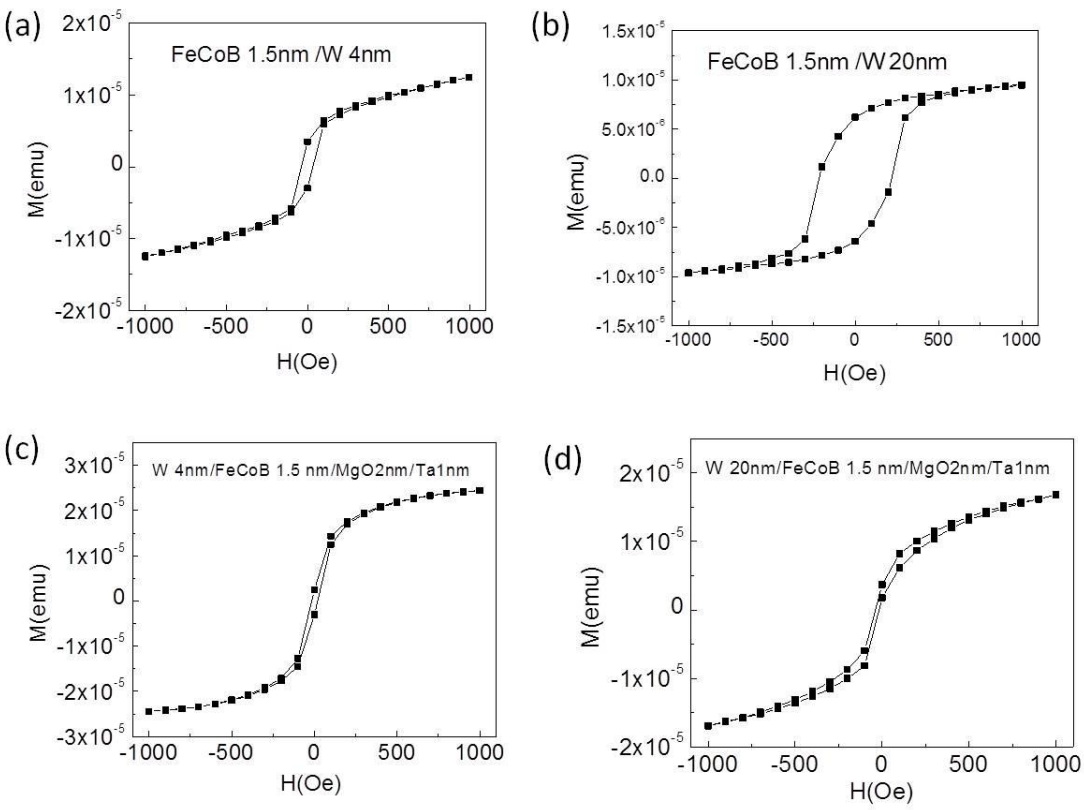

Figure 5-8. Hysteresis loops of as-grown thin films with layer structure: (a) FeCoB 1.5nm / β-W, (b) FeCoB 1.5nm / α-W, (c) β-W/FeCoB 1.5nm/MgO 2nm and (d) α-W/FeCoB 1.5nm/MgO 2nm by SQUID measured with external field perpendicular to the film plane.

an interesting structure, not only for its potential application in the MgO based MTJs with high TMR, but also for its versatility in creating in-plane and out of plane easy axis upon a variation of FeCoB thickness.

The hysteresis loop of the annealed sample β-W/FeCoB 1.5nm/MgO 2nm with the external field perpendicular to the film plane is shown in the Figure 5-9 (b). It seems that the domains with PMA are switched between 200 Oe and -200 Oe, with a

long tail beyond this regime, which suggests that its magnetization is not fully out of plane. The difference of out-plane magnetization between the samples with α-W and β-W may be related to their surface roughness Our AFM data show that the surface RMS roughness for β-W and α-W is 2.12nm and 0.95nm respectively, indicating that surface of the α-W is smoother than the β-W. The surface variation of the β-W due to

the grain boundary is confirmed by the STEM images of the sample with structure of substrate/W 4nm/FeCoB 5nm/Ta 1nm (See Figure 5-9 (f)). The discontinuous surface due to the grain boundary in the β-W needs to be considered especially when the adjacent layer FeCoB is only about 1nm thick when FeCoB is on top.

Figure 5-9 (c) shows the magnetization as a function of in-plane field in the annealed α-W/FeCoB 1.5nm /MgO sample. It is noticeable that in the smaller field regime, the slope of the curve is negative, and the zoom out plot is shown in the Figure 5-9 (e). This anomalous behavior is only shown in the α-W samples. For the β-W, as shown in the Figure 5-9 (d), as expected, M is linearly dependent on the in-plane field, which suggests its hard axis is in-plane. The reason for the strange behavior in the α-W is not clear yet but I suspect it may be related to the Dzyaloshinskii- Moriya interaction (DMI). Previous studies on single crystal W show that the domain orientation is sensitive to the underlying crystal structure rather than to the surface geometry [18]. Typically, the interplay of the DMI and the magnetic anisotropy

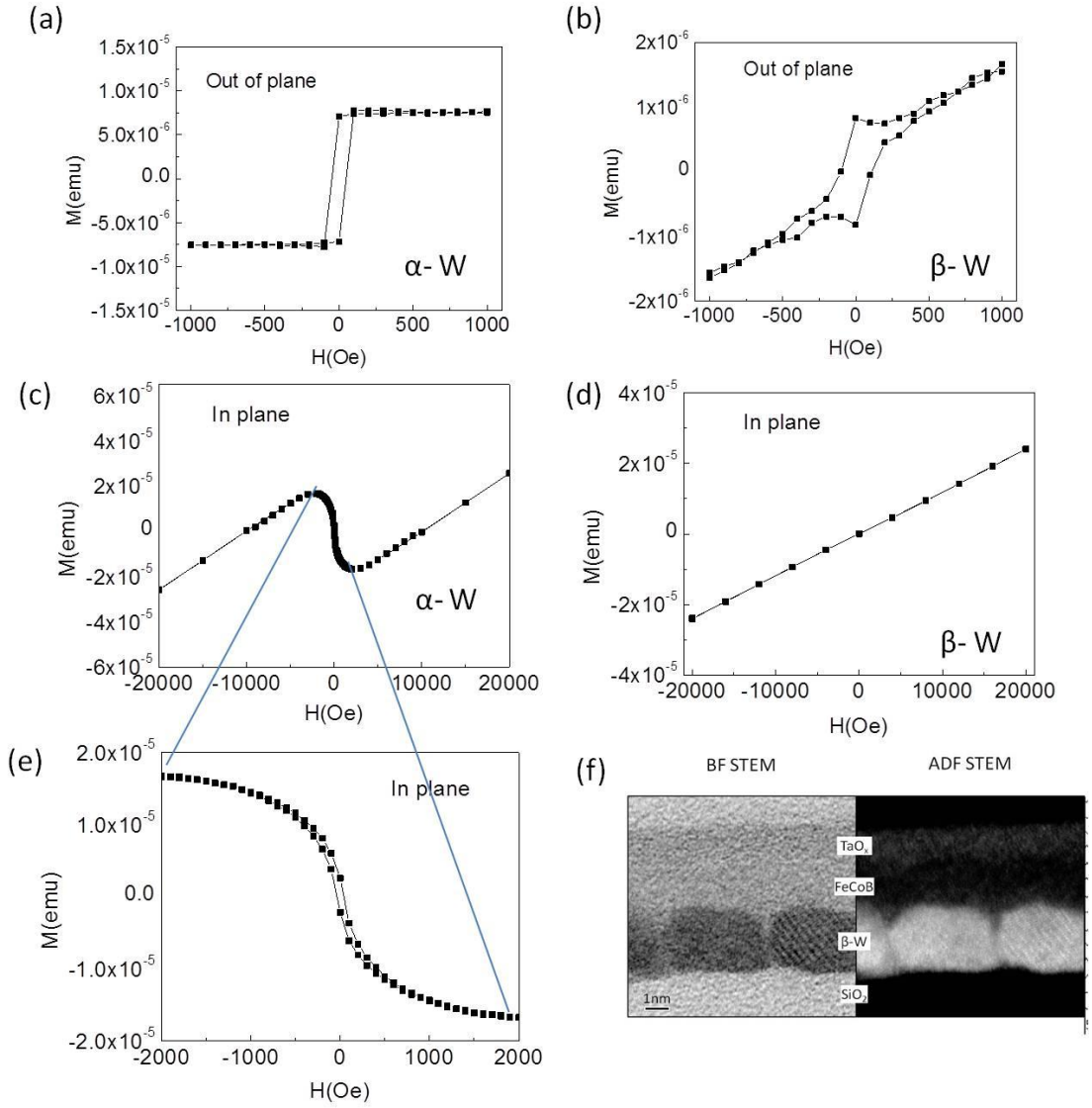

Figure 5-9. Hysteresis loops of the annealed sample with α-W and β-W. (a,c,e) Hysteresis loops of the annealed sample α-W/FeCoB 1.5nm/MgO 2nm by SQUID measured with external field (a) perpendicular to the film plane and (c) in the plane and zoom out in small regime (c). (b,d) Hysteresis loops of the annealed sample β-W/FeCoB 1.5nm/MgO 2nm by SQUID with the magnetic (b) out-plane and (d) in-plane field. Both samples are annealed in the vacuum furnace at 350 ℃ for 1 hour. (f) STEM images of the sample with structure of substrate/W 4nm/FeCoB 5nm/Ta 1nm in the bright and dark field and EELS profile.

determines the preferred orientation of the walls and the stripe domains, respectively, depending on the ferromagnetic layer thickness. For a 2-ML-thick Fe film on bcc W(110), the DMI is sufficiently strong to determine the type and rotational direction of the domain walls on the basis of first-principles calculations in combination with a micro-magnetic model [19]. Experimentally, the domain structure in Fe /W samples with a specific rotational direction that are oriented normal to the (001) direction is detected by spin-polarized scanning tunneling microscopy, which is identified as right-rotating Néel-type walls [20]. Therefore, α-W/FeCoB may be a good system to study the DMI.

5.7 Follow-up experiment: spin injection into Si

In the spin Hall effect, a longitudinal charge current is conversed into a transverse spin current, where "up" spins accumulate on one edge of the sample and "down" spins accumulate on the other. In the above sections, I discussed about the properties of the FeCoB-W interface, but another interesting topic will be how the spins propagate on the other interface, especially the tungsten layer is deposited directly on the Si.

Injection of spin currents into Si is a hot topical since the combination of ferromagnets and semiconductors exploits the unique features that make both of these materials successful [21]. There has been significant progress in recent years in spin injection into semiconductors, which uses tunnel barriers to overcome the impedance mismatch problem, which drastically limits the spin-injection efficiency [22-23]. Thus

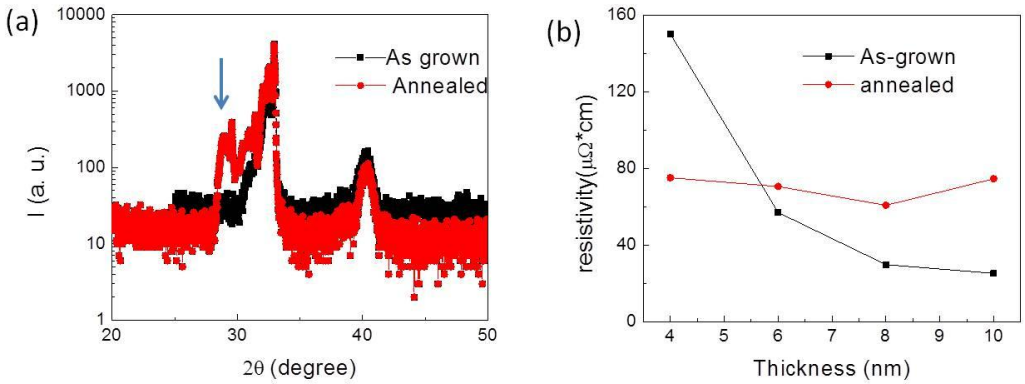

Figure 5-10. X-ray diffraction patterns and resistivity of WSi_x (a) X-ray diffraction patterns for sputtered α-W/FeCoB 5nm/Ta 1nm with (red) or without (black) the W layer annealed in the vacuum furnace for 2 hours at 700℃. The arrow indicates the identification of the WSi_x Bragg peaks. (b) Resistivity of our sputtered W films as a function of thickness.

spin injection into these materials through low-resistivity interfaces, that is, Ohmic contacts, promises an easy and versatile pathway for spin injection without the need for growing high-quality tunnel barriers [24].

One possible approach to this problem is spin injection into Si via spin hall effect. To test it, devices with the structure of Si/W 4nm / FeCoB 5nm/ Ta1nm and Si/W 20nm / FeCoB 5nm/ Ta1nm were patterned into the micron size and measured by ST-FMR. The results are shown in the Figure 5-11(a-b). The main feature of the plots are similar to that in the Figure 5-1(a-b): negative S/A ratio in β-W and positive in α-w, which suggests that the tungsten retains a high spin Hall angle (or spin pumping angle) when Si becomes its adjacent layer.

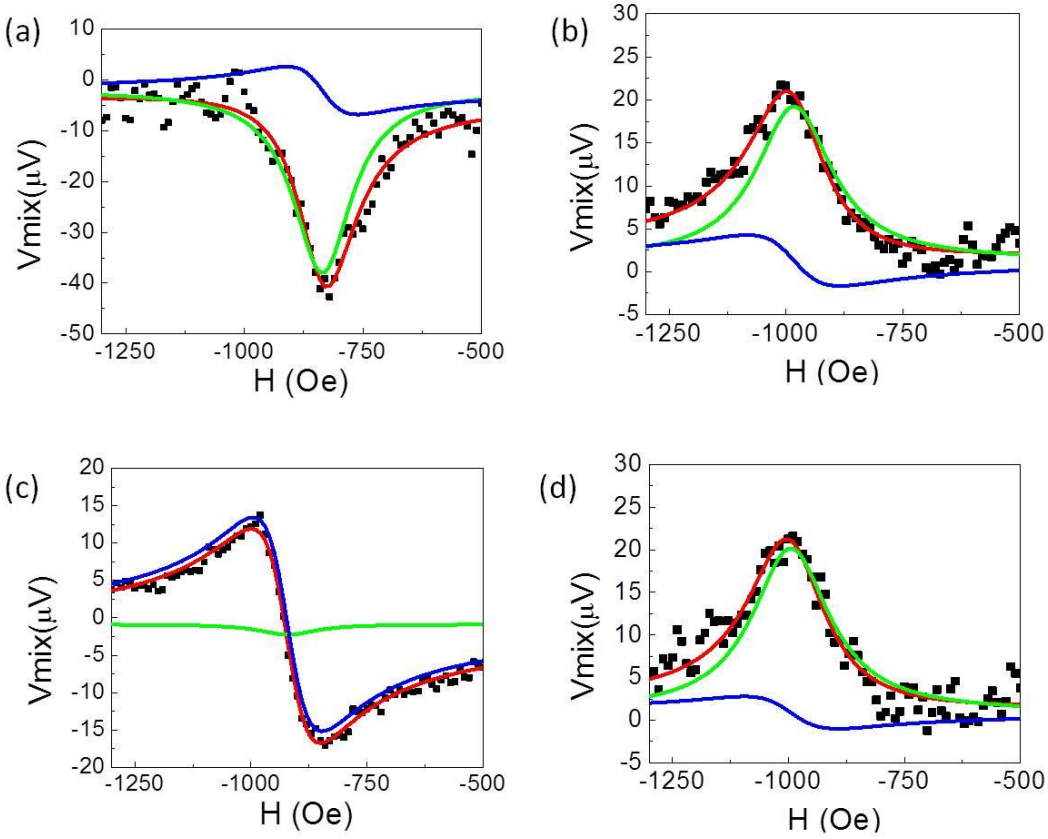

Figure 5-11. FMR spectra of samples with W or WSi_x (a) Si/W 4nm / FeCoB 5nm/ Ta1nm, (b) Si/W 20nm / FeCoB 5nm/ Ta1nm, (c) Si/WSi_x 4nm / FeCoB 5nm/ Ta1nm, (d) Si/WSi_x 20nm / FeCoB 5nm/ Ta1nm.

Since it is easy to form a Schottky barrier at the interface of W and Si layers, I also tried to grow WSi_x instead of W. Tungsten silicides on silicon have been widely studied because of process compatibility for fabricating semiconductor devices and low resistivity due to the Ohmic contact [25-26]. N-type Si wafers with resistivity 1-10 Ω·cm were treated by the RCA cleaning process in CNF. For the as-grown sample, all the films were deposited by DC sputtering in the AJA during one run. For the annealed sample, W thin film was deposited on the wafer first and followed by 700 ℃

annealing in the vacuum for 2 hours. Then the samples were put back into the sputtering system, back sputtered to remove the surface oxidation, and the rest FeCoB and Ta films were deposited on their top. The X-ray diffraction patterns for as-grown α-W (20nm) (black line) and annealed α-W(20nm) (red trace line) are shown in the Figure 5-10 (a). The peaks close to 30°, which only exist in the annealed sample, indicate WSi_x is formed in the annealed sample [27]. Meanwhile, while the resistivity of tungsten has strong thickness dependence due to the phase change, the resistivity of WSi_x varies little when the film goes thicker (see Figure 5-10 (b)), which confirms that our annealed sample is WSi_x.

FMR spectra measured for Si/WSi_x 4nm / FeCoB 5nm/ Ta1nm and Si/WSi_x 20nm / FeCoB 5nm/ Ta1nm are shown in the Figure 5-11 (c-d). The plots show that weak spin Hall signal is observed in the first case, the thin WSi_x sample, and a large spin pumping signal (similar to the α-W case) is detected in the second, thick WSi_x sample. Thus it may be difficult to use WSi_x as spin Hall material to inject spin into Si.

Possible device structures for spin injection into Si experiments are shown in the Figure 5-12. The spin generation may be via either spin Hall effect or spin pumping effect, and the promising ways to detect the spin in the silicon are by non-local spin valve and inverse spin Hall effect. However, problems involving material properties and fabrication process need be solved before any success.

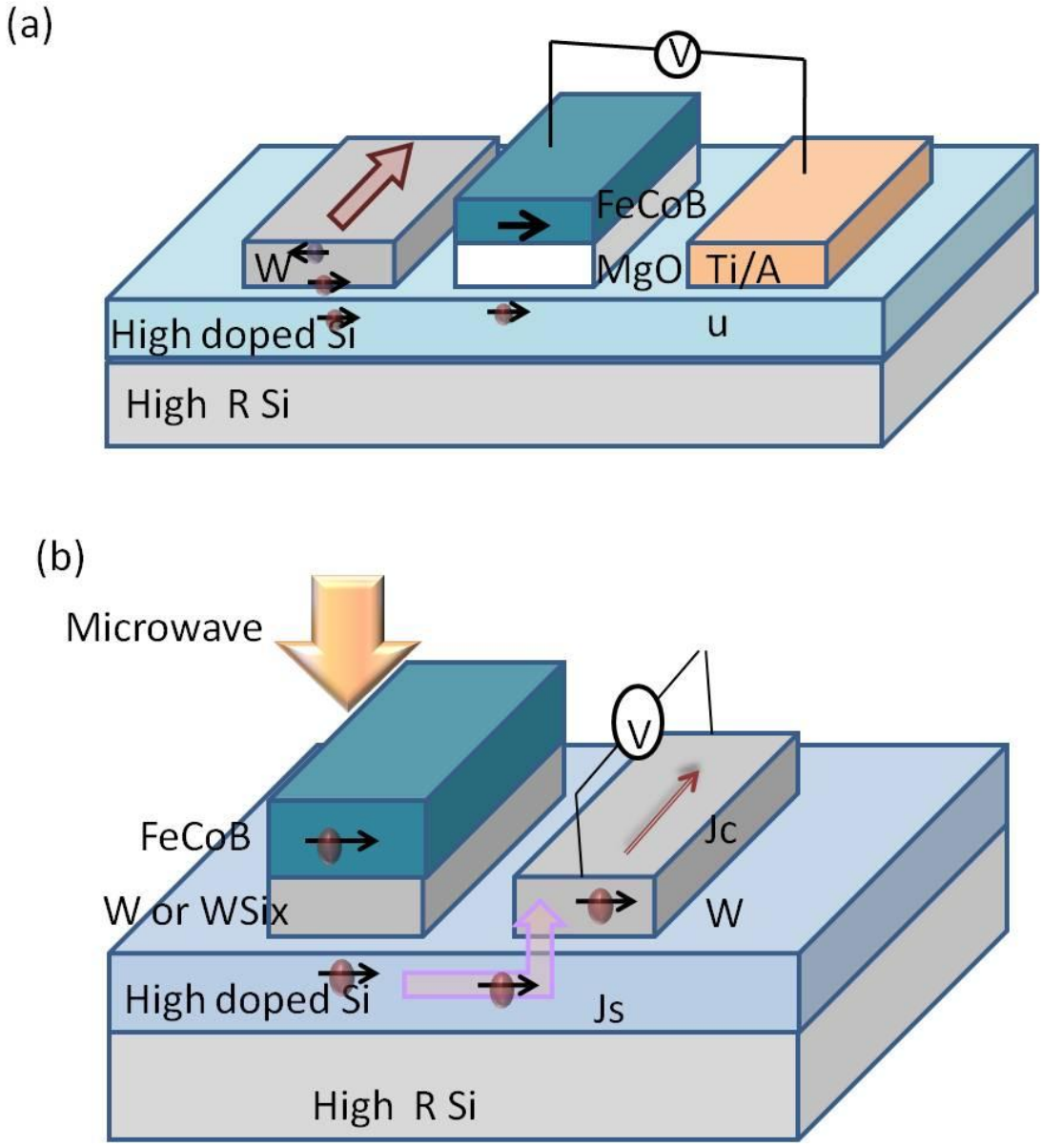

Figure 5-12 Schematic of the device structures illustrating the spin injection into the Si experiment: (a) Spin injected into Si via spin Hall effect and detected by non-local spin valve. (b) Spin injected by spin pumping effect and detected by inverse spin Hall effect.

5.8 Conclusion

In summary, the ferromagnetic resonance study of FeCoB/W thin film bi-layer structures is reported in this chapter. The result shows that the effective spin mixing conductance is enhanced in the α-W, leading to a strong spin pumping effect which cannot be negligible. Therefore the formula of spin Hall angle needs to be modified in α-W case. Moreover, VSM and SQIUD measurements indicate that the two different types of FeCoB/W bilayers have considerably different interfacial magnetic anisotropy coefficients and α-W may work as a good substrate for $Fe_{40}Co_{40}B_{20}$ with strong perpendicular magnetic anisotropy. Finally, spin injection into Si experiments are proposed, and the results from the initial work are discussed.

BIBLIOGRAPHY

1. Garlid, E. S., Hu, Q. O., Chan, M. K., Palmstrøm, C. J., & Crowell, P. a. Electrical Measurement of the Direct Spin Hall Effect in Fe/In_xGa_{1-x} As Heterostructures. *Physical Review Letters*, 105, 156602 (2010).

2. Liu, L., Pai, C.-F., Li, Y., Tseng, H. W., Ralph, D. C., & Buhrman, R. a. Spin-torque switching with the giant spin Hall effect of tantalum. *Science* 336,555 (2012).

3. D'yakonov M. I. and Perel V. I., Possibility of orienting spins with current. JETP Letter 13, 467 (1971).

4. S Murakami, S., Nagaosa, N., & Zhang, S.-C. Dissipationless quantum spin current at room temperature. *Science* 301, 1348 (2003).

5. Tanaka, T., Kontani, H., Naito, M., Naito, T., Hirashima, D., Yamada, K., & Inoue, J. Intrinsic spin Hall effect and orbital Hall effect in 4d and 5d transition metals. *Physical Review B*,77, 165117 (2008).

6. Pai, C.-F., Liu, L., Li, Y., Tseng, H. W., Ralph, D. C., & Buhrman, R. A. Spin transfer torque devices utilizing the giant spin Hall effect of tungsten. *Applied Physics Letters*, *101*(12), 122404. 101, 122404 (2012).

7. Weerasekera, I. a., Shah, S. I., Baxter, D. V., & Unruh, K. M. Structure and stability of sputter deposited beta-tungsten thin films. *Applied Physics Letters*, 64, 3231 (1994).

8. Liu, L., Moriyama, T., Ralph, D. C., & Buhrman, R. A. Spin-Torque Ferromagnetic Resonance Induced by the Spin Hall Effect. *Physical Review Letters*, 106, 036601 (2011).

9. Wegrowe, J.-E., & Drouhin, H.-J. Spin-Currents and Spin-Pumping Forces for Spintronics. *Entropy*, *13*, 316 (2011).

10. Azevedo, a., Vilela-Leão, L. H., Rodríguez-Suárez, R. L., Lacerda Santos, a. F., & Rezende, S. M. Spin pumping and anisotropic magnetoresistance voltages in magnetic bilayers: Theory and experiment. *Physical Review B*, 83, 144402 (2011).

11. Tserkovnyak, Y., Brataas, A., & Bauer, G. Spin pumping and magnetization dynamics in metallic multilayers. *Physical Review B*, 66, 224403 (2002).

12. Meservey, R., & Tedrow, P. Surface Relaxation Times of Conduction-Electron Spins in Superconductors and Normal Metals. *Physical Review Letters*, 41, 805 (1978).

13. Czeschka, F. D., Dreher, L., Brandt, M. S., Weiler, M., Althammer, M., Imort, I.-M., Reiss, G., et al. Scaling Behavior of the Spin Pumping Effect in Ferromagnet-Platinum Bilayers. *Physical Review Letters*, 107, 046601 (2011).

14. Mosendz, O., Pearson, J. E., Fradin, F. Y., Bauer, G. E. W., Bader, S. D., & Hoffmann, A. Quantifying Spin Hall Angles from Spin Pumping: Experiments and Theory. *Physical Review Letters*, 104, 046601 (2010).

15. Pal, S., Rana, B., Hellwig, O., Thomson, T., & Barman, A. Tunable magnonic frequency and damping in $[Co/Pd]_8$ multilayers with variable Co layer thickness. *Applied Physics Letters*, 98, 082501 (2011).

16. Ikeda, S., Miura, K., Yamamoto, H., Mizunuma, K., Gan, H. D., Endo, M., Kanai, S., et al. A perpendicular-anisotropy CoFeB-MgO magnetic tunnel junction. *Nature materials*, 9, 721 (2010).

17. Liu, X., Zhang, W., Carter, M. J., & Xiao, G. Ferromagnetic resonance and damping properties of CoFeB thin films as free layers in MgO-based magnetic tunnel junctions. *Journal of Applied Physics*, 110, 033910 (2011).

18. Seo, J., Oh, Y., Kim, T.-H., & Kuk, Y. Strain relaxation induced spin reorientation in Fe films on W(110). *Applied Physics Letters*, 99, 182501 (2011).

19. Heide, M., Bihlmayer, G., & Blügel, S. Dzyaloshinskii-Moriya interaction accounting for the orientation of magnetic domains in ultrathin films: Fe/W(110). *Physical Review B*, 78, 140403 (2008).

20. Vedmedenko, E., Kubetzka, a., Von Bergmann, K., Pietzsch, O., Bode, M., Kirschner, J., Oepen, H., et al. Domain Wall Orientation in Magnetic Nanowires. *Physical Review Letters*, 92, 077207 (2004).

21. Jansen, R. Silicon spintronics. *Nature materials*,11,400 (2012).

22. Dash, S. P., Sharma, S., Patel, R. S., De Jong, M. P., & Jansen, R. Electrical creation of spin polarization in silicon at room temperature. *Nature*, 462,491 (2009).

23. Sasaki, T., Oikawa, T., Suzuki, T., Shiraishi, M., Suzu, Y., & Noguchi, K. Evidence of Electrical Spin Injection Into Silicon Using MgO Tunnel Barrier. *IEEE Transactions on Magnetics*, 46, 1436 (2010).

24. Ando, Kazuya, & Saitoh, E. Observation of the inverse spin Hall effect in silicon. *Nature communications*, 10, 655 (2011).

25. Jnawali, G., Meyer zu Heringdorf, F.-J., Wall, D., Sindermann, S., & Horn-von Hoegen, M. Stable tungsten disilicide contacts for surface and thin film resistivity measurements. *Journal of Vacuum Science & Technology B: Microelectronics and Nanometer Structures*, 27, 180 (2009).

26. Byun, J. S., Lee, H., Park, J., Sohn, K., Hong, J., & Cho, W. Reduction of Dichlorosiliane-Based Tungsten Silicide Resistivity by Amorphization and Its Applicability as an Electrode, 146, 2261 (1999).

27. Tsai, M. Y. Properties of tungsten silicide film on polycrystalline silicon. *Journal of Applied Physics*, 52, 5350 (1981).

28. Worledge D. C., Hu G., Abraham D. W., Sun J. Z., Trouilloud P. L., Nowak J., Brown S., Gaidis M. C., Sullivan E. J. O', and Robertazzi R. P., *Applied Physics Letter*, 98, 022501 (2011).